ATMOSPHERIC OXYGEN DENSITY STUDIES BY SOLAR ULTRA-VIOLET ABSORPTION

BY

Paul Lancelot GOUGH B.Sc. (Hons)

Department of Physics

A thesis

presented for the degree of

Doctor of Philosophy

in the

University of Adelaide

January, 1971

SUMMARY

The absorption of solar extreme ultra-violet radiation in the earth's atmosphere represents a powerful tool for determining information on the composition of the atmosphere. Existing information on the composition of the atmosphere above about 100 Km. is still quite poor, even for major constituents such as N_2, O_2 and O. This is the most significant reason for the failure to establish a satisfactory "reference atmosphere". A small variation of the assumed composition in the lower part of the thermosphere (i.e. from about 90 Km. to 150 Km.) can lead to an enormously amplified variation of the "reference atmospheres" properties at higher altitudes.

Ultra-violet ion chambers have been used to study the absorption of wavelengths in the range 1050 Å to 1680 Å. In this region, molecular oxygen is the major absorber so that molecular oxygen densities as well as absolute solar flux intensities are obtainable.

In this work, five rockets and one satellite were fired from Woomera, South Australia.

Four HAD rockets were instrumented with lithium fluoride-nitric oxide ion chambers which respond in the range 1050 to 1350 Å. This range includes the important Lyman α line which penetrates the

atmosphere to a height of 70 Km. By using these ion chambers molecular oxygen densities can be determined in the height range 70 Km. to 90 Km. and absolute measurements of the solar Lyman-α flux can be made. No HAD rocket performed satisfactorily ; three did not reach the minimum height of 70 Km. and the other precessed so badly that very grave errors were involved in density and flux information.

One successful LONG TOM rocket was instrumented with thirteen ion chambers of different types covering the range 1050 Å to 1680 Å. Detailed measurements of molecular oxygen density in the height range 70 Km. to 120 Km. were obtained as well as solar ultra-violet fluxes within this important ultra-violet range.

Preliminary results from Australia's first satellite, WRESAT, which was instrumented with ion chambers, are discussed and compared with results from both the rocket flights and other workers in the field.

PREFACE

This thesis contains no material which has been accepted for the award of any other degree or diploma in any University. To the best of the author's knowledge and belief it contains no material previously published or written by another person, except when due reference is made in the text.

ACKNOWLEDGEMENTS

The experiments described in this thesis were carried out in co-operation with the Flight Projects Group, Weapons Research Establishment. The author would like to express his thanks to all persons involved with the construction and launching of the rockets and in particular Mr. B. Rofe for making these experiments possible.

The author would also like to thank the South Australian Institute of Technology for allowing time for the author to continue this work whilst in their employ.

Finally, the author would like to thank his supervisor Professor J.H. Carver most sincerely for his guidance throughout the course of this work.

CONTENTS

CHAPTER 1. THE SOLAR SPECTRUM

1.1.1. INTRODUCTION

The observable optical spectrum of the sun extends from the beginning of the radiofrequency spectrum ($\lambda \approx$ millimeters) to the X-ray spectra ($\lambda \approx 1$ Å). Below 1,700 Å the solar spectrum consists almost entirely of emission lines superimposed on a very faint continuum. These emission lines arise from atoms in many stages of ionization. HI, HeI, HeII, OVI and MgX are some typical examples. The existence of these emission lines imply radiation temperatures* up to several million degrees. Above 1,700 Å and extending into the infrared, the solar spectrum is a continuous spectrum crossed by Fraunhofer absorption lines. These absorption lines are those of neutral and singly ionized atoms which should appear at radiation temperatures of about 4,000°K to 6,000°K.

According to the present model of the solar atmosphere (Gingerich and de Jager, 1968) its emitting region can be classified into three layers:-

(a) The photosphere. This is the innermost region and is about 300 Km. thick. The radiation temperature is about 8,000°K at the base, dropping to about 4,500°K at the top.

---

*The radiation temperature of the sun at a particular wavelength is the temperature of a black body which would emit as much radiation at that wavelength as the sun.

(b) The chromosphere. This region is directly above the photosphere and is about 20,000 Km. thick. The radiation temperature extends from about 4,500°K where it joins the photosphere to about 40,000°K where it meets the corona.

(c) The Corona. This region is a very hot plasma, its radiation temperature being of the order of one to two million degrees. The corona has been observed to extend to distances of the order of 10 solar radii and probably does not have a well defined boundary as it merges into the interplanetry medium.

The visible spectrum, extending from approximately 4,000 to 7,000 Å, and including most of the Fraunhofer absorption lines originates in the photosphere. No radiation originating from below the photosphere can escape to the surface without being totally absorbed as the photospheric gases have a high opacity. The top of the photosphere is defined as the level at which the gases are just barely beginning to become opaque and thus the radiation that escapes from the photosphere suffers partial absorption on the way out.

At visible wavelengths the spectra of the chromosphere and corona are so faint that they cannot be observed unless steps are taken to obscure the enormously greater intensity from the photosphere. The intensity of the visible emission from the chromosphere is only about

one ten thousandth that of the photosphere. A flash spectrum* gives the best results when photographing the visible chromospheric spectrum and is only observable for a few seconds immediately before and after a total solar eclipse. Flash spectra have yielded a large portion of the information known concerning the physical state of the chromosphere. The visible radiation from the corona is one hundredth the intensity of that from the chromosphere and is again best studied during total eclipses. A continuous spectrum makes up approximately 97% of the visible radiation of the corona. The remaining 3% is in the form of bright emission lines from very highly ionized atoms (i.e. CaXII, NiXVI). The occurrence of these high stages of ionization indicates temperatures of one or two million degrees. The continuous spectrum arises from radiation from the photosphere being scattered by the electrons in the inner regions of the corona and by dust in the outer regions.

The photospheric spectral energy curve at visible wavelengths closely simulates that of a black body with a temperature of 6,300°K. At longer wavelengths in the infra-red region, the opacity of the photosphere increases with increasing wavelength and therefore the radiation temperature diminishes and approaches a boundary value of approximately 4,500°K. As the wavelength decreases, into the ultra-violet spectrum, the opacity of the chromosphere also increases and the observed radiation

---

*A spectrum of the last bright light that is seen as the moon covers the sun at a total eclipse and the first flash of light that appears as the moon moves off. No slit is needed on the spectrograph for the limb of the moon and the edge of the chromosphere combine to form a slit.

comes from progressively higher regions. Thus the radiation temperature decreases as the wavelength decreases and the intensity of the solar continuum lies below that of a 6,300°K black body down to 100 Å. At about 1,400 Å the radiation temperature reaches a minimum of 4,500°K* corresponding to a change in the origin of the continuum from the photosphere to the chromosphere. At wavelengths less than 1,400 Å the radiation temperature increases as the origin of the radiation moves up through the chromosphere and into the corona.

Figure 1.1 summarizes the regions where the various sections of the spectrum originate. The X-ray region of the spectrum shows large variations in intensity; in Figure 1.1 the spectrum shown is for quiet conditions at solar maximum.

1.2.1. MEASUREMENT OF THE SOLAR ULTRA-VIOLET SPECTRUM

Solar radiation below 2,900 Å is absorbed by atomic oxygen, nitrogen, molecular oxygen and ozone in the earth's atmosphere so that the nature of the solar spectrum at wavelengths less than 2900 was unknown until rockets capable of rising to heights greater than 75 Km. were available. Balloons were unsuitable as they could not rise above the ozone which reaches its maximum at about 25 Km. In 1946 captured German V2 rockets were fired in America to study the ultra-violet spectrum. The instrument used to record the first ultra-violet spectra was a

---

*The radiation temperature of 4500 K at the minimum is that indicated by the present work and recently has been verified by Parkinson and Reeves (1969). See Chapter six.

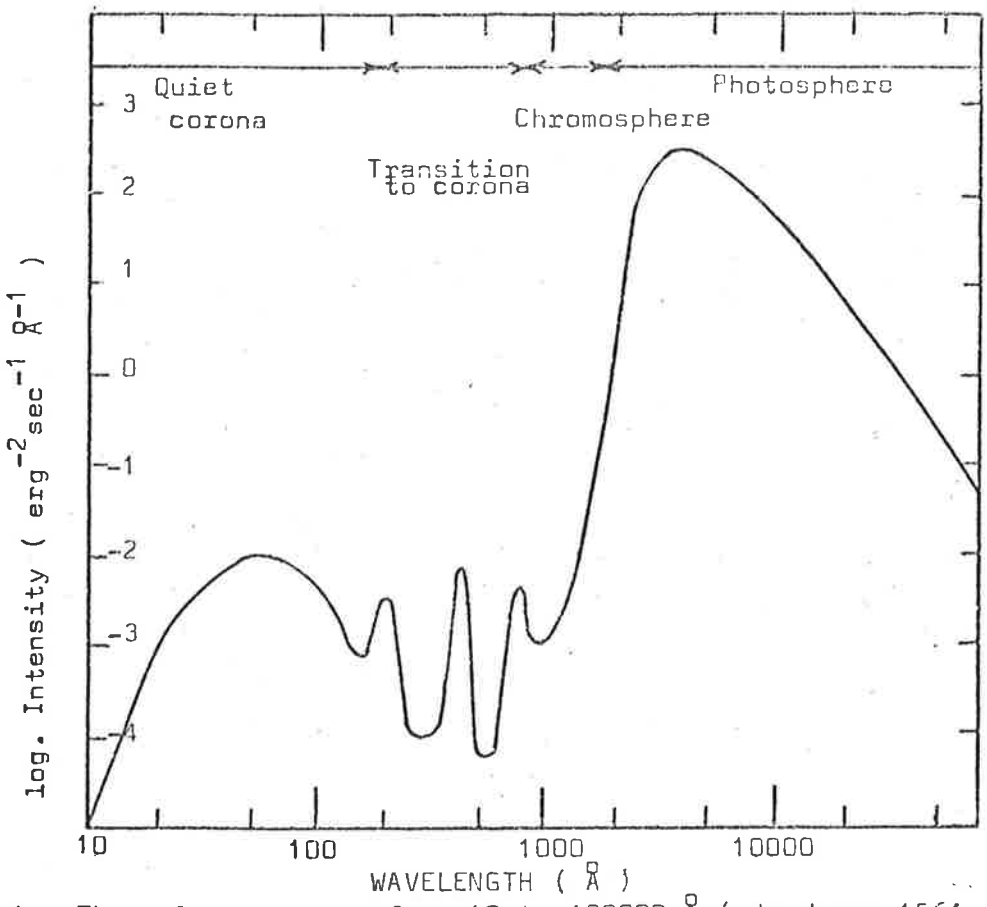

Fig. 1.1. The solar spectrum from 10 to 100000 Å (de Jager 1964 and Allen 1963). The regions where the various sections of the spectrum originate are indicated above. The X-ray region of the spectrum (λ less than 100 Å) is extremely variable.

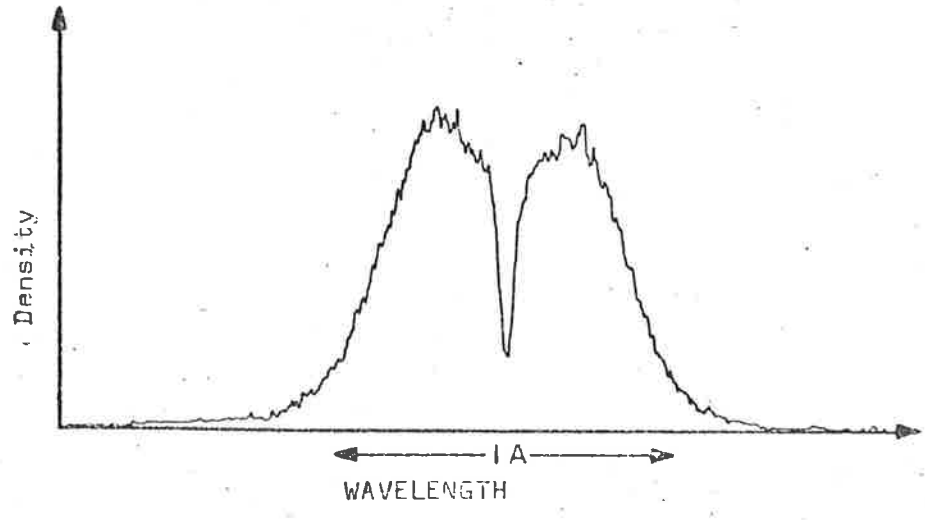

Fig. 1.2. The profile of the solar Lyman-α line by Purcell and Tousey 1959. (from Friedman 1961)

normal incidence grating spectrograph with photographic recording. As the rocket was unstabilized the spectrograph needed a wide field of view. The first spectra taken from a V2 rocket (Braun et al 1946) were not of good resolution and showed a continuation of the visible continuum down to 2100 Å with the very strong absorption doublet of MgII. A series of thirty-five spectra were taken at heights up to 88 Km. Another V2 flight was made in 1947 and about thirty absorption lines were identified down to 2300 Å. As the solar spectrum intensity drops rapidly below 2100 Å any extensions to lower wavelengths were difficult to achieve. To overcome this problem detectors suitable for flight in unstabilized rockets were developed and flown. At the same time, a pointing control was developed which could keep instruments pointing towards the sun irrespective of the motion of the rocket. Since this time, the methods of measuring ultra-violet fluxes have followed two lines : non-dispersive measurements, where pointing controls are not necessary, i.e. ion chambers, and the dispersive methods, i.e. spectrographs where pointing controls are essential.

1.2.2 DISPERSIVE MEASUREMENTS WITH PHOTOGRAPHIC RECORDING

The first pointing control was developed to be built into the Aerobee rocket which was used almost exclusively for solar spectrum measurements from 1952 onwards. The history of these and subsequent observations up to 1963 has been reviewed by Tousey (1963).

In 1952 Rense (1953) using the biaxial pointing control and a grazing incidence spectrograph obtained the first image of the Lyman-α (1215.7 Å) resonant line of atomic hydrogen which is an emission line, in contrast to the absorption lines which had been observed up to that time. The intensity of this line was measured as 0.5 erg cm^{-2} sec^{-1}.

A double normal incidence spectrograph was developed and flown in 1954 and is described by Johnson et al (1958). Two spectrographs, one covering the range 500 to 2500 Å and the other 1500 to 3500 Å were included. A number of flights were made with this instrument. In 1954, the altitude reached was 104 Km. and only the Lyman-α line was observed, as the emission lines, apart from Lyman-α in the ultra-violet spectrum between 1000 and 1700 Å, are absorbed by molecular oxygen at a greater height than 104 Km. However, the image of Lyman-α was better than that observed by Rense. About forty emission lines other than Lyman-α were first found in 1955 using the same instrument, as the rocket reached an altitude of 115 Km. Intensities of 0.6 and 1.6 erg cm^{-2} sec^{-1} for the Lyman-α flux were determined from the 1954 and 1955 flights respectively.

A grazing incidence spectrograph, which enables shorter wavelengths than the normal incidence spectrograph mentioned above to be determined was flown in 1957 by Aboud et al (1959). Violett and Rense (1959) flew an improved version of this instrument in 1958 and 1959 and detected for the first time the resonance lines of HeI

(584 Å) and HeII (304 Å). Although the grazing incidence spectrograph was more efficient at short wavelengths then the normal incidence, the gain was decreased by the increase in stray light which was worse at grazing than at normal incidence. As a result the spectra obtained by Violett and Rense were difficult to interpret.

Improvements were made to the normal incidence spectrograph flown by Johnson by coating the grating to reduce the effect of stray light. This improved instrument was flown in 1959 by Purcell et al (1960). The altitude reached was 198 Km. which allowed more emission lines than those found by Johnson to be detected.

Purcell and Tousey in 1959 observed the profile of the Lyman-α line. The spectrograph employed a 50 cm. radius, 1200 line/mm grating in the thirteenth order, which produced a resolution of about 0.03 Å at Lyman-α. Figure 1.2 includes a profile of this line which is characterized by a broad depression at the centre leaving two maxima separated by approximately 0.4 Å. The formation of this absorption occurs in the solar atmosphere. In the centre of the broad reversal is a narrow central absorption core which is produced by neutral hydrogen between the rocket and the sun.

The recorded spectra were improved by flying a double dispersion spectrograph in 1960 (Detwiler et al 1961a). A grating dispersed the solar radiation along a slit from which the radiation passed to a second grating. In this way, the level of stray light

was reduced as the visible and near ultra-violet portions of the spectrum fell beyond the end of the slit. The first grating was distorted to make the final images stigmatic, i.e. the intensity distribution along a line corresponded to the intensity distribution along a diameter of the solar disc at that wavelength. By using an ion chamber which was flown with the spectrograph the absolute level of the fluxes were determined and from this flight an intensity distribution for the region 900 to 1550 Å was derived.

A grazing incidence spectrograph was flown by Tousey et al (1963) in 1961 and 1962. This spectrograph eliminated the stray light problem experienced with previous grazing incidence spectrographs by passing the radiation from the sun through an unbacked thin aluminium film. As aluminium films only transmit at wavelengths shorter than 830 Å, this film acted as a filter eliminating visible to extreme ultra-violet stray light down to 830 Å. The region from approximately 810 to 170 Å was transmitted.

The double dispersion instrument covering the ranges 800 to 1250 Å and 1200 to 2000 Å was flown in 1962 by Tousey et al (1964). Nearly complete elimination of stray light enabled the continuum to be traced down to a wavelength of about 950 Å. The double dispersion instrument was reflown in July, 1966 by Purcell, Snider and Tousey giving spectra significantly better for photometry than the 1962 flight or a flight in February, 1966. The results of these spectra

between the limits 1520 and 1780 Å have recently been published by Widing et al (1970) (See Figure 1.3).

Figure 1.4 shows a spectrum from Tousey (1964). As the ion chambers used in the present work cover the region 1050 to 1660 Å both the spectra in Figure 1.3 and 1.4 are referred to in later Chapters.

Obtaining absolute fluxes from photographic measurements is very difficult. The difficulties have been discussed by Johnson et al (1958) and Detwiler et al (1961b). Both the sensitivity of the film and the instrument transmission constant must be measured as functions of wavelength. These two quantities can be measured simultaneously by using an absolutely calibrated beam of monochromatic radiation at various wavelengths, but this does not provide an accurate method of calibration as the angular divergence of the beam from the laboratory source may not be the same as that from the sun. Thus, one of the following additional methods have usually been used.

(a) The spectrograph efficiency can be calculated from the measured efficiency of the gratings. The spectral distribution from a carbon arc has been published (Johnson, 1956) so that the relative intensities in a carbon arc continuum transmitted by the spectrograph can be checked against the published distribution. This provided a check on the calculated efficiency

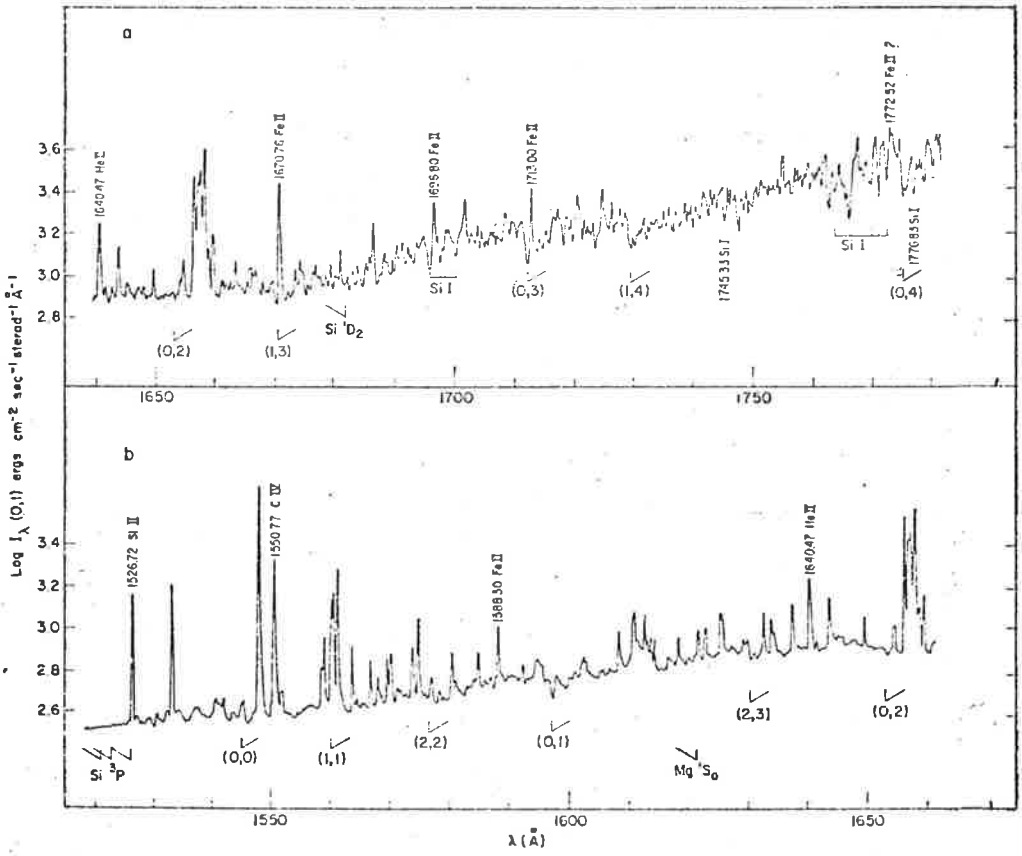

Fig. 1.3. The intensity distribution in the solar spectrum between 1520 and 1760 Å. No attempt should be made to read line intensities from the graph as the spectra were traced in a rapid scan and some lines may not have been properly recorded. (Widing et al 1970)

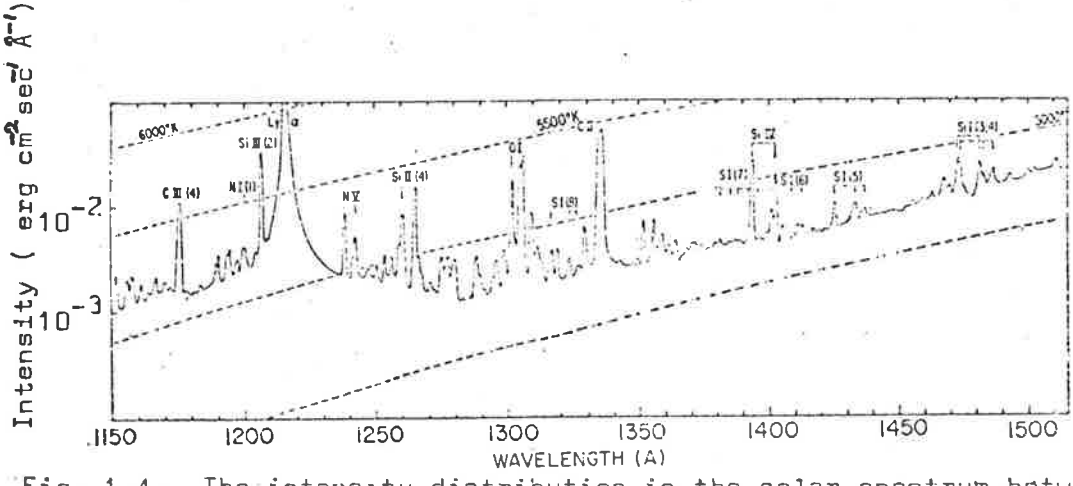

Fig. 1.4. The intensity distribution in the solar spectrum between 1150 and 1520 Å. (Tousey, 1964) Both this spectrum and those in Fig.1.3. have been determined by density tracings from photographic exposures.

only above the effective short wave limit of the carbon arc exposures (1920 Å). Calibration below 1920 Å relied on calculated efficiencies. Widing et al (1970) used this method of calibration.

(b) The spectrograph may be flown with an absolutely calibrated ion chamber (See Section 1.2.4) which is more readily calibrated as it relies on the known photoionization efficiency of nitric oxide (See Section 3.3.3). This method was first used by Byram et al (1958) who used ion chambers sensitive to the ranges 1050 to 1350 Å and 1225 to 1350 Å to correct the absolute fluxes derived from the 1955 flight by Johnson et al (1958).

1.2.3 DISPERSIVE MEASUREMENTS WITH PHOTO-ELECTRIC SCANNING

A different technique for the measurement of the solar spectrum has been used by Hinteregger and his colleagues. Their technique was to use a grazing incidence grating with in-flight photo-electric recording.of the spectrum and data transmission by telemetry. The spectrum was scanned by a slit in a moving belt and detected by a windowless, magnetically focussed, strip-type photomultiplier with a gain of 10^8. The photo-cathode was a tungsten plate of sufficient width to cover the entire region of the spectrum to be studied. Insensitivity to intense long wavelength stray light

was achieved as the photocathode had negligible sensitivity to radiation of wavelength longer than about 1300 Å. By careful electrical trapping of ions that would be admitted through the pumping ports, from the atmosphere, Hinteregger was able to reduce the background signal nearly to that produced by cosmic radiation. Photon counting rates between 10^6/sec. and 20/sec. were obtained with this instrument, and two flights were made during 1960 (Hinteregger 1961b, Hinteregger 1961c) which gave spectra covering the range 300 to 1300 Å. Absolute values for the flux of all the important emission lines and the continuum in this range were determined. Estimates were also made of the penetration height at which the solar flux had been attenuated to $^1/_e$ of its value above the atmosphere for the various wavelengths. The number of photons absorbed per unit volume per unit time (absorption rate densities) were also derived as a function of height for several strong lines. Lyman-α intensities were derived from the results of these two flights. They were 6.0 and 3.3 erg cm^{-2} sec^{-1}. A lithium fluoride window, nitric oxide gas filling ion chamber was flown with the spectrometer giving the value 3.3 erg cm^{-2} sec^{-1}.

From another flight in 1961, with the scanning monochromator, Hall et al (1963a) derived further values of absolute fluxes and photon absorption rate densities. These measurements were used to obtain the densities of the principal atmospheric constituents above 100 Km. Further analysis involving photoionization efficiencies have enabled Hinteregger and Watanabe (1962) and Hinteregger et al (1965) to

give an account of the processes leading to the formation of the F and E regions of the ionosphere.

A grazing incidence spectrometer of the same basic type has been constructed by Behring et al (1962) and flown first in an Aerobee rocket and then in the Orbiting Solar Observatory (OSO-1). It was designed to yield a spectral distribution over the 60 to 400 Å wavelength band. The sunlight was dispersed at a two degree grazing angle grating and the spectrum was focused on the Rowland circle. The spectrometer differed from the instrument of Hinteregger in that the detector was mounted on a motor driven carriage which moved along a track coincident with the Rowland circle.

Another type of spectrometer was flown in 1968 by Parkinson and Reeves (1969). This was a photo-electric scanning, Ebert spectrometer equipped with a telescope system. The Ebert mirror, of focal length 77.5 cm., was used in conjunction with a 3600 lines/mm plane grating. The complete instrument gave a resolution of 0.06 Å (full width, half maximum intensity). This instrument was flown specifically to investigate the wavelength band 1400 to 1900 Å as measurements of intensities in this band suggest a value for the solar temperature minimum. The wavelength bandpass for the instrument was determined by the photomultiplier which had a side window of lithium fluoride and a photocathode of caesium iodide. This combination of window-photocathode gave a bandpass of 1050 to 2500 Å. Parkinson

and Reeves (1969) gave absolute intensities derived from this experiment compared with two points from their satellite (OSOIV) data. Their data confirms the present work on solar intensities within the range 1400 to 1600 Å (See Section 6.2.3.).

In general the photo-electric method provides better absolute measurements of the solar spectrum (particularly below 1300 Å) and is more suitable than the photographic measurements for studying the absorption of solar radiation and hence properties of the earth's atmosphere. The photographic method provides better resolution and sensitivity, making it useful for obtaining data on the nature of the solar atmosphere. However, the photographic method is unsuitable for use in satellites where the data must be compatible with telemetry.

1.2.4 NON-DISPERSIVE MEASUREMENTS

Once the solar spectrum had been revealed down to 2100 Å with spectrographic measurements from the V2 rockets, attempts were made to extend the measurements to short wavelength ultra-violet radiation using non-dispersive techniques. As the spectrographic technique required a pointing control to extend the spectrum, there was a need to attempt non-dispersive techniques that could be flown from unstabilized rockets. The original method involved the use of the thermo-luminescent phosphor $CaSO_4$:Mn. The phosphor was activated when exposed to radiation of wavelength less than 1340 Å and phosphor-

esced when subsequently heated. Lithium fluoride and calcium fluoride which have short wavelength transmission limits of 1050 Å and 1220 Å, respectively, were made into windows and placed in front of the phosphor. This limited the response of the phosphor to two wavelengths ranges ; 1050 to 1340 Å and 1220 to 1340 Å. The range 1050 to 1340 Å included the important Lyman-α emission line (1215.7) whereas the other range did not and hence could be used to determine the absolute flux without Lyman-α. These detectors were flown in V2 rockets a number of times during the period 1948 to 1950 (Tousey et al 1951) and showed that the radiation in the range 1050 to 1340 Å was absorbed in the 80 to 90 Km. region in the earth's atmosphere. The 1220 to 1340 Å radiation was absorbed in the 90 to 125 Km. region. As detectors for measuring absolute fluxes they were not very successful, indicating an intensity for the Lyman-α line of 0.4 erg cm^{-2} sec^{-1}.

Geiger counters sensitive to ultra-violet radiation were first flown during 1949 in a V2 rocket from White Sands, New Mexico. (Friedman et al 1951). The three counters used responded to the ranges 1100 to 1350 Å, 1425 to 1650 Å and 1725 to 2100 Å. The counter responding to Lyman-α radiation had a lithium fluoride window and a gas filling of chlorine and neon, which yielded a value for the Lyman-α intensity between 1 and 10 erg cm^{-2} sec^{-1}. Interpretation of the results was difficult owing to saturation of the detectors, doubts on the calibration and the existence of a weak tail of long wavelength

sensitivity. Similar detectors were flown in April and May, 1952 (Byram et al 1953) yielding values of 0.15 and 0.1 erg cm^{-2} sec^{-1} for the Lyman-α flux. The best counter experiment yielded the lowest value for the observed Lyman-α flux. The large scattering of results was attributed to experimental uncertainities which showed that the counters were unsuitable for absolute flux determination. However, with the 1100 to 1350 Å detector, when the logarithm of the counters response was plotted against residual air mass, a straight line relationship, characteristic of monochromatic radiation, was observed, This lead Byram et al to estimate that at least 90% of the radiation within the range 1100 to 1350 Å was Lyman-α.

The first ion chamber used for non-dispersive measurements was flown in October, 1955 by Byram et al (1956). This detector, which has been used since almost exclusively for non-dispersive measurements, had a lithium fluoride window, nitric oxide filling and responded to the range 1100 to 1345 Å. As the calibration procedure (See Section 3.3.3) was simple and accurate, these chambers could be relied upon for determining absolute fluxes. Values for the Lyman-α flux were 5.7 and 4.0 erg cm^{-2} sec^{-1} derived from the October, 1955 flights and 9.2 erg cm^{-2} sec^{-1} from a November, 1955 flight. These values were all higher than previous ones but were accepted in preference. Byram et al (1958) pointed out that the sensitivity of the chambers themselves can only decrease as a result of aging between calibration and flights, so that provided there were no errors from

other sources the values obtained must be minimum values. In 1956 an ion chamber was flown during a solar flare by Chubb et al (1957) in order to detect any change in the Lyman-α flux during the flare. Their results indicated that the flux did not vary to any measurable extent. From this flight and others made in 1957 the Lyman-α flux values were found to be close to 6 erg cm^{-2} sec^{-1}.

In order to obtain absolute levels of spectrographic measurements Byram et al (1958) flew two ion chambers, one responding to 1050 to 1350 Å and the other to 1220 to 1350 Å which had a calcium fluoride window, nitric oxide filling. It was pointed out by Byram et al that while measurements of the total flux in the 1050 to 1350 Å range may be used to determine the absolute Lyman-α flux, the 1220 to 1350 Å range was better for determining the level of other lines. The Lyman-α line is usually over exposed on photographic spectra and comparison with other lines is difficult.

Lithium fluoride-nitric oxide ion chambers have been flown in satellites, i.e. Solar Radiation I, Explorer 30, WRESAT I with the aim of monitoring continuously the Lyman-α flux. "Lyman-α" flares, even though they are a rare occurrence, have been observed by the Naval Research Laboratory. Changes in flux of approximately 30% have been detected which may be large enough to cause significant changes in D region ionization.

CHAPTER 2. ATMOSPHERIC ABSORPTION OF SOLAR ULTRA-VIOLET RADIATION

2.1.1. INTRODUCTION

The absorption of solar extreme ultra-violet fluxes represents an important and probably dominant source of heating and ionization of the upper atmosphere and is the only source which is reasonably well understood quantitatively. However, existing information on the composition of the atmosphere above about 100 Km. is quite poor, even for major constituents like N_2, O_2 and O. This is the most significant reason for the failure to establish a satisfactory "reference atmosphere". A small variation of the assumed composition in the lower part of the thermosphere (i.e. from about 90 to 150 Km.) can lead to an enormously amplified variation of the "reference atmosphere's" properties at higher altitudes.

The absorption of wavelengths in the range 1000 $\mathring{A}$ to 1700 $\mathring{A}$ will be considered in detail as this is the region where the ion chambers described in Chapter Three operate. In this region, molecular oxygen is the major absorber above 70 Km., although minor constituents absorb to a small extent. Of the minor constituents water vapour absorbs very strongly so that even a small concentration of water vapour can affect the measurements of ultra-violet fluxes. No experimental determinations of water vapour above 70 Km. have been

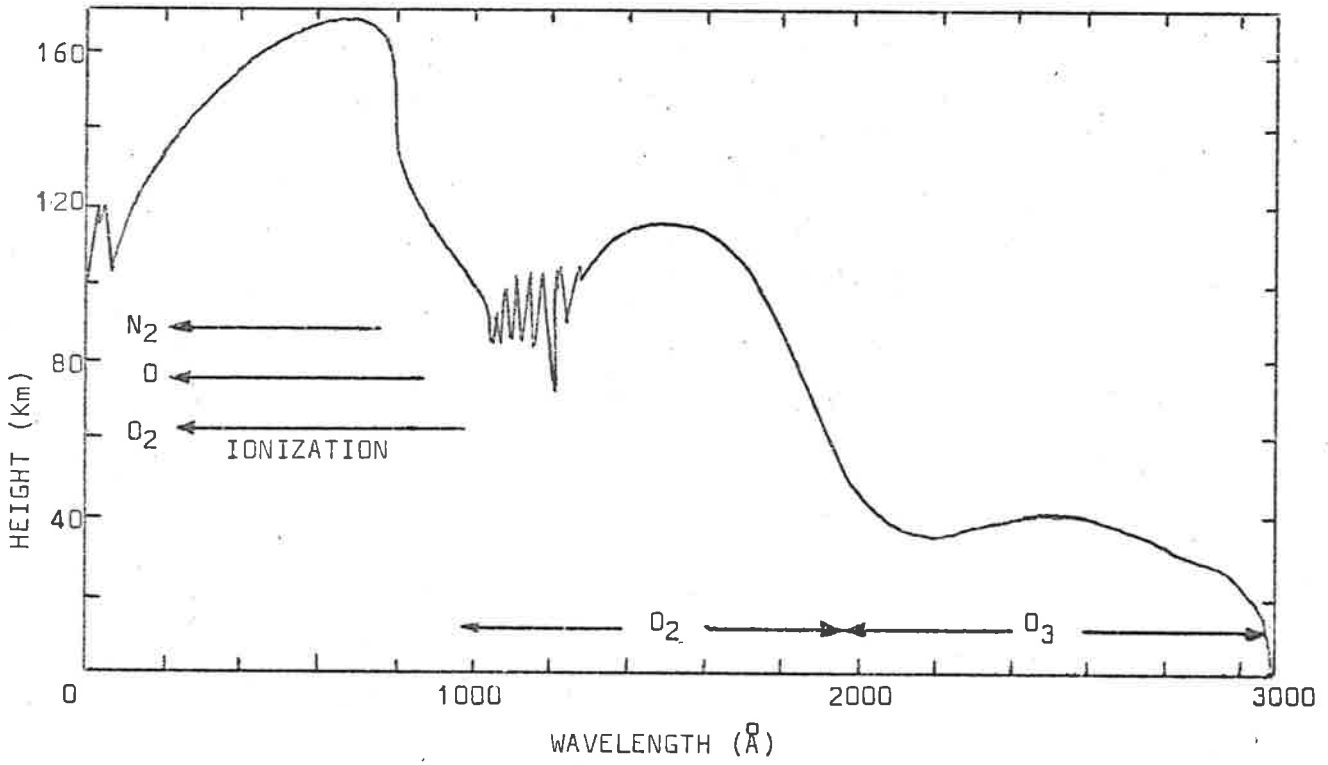

Fig. 2.1. The variation of penetration height with wavelength (after Friedman 1960). The penetration height is the height at which the solar flux has been attenuated to 1/e of its value outside the atmosphere.

made but Bates and Nicolet (1950) have made theoretical estimates. From their estimates absorption of Lyman-α due to water vapour is 4% relative to oxygen at 70 Km. reducing to less than 0.1% higher than 90 Km. The other minor constituents account for only a small fraction of the absorption (see Section 2.4.1). Figure 2.1 shows the variation in penetration height with wavelength (after Friedman 1960). The penetration height is the height at which the solar flux has been attenuated to $^1/_e$ of its value outside the atmosphere. As can be seen from this figure at wavelengths shorter than 1000 Å molecular nitrogen absorbs strongly, and atomic oxygen which is the principal constituent above about 140 Km., contributes to the absorption of wavelengths shorter than 700 Å. Absorption by molecular oxygen between 1000 Å and 2000 Å leads to its dissociation and the production of atomic oxygen. This absorption is taking place at higher altitudes than the absorption by ozone in the 2000 Å to 3000 Å region. Ozone reaches its maximum concentration at an altitude of 25 Km.

THE DETERMINATION OF ATMOSPHERIC COMPOSITION

2.2.1 THE ABSORPTION LAW

When monochromatic radiation traverses through as gas, the variation of flux with distance is governed by the absorption law.

$$\phi = \phi_o \exp(-\sigma N) \qquad (1)$$

where ϕ is the flux (photons $cm^{-1}sec^{-1}$),

σ is the absorption cross section for the particular gas at the particular wavelength under consideration,

N is the number of molecules in a column of area 1 cm^2, along the path of the radiation,

and ϕo is the flux where N = 0.

{The notation used here is taken from a paper by Hinteregger (1962), which contains a detailed discussion of the interpretation of atmospheric absorption data.}

Equation (1) has serious limitations when applied to the practical situation. First, the measuring instrument would have a definite bandpass, $\Delta\lambda$, so what was being measured would be an integrated flux over $\Delta\lambda$ and not monochromatic. Second, the absorption cross-section may vary over several orders of magnitude within $\Delta\lambda$, in which case, an effective absorption cross section must be used. An example of this behaviour is given by the absorption cross section for molecular oxygen in the "oxygen window" region (see Figure 2.2). The quantity (σN) is called the optical depth. If the number density n cm^{-3} is constant over the path the absorption law can be written

$$\phi(x) = \phi o \exp(-\sigma n x) \qquad (2)$$

where $\phi(x)$ is the flux after the beam has travelled a length x cm. of the gas. The quantity $a = \sigma n$ is the absorption coefficient of the gas in cm^{-1}, at a number density n. Laboratory determinations

of the absorption coefficient are made by measuring the transmission $\phi(x)/\phi_0$ of a path length x of gas. Absorption coefficients are usually tabulated for the gas at N.T.P. (0^oC and 760 mm of Hg pressure). If a_0 is the absorption coefficient at N.T.P. then $a_0 = \sigma n_0$ where n_0 is Loschmitt's number ($2.687 \times 10^{+19} cm^{-3}$). If σ is not dependant on temperature or pressure then "a" for any other conditions of temperature T^oC and P (mm of Hg) can be obtained from the formula

$$a(T,P) = a_0 \frac{273P}{760(T + 273)} \qquad (3)$$

Equation (1) can be used to determine N from a measured transmittance once the value of σ has been determined. This method has been used extensively to determine number densities in the atmosphere by measuring the attenuation of solar ultra-violet radiation at various altitudes.

2.2.2. ATMOSPHERIC ABSORPTION

If monochromatic radiation is being absorbed by one constituent of the atmosphere the flux, at wavelength λ, $\phi(\lambda, h, z)$, is given by

$$\phi(\lambda, h, z) = \phi_0(\lambda) \exp\left[-\int_h^\infty \sigma_1(\lambda)\, n_1(h) dh \, \mathrm{Sec}\, Z\right] \qquad (4)$$

where h is the height above the earth's surface,

Z is the solar zenith angle, i.e. the angle between the direction of the sun and zenith,

$\sigma_1(\lambda)$ is the absorption cross-section of the absorbing constituent at λ,

$n_1(h)$ is the number density of the absorbing constituent,

and $\phi_0(\lambda)$ is the flux at wavelength λ on the top of the atmosphere.

Equation (4) is expressed in the simplified form involving SecZ which is valid for zenith angles less than 73°. This form assumes that the atmosphere is planar. Weeks and Smith (1968) point out that for molecular oxygen, equation (4) is in error by no more than 1% for Z<73°. However, the error is 10% at Z = 85° so that for zenith angles close to 90°, which is the case in satellite experiments and rocket experiments flown at sunrise or sunset the spherical atmosphere model must be applied. Equation (4) was used for the rocket flights considered in this work as the zenith angles were less than 73°. The spherical atmosphere model was used in analysing the WRESAT satellite results. If the sun is considered as a point source then, in the spherical atmosphere model, SecZ is replaced by the expression $(\frac{2\pi R}{H})^{\frac{1}{2}}$ where R is the radius of the earth and H the scale height (See Section 5.3.1).

In general several constituents will be absorbing the solar radiation and then equation (4) must be replaced by

$$\phi(\lambda, h, Z) = \phi_0(\lambda) \exp\left[-\int_h^\infty \sum_j \sigma_j(\lambda) n_j(h)\, dh\, \mathrm{Sec}Z\right] \qquad (5)$$

where $n_j(h)$ is the partial number density for constituent j

and $\sigma_j(\lambda)$ is the monochromatic absorption cross-section for constituent j.

The quantity $\sigma_j(\lambda)$ for a given species, j, is essentially independent of altitude although $\sigma_j(\lambda)$ may depend on kinetic temperature thus showing some possible indirect dependence on altitude. Neglect of this effect does not seem to be serious in the determination of oxygen densities.

Equation (5) may be simplified by introducing what Hinteregger calls a "weighted mean absorption cross-section" which is defined by

$$\sigma(\lambda, h) = \sum_j \sigma_j(\lambda)\, n_j(h)/n(h) \qquad (6)$$

where $n(h) = \Sigma n_j(h)$ which is the total particle number density. Equation (5) can now be rewritten as

$$\phi(\lambda, h, Z) = \phi_0(\lambda) \exp\left[-\int_h^\infty \sigma(\lambda, h)\, n(h)\, dh\, \mathrm{Sec}\, Z \right] \qquad (7)$$

The "weighted mean absorption cross-section" will vary with altitude (h) although $\sigma_j(\lambda)$ does not as the relative concentration n_j/n varies with altitude. To be completely general it is necessary to consider $\sigma(\lambda, h)$ as a function not only of wavelength (λ) and altitude (h) but also of time (t) as there are significant diurnal variations in the composition of the atmosphere. Additional independent variables such as geographic or geomagnetic latitude are also important. In practice with rocket probing experiments the experiment is only operating for a short time and quantities like solar zenith angle, latitude, longitude, diurnal variation and effects of particle fluxes are assumed to remain constant.

A quantity called the "extinction coefficient" is defined as

$$\mu(\lambda, h) = \sum_j \sigma_j(\lambda)\, n_j(h) \quad \text{so that } \sigma(\lambda\, h) \tag{8}$$

can be defined as the ratio of the "monochromatic extinction coefficient" to the total particle number density.

$\mu(\lambda\ h)$ can also be written as $= \frac{1}{\text{Sec } Z} \cdot \frac{1}{\phi} \frac{\partial \phi}{\partial h}$ (9)

$$= \frac{1}{\text{Sec } Z} \cdot \frac{\partial}{\partial h} (\ln \phi)$$

Equation (9) indicates that an "observed" extinction coefficient can be determined from the slope of a semi-logarithmic plot of measured photon flux verses altitude. The evaluation of the "extinction coefficient" does not require an absolute value of ϕ and can be derived directly from experimental flux values. Hence the extinction coefficient is the main experimentally determined quantity since the number densities can be expressed in terms of it, if the value for the cross-section is known.

So far it has been assumed that the flux measured is a monochromatic flux $\phi(\lambda, h, Z)$. In practice the quantity measured is an integral flux corresponding to the measuring instrument's band width $\Delta\lambda$. In the case of photo-electric monochromators $\Delta\lambda$ may only be about 2 $\mathring{A}$ but in the case of the ultra-violet ion chambers used in this work $\Delta\lambda$ may be from 50 $\mathring{A}$ to 300 $\mathring{A}$. The measured flux is

then given by

$$\phi(\lambda, h, \Delta\lambda, Z) = \int_{\lambda}^{\lambda+\Delta\lambda} \phi(\lambda, h, Z)d\lambda$$

$$= \int_{\lambda}^{\lambda+\Delta\lambda} \phi_0(\lambda) \exp\left[-\int_{h}^{\infty} \sigma(\lambda, h)\, n(h)\, dh\, \mathrm{Sec}\, Z \right] d\lambda \qquad (10)$$

The effective absorption cross-section is defined as

$$\sigma_{j\ \mathrm{eff}}(\lambda, \Delta\lambda, h) \equiv \int_{\lambda}^{\lambda+\Delta\lambda} \phi(\lambda, h, Z)\sigma(\lambda, h)d\lambda / \phi(\lambda, \Delta\lambda, h, Z) \qquad (11)$$

and the "effective weighted mean absorption cross-section", as,

$$\sigma_{\mathrm{eff}} = \Sigma \sigma_{j\ \mathrm{eff}}\, n_j/n, \qquad (12)$$

and an "effective extinction coefficient"

$$\mu_{\mathrm{eff}} = \sigma_{\mathrm{eff}}\, n \qquad (13)$$

The expression "effective" here refers to weighting with the spectral intensity distribution within the wavelength bandwidth $\Delta\lambda$, whereas "weighted mean" refers to weighting with the composition.

The experimental extinction coefficient as determined from the slope of a semi-logarithmic plot of measured flux verses altitude is the same as the effective extinction coefficient i.e.

$$\mu_{\mathrm{obs}}(\lambda, \Delta\lambda, h) = \frac{1}{\mathrm{Sec}\ Z} \left[\frac{1}{\phi} \frac{\partial \phi}{\partial h} \right]_{\mathrm{obs}} = \mu_{\mathrm{eff}} \qquad (14)$$

$\phi(\lambda, h)$ will, in general, vary with altitude. If one considers the radiation within the band pass $\Delta\lambda$, the more strongly absorbed parts of the spectrum will be filtered out at higher altitudes, quickly leaving a higher fraction of the radiations of wavelength at which the cross-section is smaller. The changing distribution of flux $\phi(\lambda, h)$ within the bandwidth is known as "radiation hardening". As $\phi(\lambda, h)$ varies with altitude so will

$\sigma_{j\ eff}$ for some given wavelength band-pass $\Delta\lambda$. This variation is in addition to the weighted mean resulting from variable composition. If only direct radiation from the sun is considered, the character of this additional dependence can only be an increase of σ_{eff} with height, i.e.

$$\frac{\partial(\sigma_{eff})}{\partial h} > 0 \qquad (15)$$

By using the "effective extinction coefficient" then

$$\phi(\lambda, \Delta\lambda, h, Z) = \phi_0(\lambda, \Delta\lambda) \exp\left[-\int_h^\infty \mu_{eff} dh \ \mathrm{Sec}\ Z\right] \qquad (16)$$

where the integral represents the "effective optical depth", $\tau_{eff}(\lambda, \Delta\lambda, h, Z)$ of the atmospheric slant column along the solar ray to the point of observation.

Accurate experimental attenuation measurements in the low attenuation region $\phi_0 - \phi(h) << \phi_0$ are very difficult. Ideally they require very accurate measurements of $\phi(h)$ and reference measurements of the time rate of change of the incident flux $\partial\phi_0/\partial t$ at the top of the atmosphere from a satellite. In the absence of satellite measurements of $\partial\phi_0/\partial t$ the best values of $\mu_{eff}(\lambda, h)$ are derived from that section of the experimental $\phi(h)$ - curve for which the slope $d\phi/dh$ is greatest. In this region the error in taking the observed slope $d\phi/dh$ instead of the correct slope, $\partial\phi/\partial h$ is usually the smallest.

The correct slope is given by the expression,

$$\frac{\partial \phi}{\partial h} = \left(\frac{d\phi}{dh}\right)_{obs} \mp \frac{\partial \phi}{\partial t} / V,$$

where V designates the vertical motion of the rocket and the signs $\mp$ refer to ascent and descent respectively. At the peak of the rocket's trajectory (small V) and if no reference measurements are made from a satellite then from the above equation it can be seen that the largest errors in extinction coefficient will be in the low attenuation region (large ϕ, small $d\phi/dh$).

Errors can also be large in the region where ϕ is small even though V is large. These errors are obtained from difficulty in measuring $d\phi/dh$.

2.2.3. ABSORPTION OF SOLAR ULTRA-VIOLET RADIATION BY MOLECULAR OXYGEN

From Figure 2.1, at wavelengths less than 1000 $\mathring{A}$, molecular oxygen, molecular nitrogen and atomic oxygen all contribute to atmospheric absorption. To solve for $n_j(h)$ the extinction coefficient must be measured at at least three wavelengths.

Between 1000 $\mathring{A}$ and 1700 $\mathring{A}$ atmospheric absorption is due almost entirely to molecular oxygen. The extinction coefficient for molecular oxygen is very much greater than the sum of the

extinction coefficients for other constituents, i.e.

$$\sigma_{O_2}(\lambda)n_{O_2}(h) >> \sigma_2(\lambda)n_2(h) + \sigma_3(\lambda)n_3(h) + \text{etc.} \qquad (17)$$

in the height range where $\partial\phi/\partial h$ is a maximum.

Under condition (17) equation (13) becomes

$$\mu_{eff}(\lambda, \Delta\lambda, h) = \sigma_{O_{2eff}}(\lambda, \Delta\lambda, h)n_{O_2}(h) \qquad (18)$$

where $$\sigma_{O_{2eff}}(\lambda, \Delta\lambda, h) = \frac{\int_{\lambda}^{\lambda+\Delta\lambda} \phi(\lambda hZ)\sigma_{O_2}(\lambda)d\lambda}{\phi(\lambda, \Delta\lambda, h, Z)} \qquad (19)$$

As ion-chambers have a large band-pass ($\Delta\lambda$), and the solar flux $\phi_0(\lambda)$ and the molecular oxygen absorption cross-section $\sigma_{O_2}(\lambda)$ (see Sections 1.2.2. and 2.3.1) vary widely with wavelength within the range 1000 Å to 1700 Å it would appear that any derivation of molecular oxygen densities would be extremely complicated. In the cases of several ion chambers flown, which operate in the "oxygen window" region (see Fig. 2.2), the effective absorption cross-section has been so variable that oxygen densities were not derived from these chambers (see Section 4.3.1.).

Equations (18) and (19) can be simplified in certain cases;

(a) When $\sigma_{O_2}(\lambda)$ is constant over the ion chamber's band-pass $\Delta\lambda$. The effective molecular oxygen absorption cross-section becomes equal to

$$\sigma_{O_2}(\lambda)$$

and the extinction coefficient,

$$\mu(\lambda, \Delta\lambda, h) = \sigma_{O_2}(\lambda)n_{O_2}(h) \qquad (20)$$

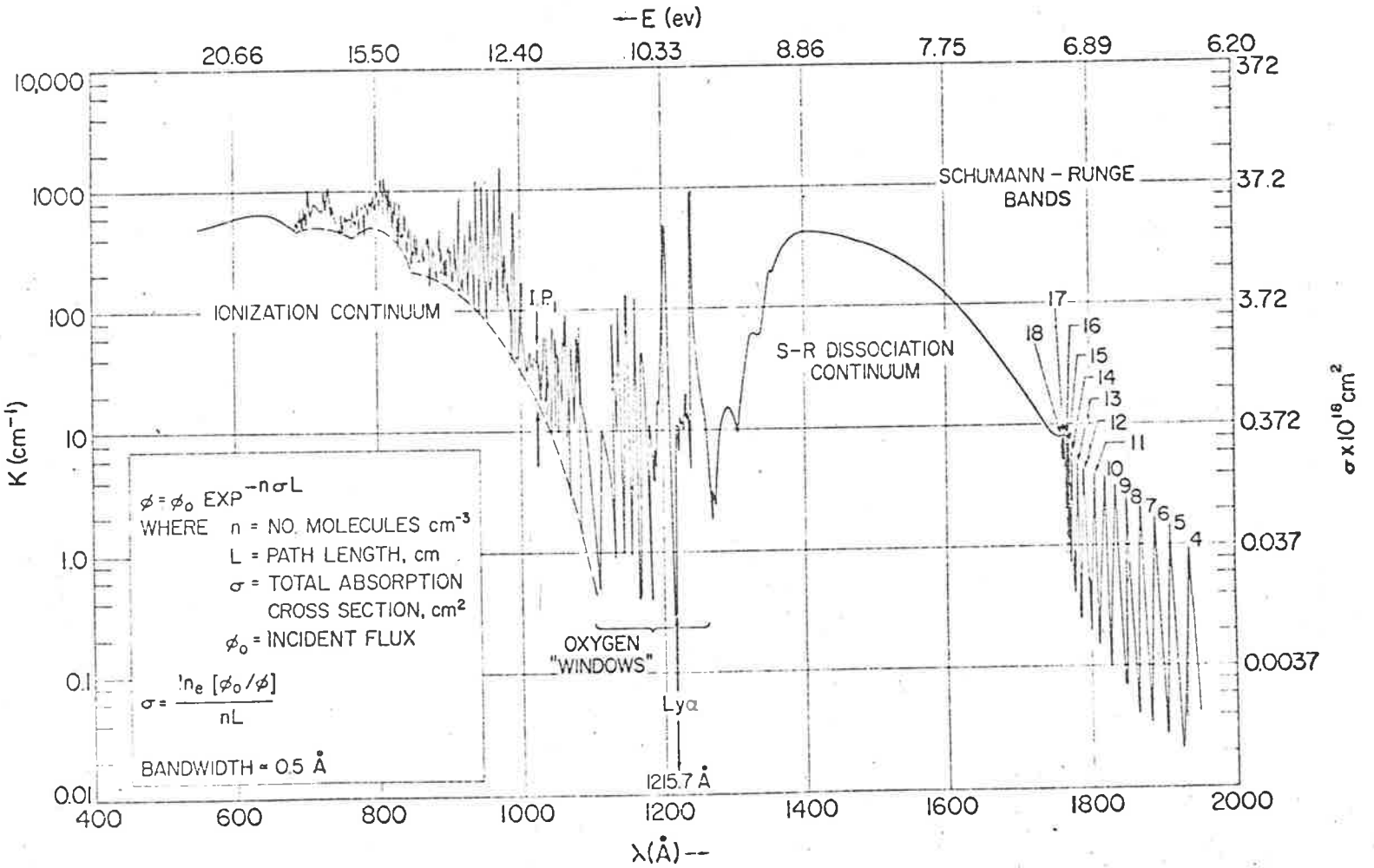

Fig. 2.2. The absorption spectrum of molecular oxygen (from Cook and Ching, 1965).

An example of this behaviour is provided by the ion chamber with a sapphire window and xylene filling which responds to the range 1420 to 1470 Å. Within this range the absorption cross-section varies little (see Section 2.3.1) and equation (19) and equation (20) are good approximations. Other ion chambers, i.e. the quartz window, triethylamine filling and the barium fluoride window-toluene filling which operate within the range 1350 to 1410 Å and 1570 to 1680 Å also fall into this category.

(b) If a solar emission line dominates the spectral intensity within the bandwidth of the ion chamber ($\Delta\lambda$), then the bandwidth can be reduced to the bandwidth across this line. An example is provided by an ion chamber, such as the one with a lithuim fluoride window and nitric oxide filling, which responds to the range 1050 to 1350 Å. The Lyman-α line (1215.7 Å) which accounts for 80% of the solar intensity occurs within this range. Also, by coincidence, the Lyman-α line corresponds to a very sharp minimum in $\sigma_{O_2}(\lambda)$ (see Section 2.3.1) which means that most of the other wavelengths within the range 1050 to 1350 Å will be absorbed at much higher altitudes. From Figure 2.1 it can be seen that Lyman-α penetrates to approximately 70 Km. whereas most of the other wavelengths

within this range are effectively absorbed above 90 Km. These penetration heights quoted depend on the solar zenith angle (see Section 2.2.4).

With the lithium fluoride-nitric oxide ion chamber, within the height range 70 to 90 Km. where $\frac{\partial \phi}{\partial h}$ is a maximum, measurements are taken of the almost monochromatic flux at Lyman-α. The extinction coefficient in this case becomes :-

$$\mu(\lambda, \Delta\lambda, h) = \sigma_{O_2}(L\alpha)\, n_{O_2}(h) \qquad (21)$$

to a very close approximation and so considerably simplifies the mathematics.

2.2.4 HEIGHT RANGE FOR DETERMINING OXYGEN DENSITIES

To illustrate that there is a practical limit to the height range over which molecular oxygen densities can be determined on one value for the absorption cross-section, consider the following simplified situation which is applicable to the lithium fluoride-nitric oxide ion chamber. Assume,

(a) the absorption is due only to molecular oxygen,

(b) the molecular oxygen absorption cross-section is constant over the range $\Delta\lambda$, and

(c) the number density of molecular oxygen varies exponentially with height, i.e.

$$n(h) = n_0 \exp(-h/H) \qquad (22)$$

In equation (22), H is the scale height for molecular oxygen. From equation (16)

$$\phi(\lambda, \Delta\lambda, h) = \phi_0(\lambda, \Delta\lambda) \exp(-\tau) \tag{23}$$

and by definition the penetration height h* is the height at which $\tau = 1$, i.e.

$$\int_{h^*}^{\infty} \mu(\lambda, \Delta\lambda, h)\, dh \sec Z = 1 \tag{24}$$

Under the above assumptions,

$$\mu(\lambda, \Delta\lambda, h) = \sigma n(h) = \sigma n_0 \exp(-h/H) \tag{25}$$

from equation (24) and,

$$\tau = \sigma n_0 H \sec Z \exp(-h/H) \tag{26}$$

Using equations (23) and (24) the variation of ϕ with height can be tabulated as shown in Table 1.

TABLE 1

h	τ	ϕ/ϕ_0
h* + 4H	.02	0.98
h* + 3H	.05	0.95
h* + 2H	0.14	0.87
h* + H	0.37	0.69
h*	1	0.37
h* - H	2.7	0.067

It can be seen that 90% of the absorption takes place over a height range of four scale heights.

Since from equation (26)

$$\sigma n_0 H \text{ Sec } Z \exp(-h^*/H) = 1$$

the value of h* will be changed by altering the zenith angle Z but the values given in Table 1 will not be affected. Therefore, the absorption takes place higher up but over the same range of heights. As the zenith angle changes from 0 to Z the absorption moves up by an amount H* given by:

$$\text{Sec } Z = \exp\left(\frac{H^*}{H}\right)$$

Values for H*/H are given in Table 2.

TABLE 2

Z	H*/H
0°	0
10°	0.01
30°	0.14
50°	0.44
70°	1.07

It can be seen from Table 2 that even for a large variation in zenith angle the range over which oxygen densities can be determined is not raised by a large amount. This statement is

exactly true, only for a planar atmosphere with the assumptions made above. With the lithium fluoride-nitric oxide ion chamber at zenith angles less than 70°, the normal height range for determining oxygen densities is restricted to 70 to 90 Km. However, using large zenith angles by making rocket flights near sunrise and sunset, is a technique used successfully by Weeks and Smith (1968). When dealing with large zenith angles the spherical atmosphere model must be used and not the planar model used above. Weeks and Smith obtained a range of 94 to 112 Km. by using a zenith angle of 95° with a lithium fluoride-nitric oxide ion chamber.

2.3.1. THE ABSORPTION CROSS-SECTION OF MOLECULAR OXYGEN

The absorption of vacuum ultra-violet radiation by molecular oxygen has been investigated by numerous workers. Detailed measurements were made by Watanabe et al. (1953), Metzger and Cook (1964), Blake et al. (1966) and Ogawa (1968) using photo-electric techniques. The absorption spectrum of molecular oxygen is shown in Figure 2.2 {from Cook and Ching (1965)}. At wavelength shorter than 1300 Å, the spectrum shows a number of absorption bands separated by "windows" of much lower absorption cross-section. The most important "window" is that which coincides with the Lyman-α line. Even though this window is extremely narrow there is an almost exact coincidence of

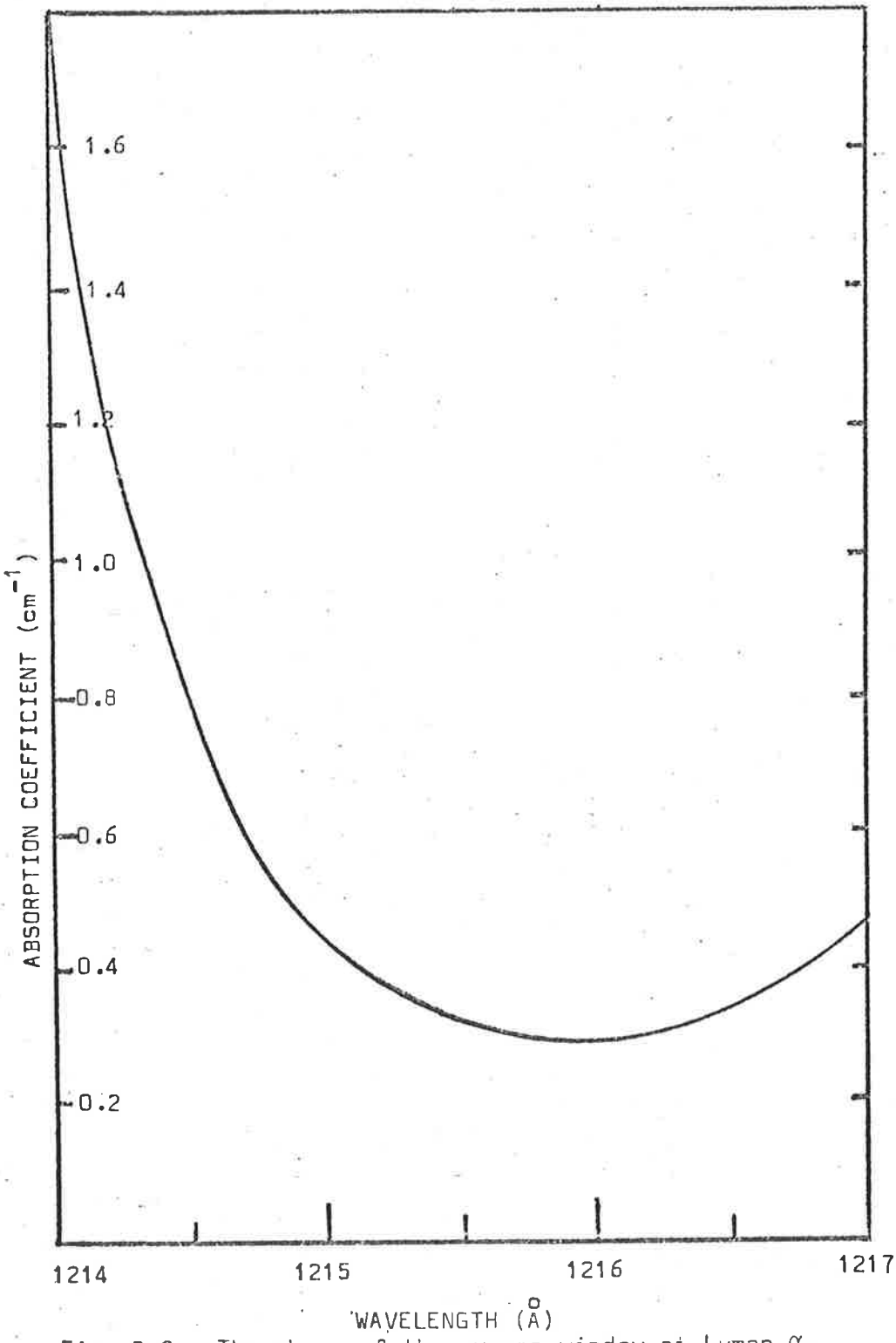

Fig. 2.3 The shape of the oxygen window at Lyman-α.
(after Blake et al 1965, unpublished).

the centre of the window with that of the line. It can be seen that within the range 1050 to 1700 Å, the range covered by ion chambers this window has the lowest value for the cross-section.

At wavelengths larger than 1300 Å and extending to about 1750 Å is the Schumann-Runge dissociation continuum which reaches a maximum absorption cross-section of 1.48×10^{-18} cm^2 at 1425 Å. At wavelengths larger than 1750 Å commence the Schumann-Runge bands where the average absorption cross-section decreases with increasing wavelengths until they merge into the Hertzberg continuum.

2.3.2. THE ABSORPTION CROSS-SECTION AT LYMAN-α

The shape of the "oxygen window" at Lyman-α is shown in Figure 2.3 (Blake 1965 unpublished). The cross-section at the bottom of the window is constant over the width of the Lyman-α line but is pressure dependent, increasing linearly as the pressure is increased (Preston 1940, Blake et al. 1966). As the rate of increase is 1.7×10^{-23} cm^2 $torr^{-1}$ and the value for the cross-section is about 10^{-20} cm^2 the pressure dependence is negligible for the range of pressures encountered between 70 and 90 Km. Values for the cross-section obtained by different workers using a photo-electric techniques are shown in Table 3.

Photographic techniques were used by other workers Ditchburn et al. (1954) and Lee (1955) obtaining values of 0.84×10^{-20} cm^2 and 0.85×10^{-20} cm^2 respectively but neither mentioned any pressure dependence. A value of 1.00×10^{-20} cm^2 for the cross-section has been used in the present work.

TABLE 3

Investigation	Cross-section	Pressures
Preston (1940)	$1.04 \times 10^{-20} cm^2$	Extrapolated to zero pressure
Watanabe (1953)	$1.00 \times 10^{-20} cm^2$	Extrapolated to zero pressure
Metzger and Cook (1964)	$1.04 \times 10^{-20} cm^2$	9.3 torr
Blake et al. (1966)	$1.12 \times 10^{-20} cm^2$	Extrapolated to zero pressure
Ogawa (1968)	$\left.\begin{matrix}1.03\\1.13\end{matrix}\right) \times 10^{-20} cm^2$	1.2 - 6.3 torr

2.4.1. ABSORPTION BY OTHER CONSTITUENTS IN THE ATMOSPHERE

Table 4 shows the constituents in the air in the homosphere which should be considered when dealing with solar ultraviolet absorption.

TABLE 4

Constituent	Fraction by Volume
Nitrogen	.7808
Oxygen	.2095
Argon	.00934
Carbon dioxide	3×10^{-4}
Water Vapour	$10^{-2} - 10^{-5}$
Ozone	$10^{-5} - 10^{-7}$
Nitric Oxide	$10^{-6} - 10^{-9}$

For the major constituents the U.S. Standard Atmosphere (1962) was the reference. For the minor constituents see text.

The minor constituents concentrations are determined by chemical and photochemical reactions and so are rather variable. Very little direct experimental evidence has been obtained for constituents like water vapour, carbon dioxide ozone and nitric oxide and theoretical estimates have to be used for the region

above 70 Km. In the following each constituent will be discussed in terms of absorption cross-section between 1000 and 2000 Å.

(a) Molecular Nitrogen

The absorption spectrum for nitrogen above 1000 Å consists of several band systems, corresponding to forbidden transitions which are very weak. The Lyman-Birge Hopfield bands from 1130 Å to 1450 Å are the principal ones but even these have very small cross-sections. Upper limits which have been obtained for wavelengths in the vicinity of Lyman-α are 3×10^{-22} cm^2 (Watanabe et al. 1953), 6×10^{-23} cm^2 (Ditchburn et al. 1954) and Lee (1955) found the cross-section to be less than 2×10^{-21} cm^2 at all wavelengths above 1040 Å. At Lyman-α the lowest upper limit for the cross-section is 6×10^{-23} cm^2. Using this value, the fraction of the absorption due to nitrogen is less than 2% of that due to oxygen at Lyman α.

(b) Carbon Dioxide

The absorption spectrum of carbon dioxide is given in Figure 2.4 (from Inn et al. 1953). As can be seen from this spectrum the average cross-section is the order of 10^{-18} cm^2. There is a large continuum extending from 1200 Å to 1700 Å and very strong bands occurring at wave-

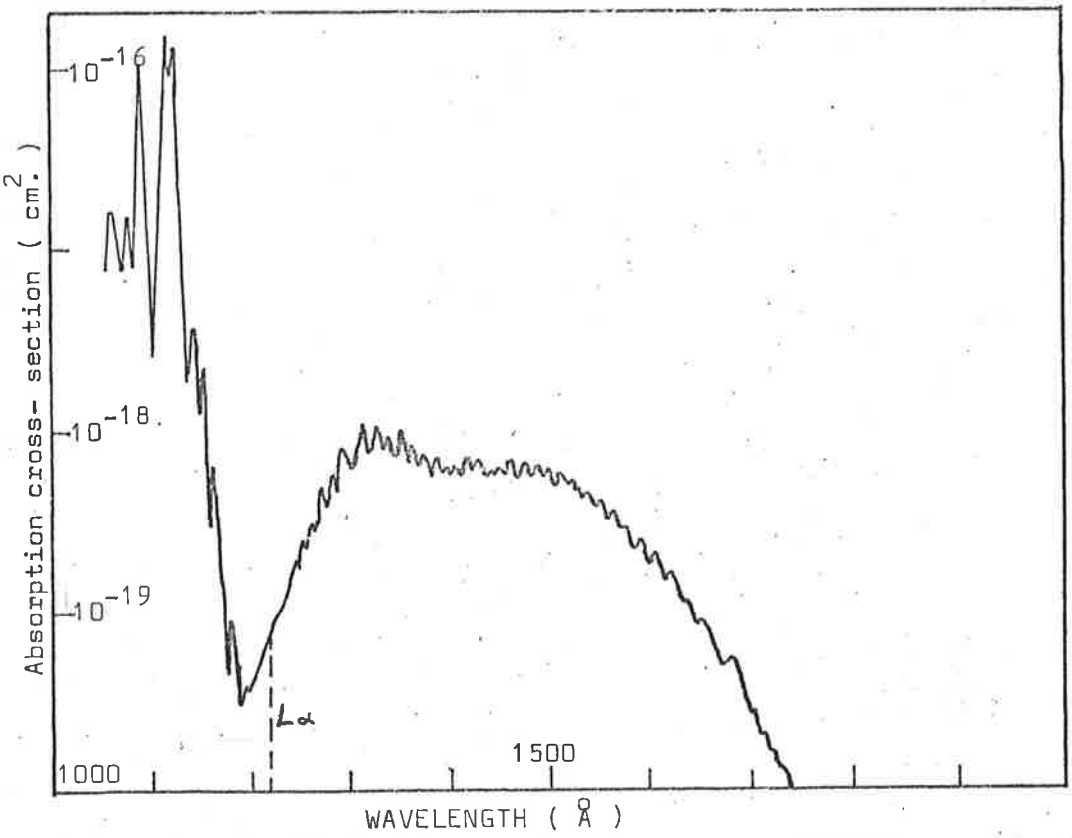

Fig. 2.4. The absorption spectrum of carbon dioxide.
(Inn et al , 1953)

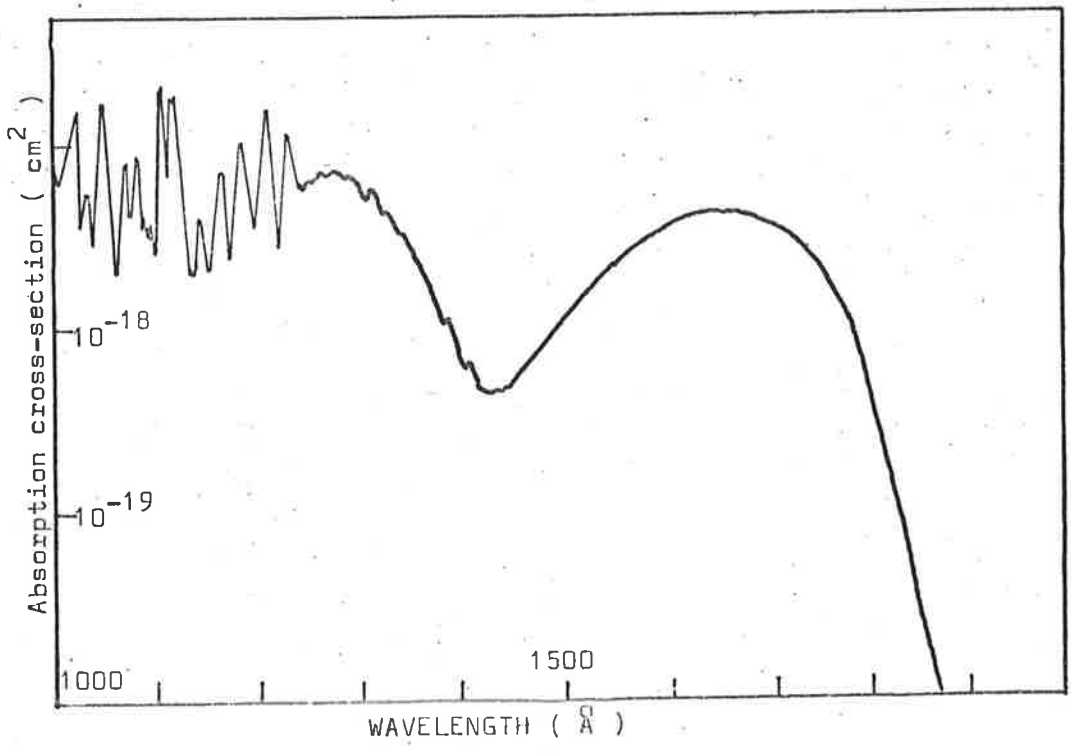

Fig. 2.5. The absorption spectrum of water vapour.
(Watanabe and Zelikoff, 1953)

lengths less than 1200 Å. Lyman-α lies very close to the minimum between the continuum and the bands with a cross-section value of 7.3×10^{-20}, which is larger than that for oxygen. As this cross-section is larger than that of oxygen at Lyman-α even small concentrations of carbon dioxide may make some contribution to the absorption of Lyman-α. In the region from 70 to 90 Km. there is no experimental evidence concerning the concentration of carbon dioxide, although it has been stated {Bates and Witherspoon (1952)} that photo-dissociation of carbon dioxide takes place above 100 Km. If the concentration of carbon dioxide is constant up to 90 Km., then the absorption of Lyman-α due to carbon dioxide is only 1% of that due to oxygen.

(c) Water Vapour

Figure 2.5 shows the absorption spectrum of water vapour (Watanable and Zelikoff 1953). The main features of this curve are a series of bands below 1250 Å in which the cross-section varies from 2×10^{-18} cm^2 to 2×10^{-17} cm^2, and two continua peaking at 1300 Å and 1650 Å where the cross-section is 8×10^{-18} cm^2 and 4.5×10^{-18} cm^2 respectively. Lyman-α occurs in the band structure near a maximum in the absorption spectrum. The value for the

cross-section at Lyman-α has been determined by several workers. Watanabe and Zelikoff (1953) determined a value of 1.45×10^{-17} cm^2 and Ditchburn et al. (1954) a value of 1.34×10^{-17}. This value being 1.3×10^3 greater than that used for oxygen means that small concentrations of water vapour could drastically affect the measurements at Lyman-α. Water vapour inside the lithium fluoride window-nitric oxide filling ion chamber can seriously affect the spectral response as the band structure in the water vapour absorption spectrum occurs within the wavelength band pass of this chamber.

As in the case of carbon dioxide there has been no experimental determination of water vapour concentrations above 70 Km. Bates and Nicolet however, have produced a theoretical profile for water vapour, and using their values, the absorption due to water vapour, relative to that due to oxygen is 4.0% at 70 Km. and 0.1% at 90 Km.

The occasional appearance of noctilucent clouds near 80 Km., in summer at latitudes above 45^o must lead to uncertainty concerning the concentration of water vapour above 70 Km. Chapman and Kendall (1965) have analysed the conditions which lead to the formation of these clouds and concluded that water vapour is carried up to 80 Km.

by convection and there condenses onto dust particles. As these clouds are rare, if this process occurs then it must be a rare occurrence and should not affect the overall concentration of water vapour in this region.

(d) Ozone

The absorption spectrum of ozone is shown in Figure 2.6. It can be seen from this figure that ozone absorbs strongly with a continuum extending from 1350 to 2000 Å and very mild band structure below 1350. As in the case of water vapour, the Lyman-α line lies near a maximum in the absorption spectrum of ozone. A value for the cross-section at Lyman-α was found by Tanaka et al (1953) to be 2.3×10^{-17} cm^2.

The concentration of ozone above 70 Km. has been studied both theoretically by Johnson et al (1952), Barth (1961) and Hunt (1965) and experimentally by use of satellite {Rawcliffe et al (1963)}. The concentration of nocturnal ozone above 70 Km. has been determined by Carver, Horton and Burger (1966). Their technique involved measuring the absorption of solar radiation reflected from the moon. The absorption of wavelength bands centered at 2400 Å, 2500 Å, 2650 Å and 2900 Å was measured by using an interference filter-photo-

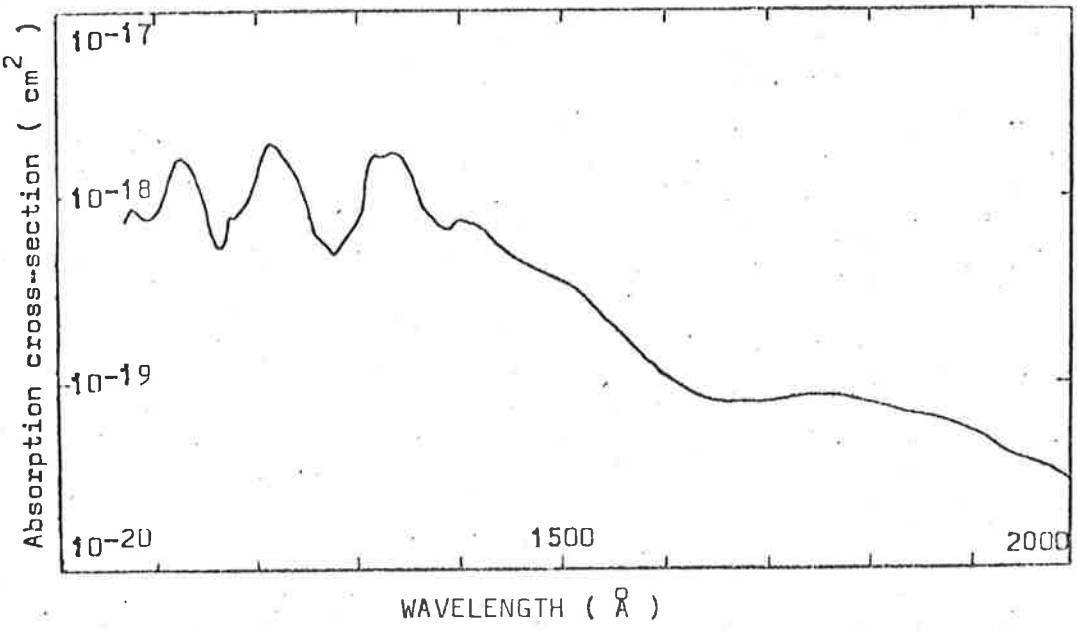

Fig. 2.6. The absorption spectrum of ozone. (Tanaka et al, 1953)

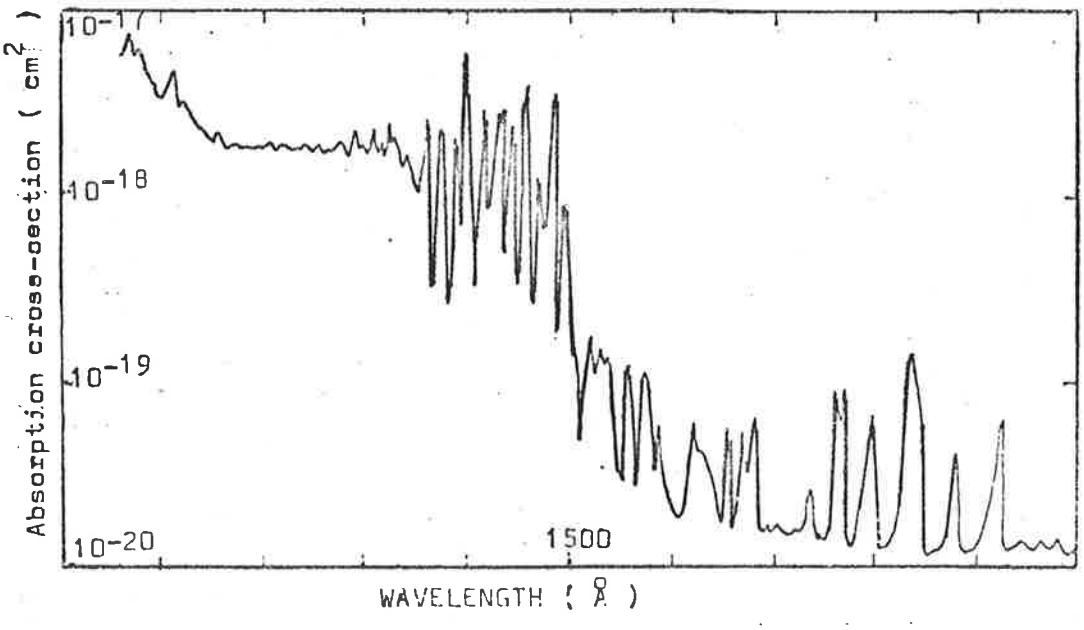

Fig. 2.7. The absorption spectrum of nitric oxide. (Marmo, 1953)

multiplier combination. Carver and Horton's results indicated that the concentration of nocturnal ozone at 70 Km. was 2 x 10^9 mols cm^{-3}. Rawcliffe's results give the number density of ozone as 10^9 mols cm^{-3} at 70 Km. ranging to 10^8 mols cm^{-3} at 90 Km. which gives an absorption due to ozone varying from 0.67% at 70 Km. to 1.26% at 90 Km. of that due to oxygen.

(e) Nitric oxide

The absorption spectrum of nitric oxide is shown in Figure 2.7. Violent band structure characterizes this spectrum above 1300 Å, during which the absorption cross-section can vary by a factor of 10. Below 1300 Å a continuum exists. At Lyman-α the cross-section has a value of 2.5 x 10^{-18} cm^2 (Marmo 1953).

The concentration of nitric oxide has been determined by Barth (1965) for the 70 to 90 Km. region who found it to be the order of 6 x 10^7 mols cm^{-3}. This corresponds to an absorption of nitric oxide relative to oxygen of 0.1% at 90 Km. at Lyman-α.

(f) Inert gases

The inert gases, which have ionization limits of 575Å (Ne), 787 Å (A) and 886 Å (Kr) exhibit continuous

absorption only below their first ionization limits and so can be neglected in considering absorption in the range 1000 to 1700 Å. Atomic nitrogen and atomic oxygen which have first ionization limits at 852 Å and 910 Å, respectively, can also be neglected.

In the present work, no corrections have been applied for absorption of gases other than oxygen. Due to the uncertainty in the concentration of constituents, the exact contributions to the absorption of Lyman-α is doubtful, but should not be more than seven percent.

CHAPTER 3. CONSTRUCTION AND PROPERTIES OF THE DETECTORS USED IN THE ROCKET EXPERIMENTS

3.1.1. INTRODUCTION

Various types of detector have been used in rockets for studying solar ultra-violet radiation. Dispersive instruments, with narrow fields of view may be used only if the rocket has a pointing control (see Chapter 1). Non-dispersive instruments with large fields of view, and high sensitivity, should be used in rockets without a pointing control facility. Two basic types of non-dispersive detector are used:- (a) those which use the photoelectric effect at the surface of a solid, and (b) those which use the photo-ionization of a gas. Photomultipliers and photodiodes, with interference filters which are used to restrict the spectral response to narrow spectral bands above 2000 $\mathring{A}$ fall into the first category. Alternatively, photo-multipliers and photodiodes can have their spectral responses limited separately on the short and the long wavelength side. Many materials, i.e. lithium fluoride, calcium fluoride, only transmit radiation from a certain limit and can be used to limit the short wavelength side. By varying the types of photocathodes, i.e. C_S-T_e, C_S-I some control can be made on the long wavelength side. These materials, even though they have high sensitivities in the vacuum ultra-violet region do not have sharp cut-offs; their sensitivity decreasing over several hundred angstroms. Pure metals such as nickel and tantalum have also been used as photocathodes.

Detectors employing the photo-ionization of a gas, of which the ion chamber is an example, use window materials like lithium fluoride, calcium fluoride, and sapphire to control the low wavelength cut-off which is sharp in the majority of cases. The gas inside the ion chamber provides a definite upper limit to the wavelength sensitivity as a gas molecule can only be ionized by a photon of energy greater than the first ionization potential of the molecule. Although the first ionization potential decreases with an increase in temperature of the gas, the effect which is due to thermal excitation of the molecule, is small in practice {Carver and Mitchell (1967)}. The number of photoelectrons produced per photon absorbed in the gas is defined as the photo-ionization efficiency which is usually greater than 10%. For most gases there is a small variation in the photo-ionization efficiency with wavelength and molecules which have an efficiency that decreases sharply at the cut-off are most suitable for ion chambers. The types of gases in use are simple diatomic molecules (nitric oxide), alkyl halides (ethyl chloride, ethyl iodide), aromatic compounds (benzene, toluene, xylene), tertiary amines (triethylamine) and ketones (acetone).

Photoelectric emission from the walls or the central wire of an ion chamber can prevent a sharp cut-off for long wavelengths. This effect is normally negligible as the photoelectric yield of metals rapidly decreases as the wavelength increases. The short wavelength radiation, which is most effective in releasing electrons will be

absorbed by the filling gas before it reaches the walls. Photo-electric emission can be reduced if the central wire of the ion chamber is the cathode and the walls, the anode. In this mode, if any photoelectron is emitted from the wall, then it is immediately attracted back to the wall ; opposite from that of Geiger counters. The voltage applied to an ion chamber is normally less than 100 V, hence as there is no gas amplification involved, the electric field around the central wire is not as critical as that in the Geiger counter. Chubb and Friedman (1955) found that the photoelectric yield of a surface is decreased in the presence of the filling gas particularly an electro-negative gas such as nitric oxide.

Detectors using the photo-ionization of a gas together with an appropriate window were first used by Chubb and Friedman (1955). Their detectors were Geiger counters which proved rather unreliable in use, their sensitivity changing with time. Ion chambers with machined copper bodies replaced these Geiger counters (Friedman et al 1958). Ion chambers with ceramic bodies and gold interior walls have also been used at the Goddard Space Flight Center (Stobber et al 1963) and by the Meteorological Office, Bracknell).

3.2.1 CONSTRUCTION OF THE ION CHAMBERS

Figure 3.1 shows a cross-sectional diagram of an ion chamber used in the present work. These ion chambers are identical to those

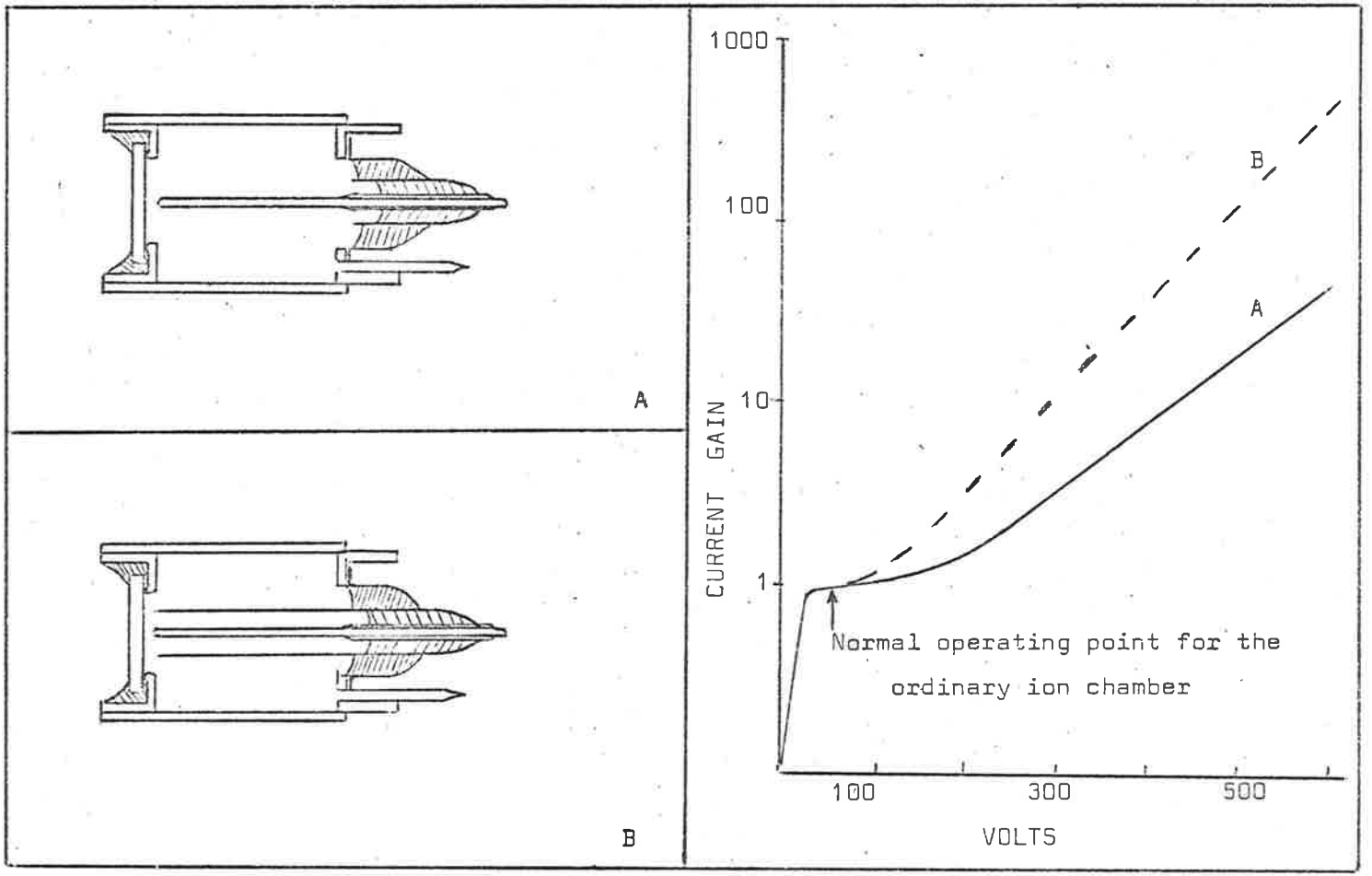

Fig. 3.1. A composite diagram showing the cross section of the ordinary (A) and gas gain ion chambers. The graphs on the right indicate the current- voltage characteristics for the ion chambers.

used by Mitchell (1966) and described by Carver and Mitchell (1964). The body of the ion chamber consisted of a piece of one inch copper tubing into which copper end pieces were soldered. A length of annealed 0.052" I.D. copper tubing was soldered into the back of the ion chamber. A 1 mm diameter ground tungsten rod formed the cathode which was supported by a kovar-glass seal. A guard ring was included in the seal to minimize the effects of leakage currents. A leakage resistance of greater than 10^{13} ohm existed between the guard ring and either of the electrodes. Soft silver solder was used in assembling the chamber although recently the chamber has been assembled with epoxy resin, as considerable difficulty was found in cleaning the inside of the chamber without affecting the soft silver solder with cleaning acids. Connecting leads were attached to the tungsten wire, guard ring and outside case and the window materials were attached with epoxy resin after the chamber had been thoroughly tested for leaks.

The body of the chamber was tested for leaks by fitting a brass blank, with an O-ring seal, to the copper end piece normally holding the window. The copper body was evacuated through the filling tube sealed to the vacuum system by a double O-ring port. Six ports were on the system so that a maximum of six ion chambers could be pumped down (and filled, with the same gas) at once. The vacuum system used (see Figure 3.2) was a glass-metal system fitted with a two inch diffusion pump which enabled the system to be evacuated to less than

Fig. 3.2. The vacuum system used for filling the ion chambers. Three ion chambers are connected to the system by means of their filling tubes. The oil manometer shown was used to adjust filling gas pressures.

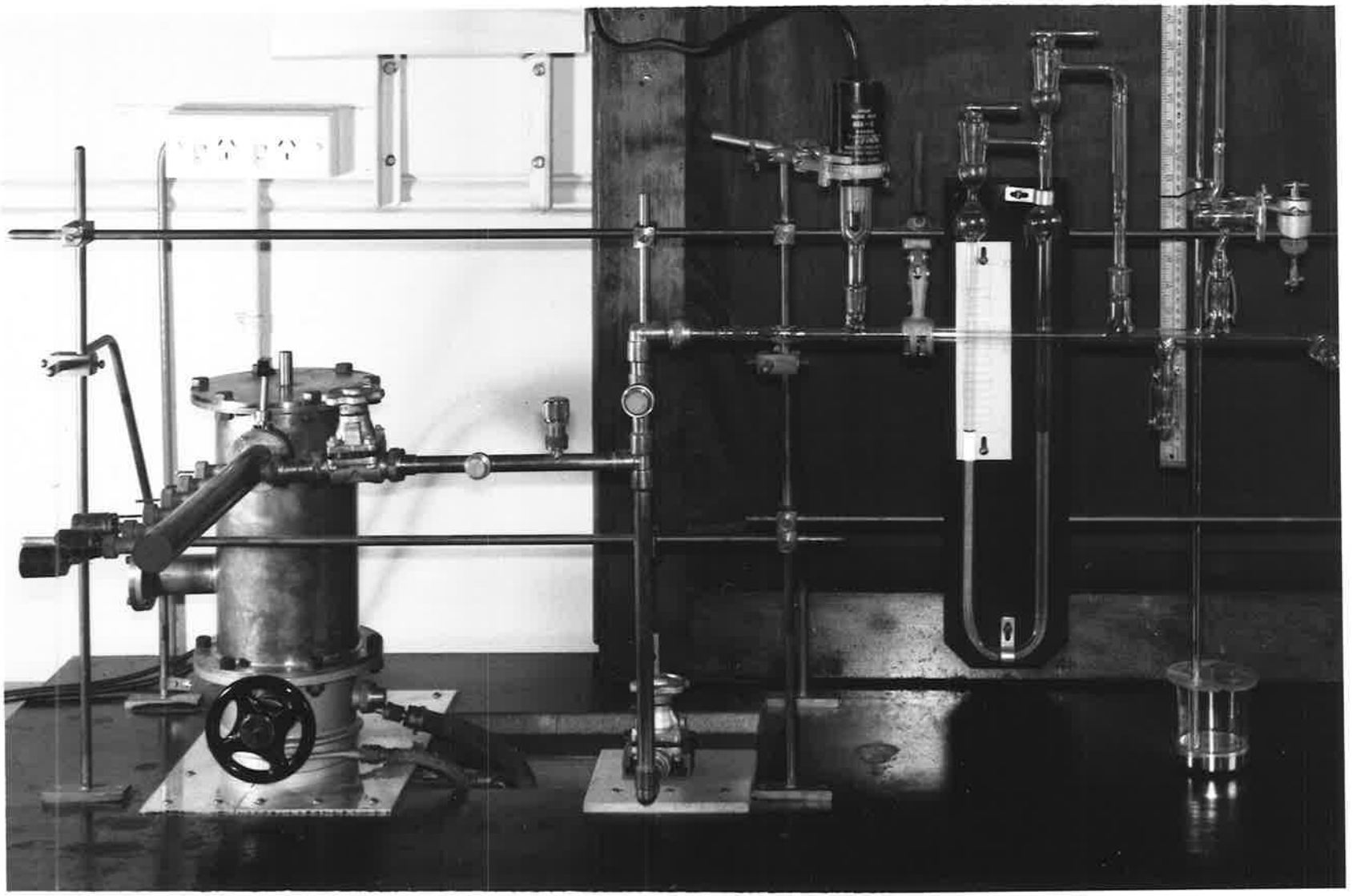

10^{-5} torr. Pressure measurements were made with an oil manometer (used for the measurement of filling gas pressures), Pirani gauge and an ionization gauge.

The window materials used are summarized in Table 3.1.

TABLE 3.1

Window Material	Window Size	*Transmission limit
lithium fluoride	3/4" diam. x 1.5 mm thick	1050 Å
calcium fluoride	3/4" diam. x 1.5 mm thick	1220 Å
Barium fluoride	3/4" diam. x 1.5 mm thick	1350 Å
Sapphire	3/4" diam. x .02" thick	1420 Å
Quartz	3/4" diam. x 1/16" thick	1560 Å

The quartz window listed was actually a highly refined quartz called "Spectrosil A". This has a much lower cut-off than normal quartz which has a transmission limit of approximately 1800 Å. As the window sizes differ slightly in thickness the angular response of the ion chambers should also differ slightly. However, by comparing the in flight angular responses of different ion chambers from the Long Tom rocket flight this effect was found to be negligible.

---

*The figures quoted under "Transmission limit" are the wavelengths at the short wavelength cut-off i.e. barium fluoride will transmit only above 1350 Å.

For the design of an efficient ion chamber the filling gas pressure must be adjusted so that the incident ultra-violet radiation is totally absorbed in the gas. The absorption coefficients of the various filling gases were determined by Carver and Mitchell (1964)* with the exception of nitric oxide which was determined by Watanabe (1954). Table 3.2 lists the filling gases together with the pressures used to ensure that most of the ultra-violet radiation entering the ion chambers would be completely absorbed.

TABLE 3.2

Gas	Filling Pressures	Photo Ionization Threshold
Nitric oxide	15-20 mm of Hg	1350 Å
Ethyl chloride	13 mm of Hg	1130 Å
Ethyl bromide	6.8 mm of Hg	1200 Å
Ethyl iodide	15 mm of Hg	1330 Å
Toluene	10 mm of Hg	1410 Å
p-Xylene	4.0 mm of Hg	1470 Å
Benzene	8.0 mm of Hg	1340 Å
Acetone	7.8 mm of Hg	1290 Å
Triethylamine	9.5 mm of Hg	1660 Å

Carbon disulphide (photo-ionization threshold of 1240 Å) and Mesitylene (photo-ionization threshold of 1480 Å) have also been used as ion chamber filling gases. Lithium fluoride-carbon disulphide ion chambers have been flown in rockets but in-flight sensitivity

---

*In this paper there is a numerical error in the results. The absorption coefficients for the gases are a factor of 10 too low.

variations were found. These were believed to be due to degradation of carbon disulphide under the action of ultraviolet radiation (Smith et al 1965); laboratory tests by Carver and Mitchell (1967) have confirmed this conclusion. Mesitylene does not offer any advantages over p-Xylene as a filling gas but has the disadvantage that it is extremely difficult to remove completely from the vacuum system used for filling the chambers. Because of these disadvantages carbon disulphide and mesitylene have not been used in the present work. By using combinations of the window materials listed in Table 3.1 and the gases of Table 3.2 a large number of ion chambers may be constructed to cover the wavelength range 1050 - 1660 Å. The most commonly constructed ion chambers were those used in the Long Tom rocket flight (see Table 4.1).

Most compounds listed in Table 3.2 are liquids at room temperature. A glass phial, which contained 1 cc of liquid was mounted on the vacuum system and the vapour from these liquids allowed to flood the system and hence fill the ion chambers. The ultimate pressure obtained from these compounds was limited by the vapour pressure of the liquid at room temperature. Unfortunately, most of the gases used adversely affected the oil in the backing pump and oil manometer. This necessitated frequent changing of these oils and long periods of pumping out between filling chambers with different gases.

The nitric oxide, being a gas, was purified and stored in a one litre spherical glass flask. This flask was attached to the vacuum

system and the nitric oxide admitted through a series of taps to the ion chambers. Purification of the nitric oxide was performed with the apparatus shown in Figure 3.3. The impure nitric oxide was obtained either from a cylinder or prepared chemically, in either case, the nitric oxide contained other oxides of nitrogen and water vapour. These impurities were removed by passing the nitric oxide through two U-tubes containing silica-gel, which were surrounded by a "slush" mixture containing 50% chloroform and 50% carbon tetrachloride. This mixture was partially solidified by adding liquid air and once prepared was a non-inflammable mixture at a temperature of $-80^{o}C$ which was sufficient to liquify nitrous oxide, nitrogen dioxide and water vapour, whilst still allowing the nitric oxide to pass. Silica-gel was included as an extra precaution against water vapour. The complete apparatus was initially flushed with argon to remove any traces of air so that the nitric oxide would not combine to form nitrous oxide and nitrogen dioxide.

Once the ion chamber was filled with the appropriate gas, it was removed from the vacuum system by cutting the filling tube with a pair of pinchers which formed a cold weld and hence a vacuum tight seal. The seal was protected by dipping the weld into a bath of solder. The use of a soldering iron was unsuitable for this process for localized heat may have broken the weld and introduced a leak. A portable hydrogen lamp was used to check that a leak had not developed in the

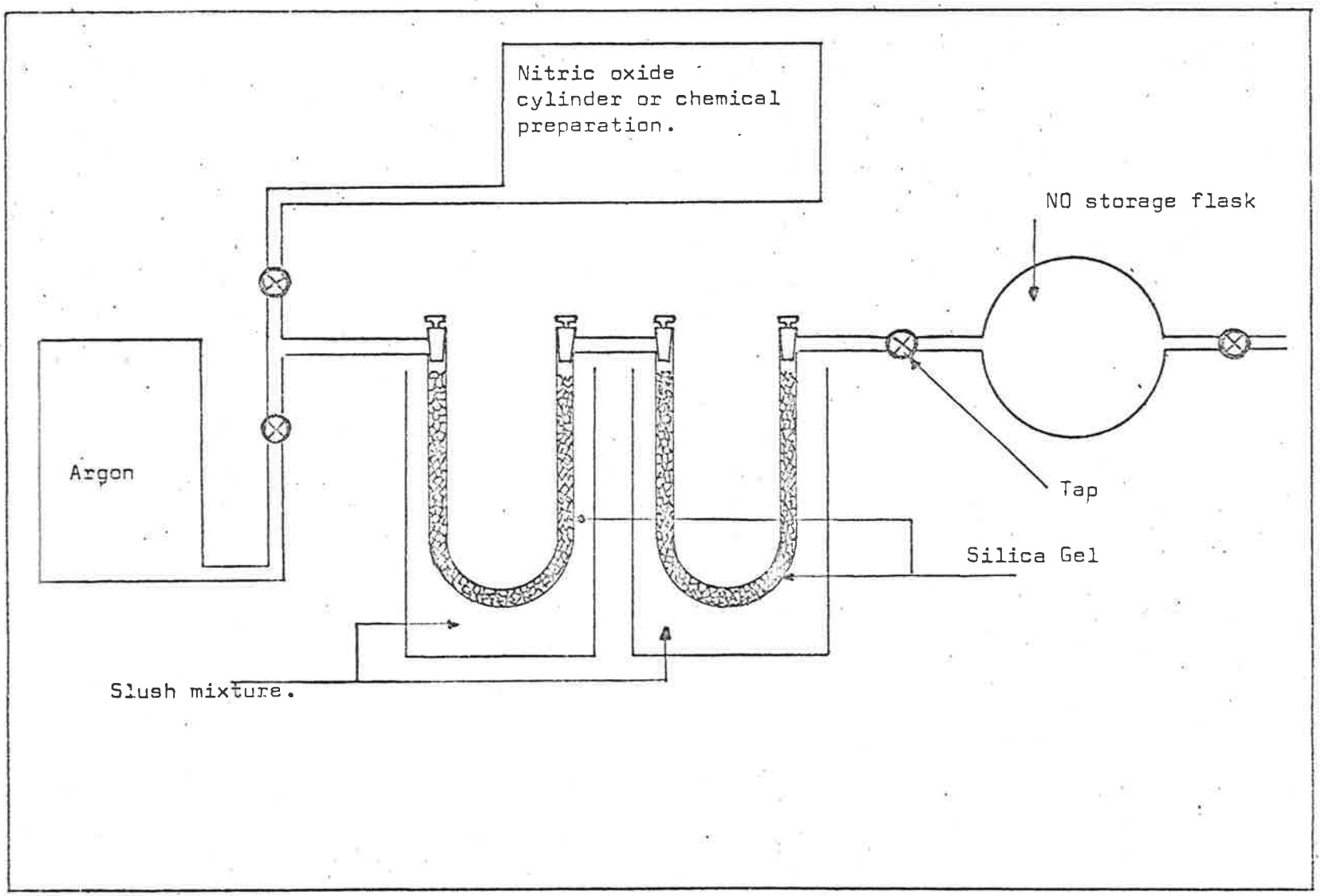

Fig. 3.3. Experimental arrangement for the purification of nitric oxide.

Fig. 3.4. A view of a completed ion chamber. The back of the ion chamber, on the right, has been protected by potting in silicone rubber. On the left is a partly completed ion chamber which shows the three electrodes as well as the resistor, included to protect the ion chambers' power supply.

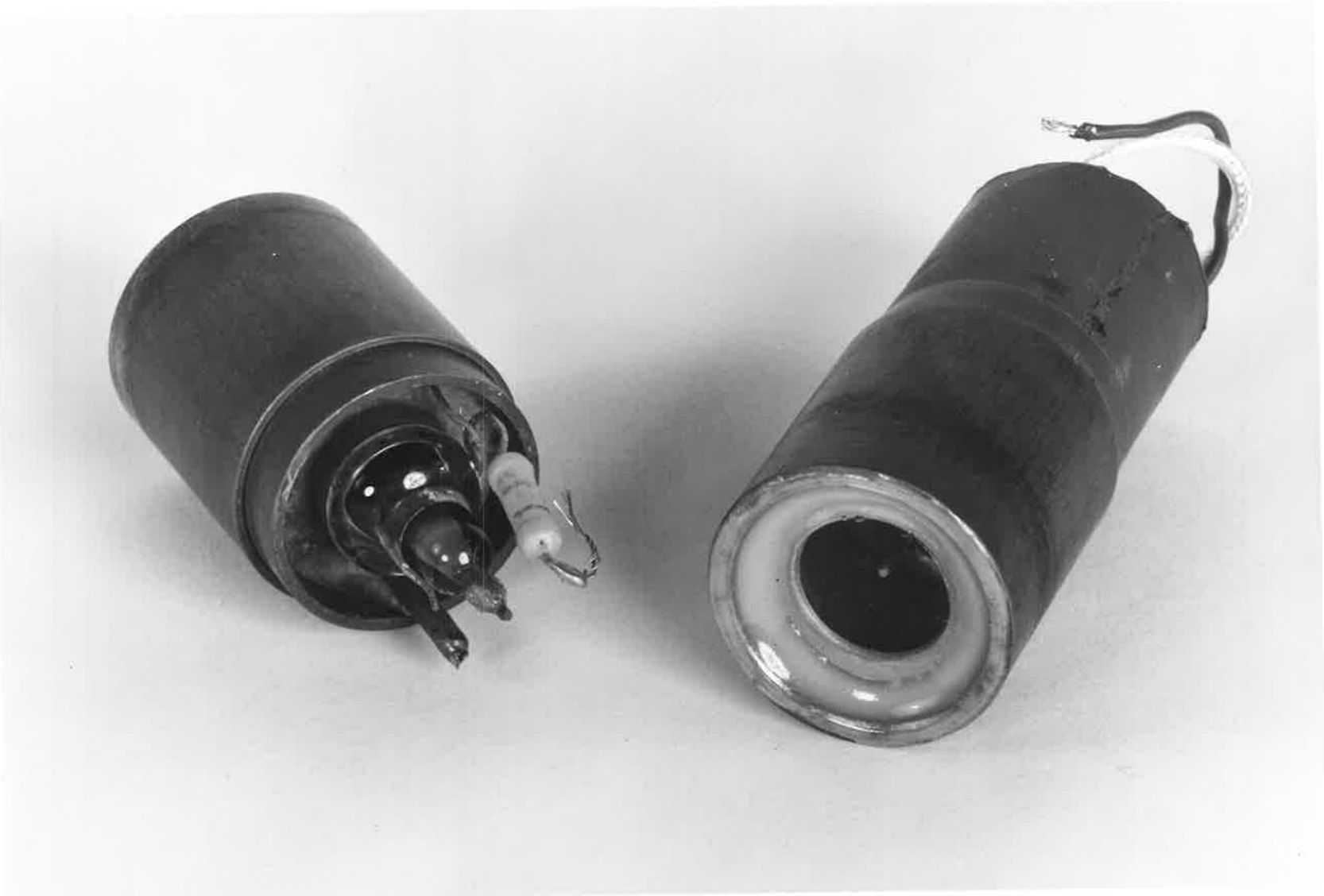

ion chamber. (see Section 3.3.1.).

Figure 3.4 shows two ion chambers. One ion chamber has a resistor added to the anode lead and shows the kovar-glass seal with the guard ring. The resistor was added as if there were a mechanical breakdown during a rocket flight and the ion chamber's electrodes were shorted, then the power supply to the ion chamber would not be overloaded. The second ion chamber in Figure 3.4 has the glass seal and the electrical wiring protected by potting the back of the ion chamber in silicone rubber. This was the final form in which the ion chambers were flown.

3.3.1. CALIBRATION AND TESTING OF ION CHAMBERS

A small portable D.C. hydrogen lamp was constructed for periodic testing of the ion chambers. The lamp consisted of an ion chamber body with a lithium fluoride window so that ultra-violet radiation of wavelength greater than 1050 Å was emitted. The pressure of hydrogen in the lamp was adjusted, such that Lyman-α was dominant in the ultra-violet spectrum, by monitoring with a lithium fluoride-nitric oxide ion chamber, the output from the direct current discharge. The pressure was varied until a maximum output was obtained from the ion chamber. It was found that adjusting the pressure in this way, gave the best results for testing ion chambers other than the lithium fluoride-nitric oxide chamber. If

the lithium fluoride-nitric oxide ion chamber was placed at 2 cm. from the lamp only Lyman-α could penetrate the air gap and activate the ion chamber. The other wavelengths in the range 1050 to 1350 Å would be absorbed in an air gap of 0.3 cm. so that all ion chambers were tested with the air gap between the lamp and the ion chamber flushed with "oxygen free nitrogen". This removed oxygen and water vapour from the gap so that very little absorption occurred and the ion chambers responded to the lamp.

Periodic semi-quantitative measurements of the ion chamber's sensitivity were made with the portable hydrogen lamp. As the absolute intensity of the lamp could not be relied upon to remain constant, a standard ion chamber had to be employed. This standard ion chamber was usually an old lithium fluoride-nitric oxide chamber whose response had been constant over the previous year. The standard ion chamber was placed in front of the lamp, and a current measurement taken (I_S). Then the ion chamber to be tested was placed in an identical position, and its current measured (I_C). The ratio I_C/I_S should be independent of the absolute intensity of the hydrogen lamp. This process was repeated regularly and by comparing the values of I_C/I_S any degradation of the ion chamber's sensitivity could be measured. It was found that the ion chambers gave a high response when first filled which settled down to a slightly lower value about a week later. Figure 3.5 shows the circuit used for testing ion chambers.

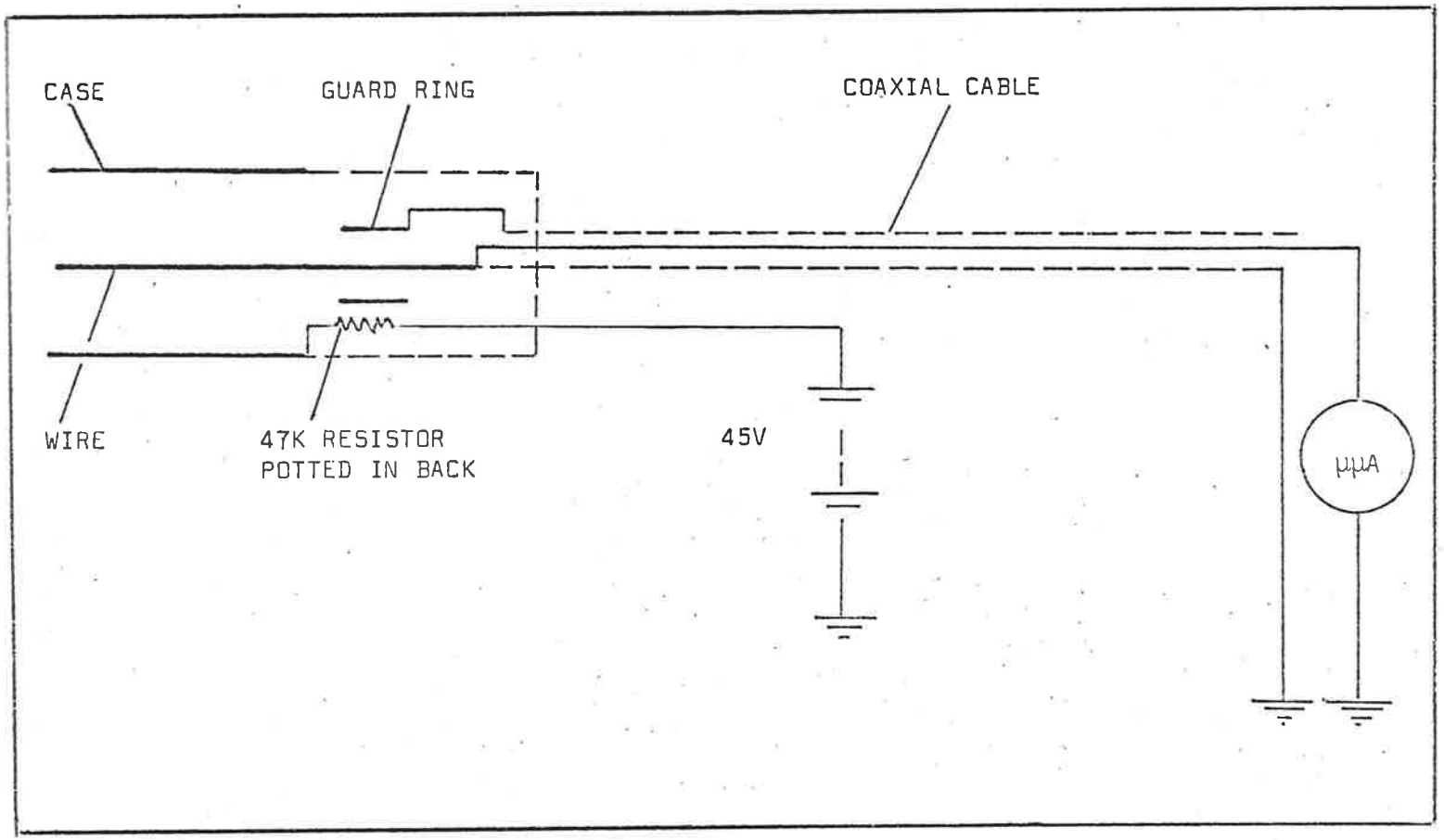

Fig. 3.5. The electrical circuit for testing ion chambers.

Apart from laboratory checks on the state of ion chambers, the portable hydrogen lamp was also used for final testing of the ion chambers at Woomera before launch.

3.3.2. SPECTRAL RESPONSE OF THE ION CHAMBERS

The sensitivities of the ion chambers used in the present work were measured in terms of the quantum efficiency. The quantum efficiency is defined as the number of electrons collected at the anode of the chamber per photon incident on the window. Quantum efficiencies of ion chambers are given by the product of (1) the transmission of the window, (2) the fraction of the radiation absorbed in the filling gas and (3) the photo-ionization efficiency of the filling gas. The photo-ionization efficiency is defined as:-

$$\frac{\text{The number of photoelectrons produced in the gas}}{\text{The number of photons absorbed in the gas.}}$$

The current collected varied with the collecting voltage but for the ion chambers used, there was a plateau region of slope 0.1% volt extending from 10V to 90V where the current was almost independent on voltage and the collection efficiency was close to 100%. (see Fig. 3.1). In the present work, the quantum efficiencies were measured with a collecting voltage of 45V at which there was no gas amplification. Determination of the quantum efficiency at a particular wavelength involved the measurement of the current from the ion chamber when it was exposed to a monochromatic beam, of known intensity (see Section 3.3.3).

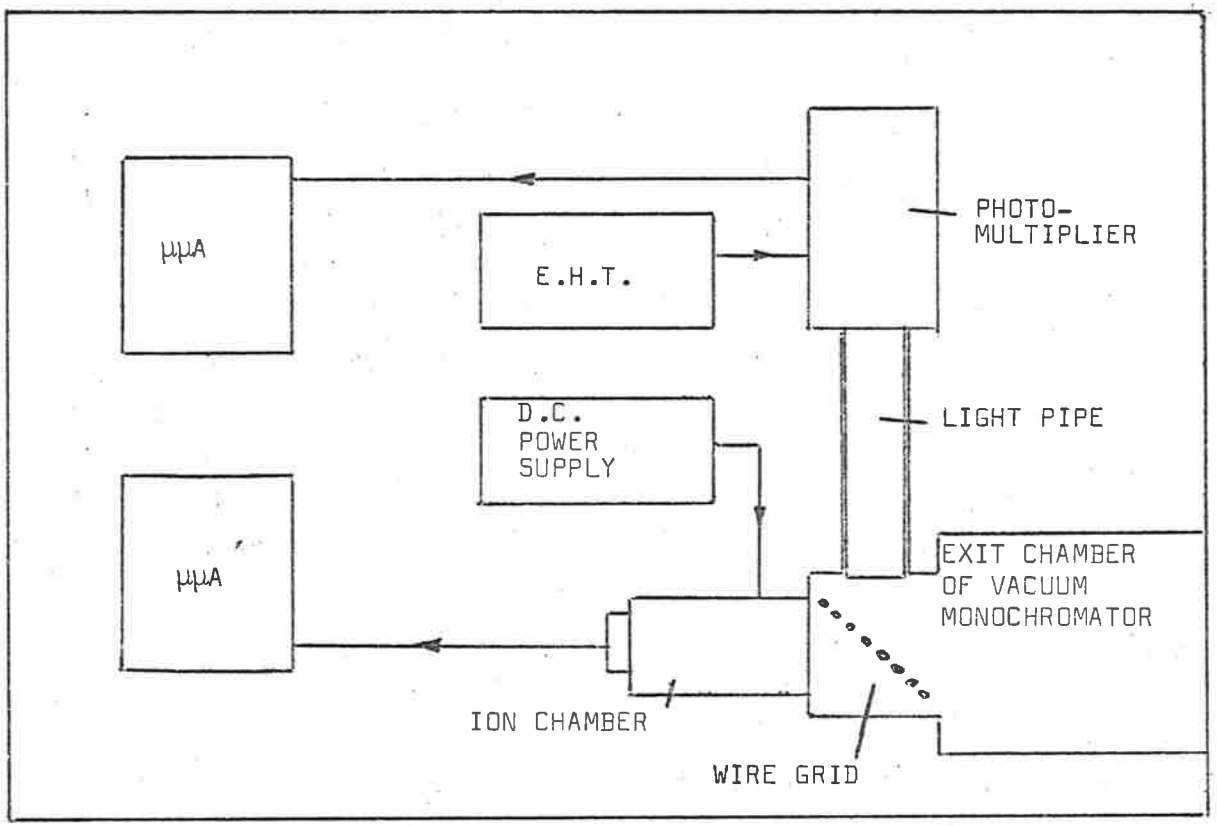

Fig. 3.6. The experimental arrangement for determining the spectral response of the ion chambers.

The spectral response of the ion chambers were measured by using a half metre McPherson vacuum ultra-violet monochromator: the light source was a hydrogen discharge, energized in a microwave resonant cavity. A sodium salicylate coated wire grid viewed by a photomultiplier (EMI 9514S) was placed,as shown in Figure 3.6,at the exit port of the monochromator and used to monitor the light beam (Ditchburn 1962). An ion chamber was placed as shown in Figure 3.6 but insulated from the monochromator's body so that the collecting voltage of 45V could be applied to the case.

Sodium salicylate sensitized photomultipliers have been used for many years as photon detectors in the near and vacuum ultraviolet spectral region. It was reported by several authors {Watanabe and Inn (1953), Smith (1960)}, that the phosphor possessed the desirable property of having a luminescent efficiency which was essentially independent of the wavelength of the incident radiation. However, Knapp and Smith (1964) reported that sodium salicylate tended to decline in sensitivity with time. Their experiments showed that the decline in the response of the phosphor was due to the combination of two effects:-

(1) a decrease at short wavelengths due to prolonged exposure to the atmosphere of the monochromator, and

(2) a general decline at all wavelengths due to exposure to a large number of energetic photons (greater than 7.7eV).

Certain precautions had to be made in dealing with sodium salicylate.

Fig. 3.7. The experimental arrangement used for determining the spectral response of the ion chambers. An ion chamber can be seen mounted on the exit port of the vacuum monochromator.


610B ELECTROMETER
McPherson

The main precautions were that the coating of sodium salicylate should be replaced at short intervals and the atmosphere of the monochromator be kept as clean as possible. The method of renewing the sodium salicylate on the grid was very simple. The old coating could be washed off as sodium salicylate dissolved easily in water and a saturated solution of sodium salicylate was made in methyl alcohol and this solution sprayed onto the grid, kept hot with a hair dryer. The methyl alcohol evaporated leaving the new sodium salicylate deposited on the grid.

As these precautions were taken then the sodium salicylate had an almost flat spectral response throughout the region of interest for the ion chambers so that the photomultiplier current was directly proportional to the lamp output. The ratio of the ion chamber current to photomultiplier current gave the spectral responses of the ion chambers which were independent of the lamp spectrum. The data points for the spectral response were taken at 5 Å intervals throughout the bandpass of the ion chamber with the monochromator slit width set at 60μ corresponding to a spectral bandwidth of 2 Å. Figure 3.7 shows a view of the apparatus used for determining spectral responses.

3.3.3. ABSOLUTE CALIBRATION OF ION CHAMBERS

Absolute calibration was obtained by means of a standard parallel plate ion chamber filled with a gas, the photo ionization

efficiency of which had been previously determined. The most convenient gas was nitric oxide as the photo ionization efficiency had been determined by Watanabe and Matsunaga (1961) for wavelengths between 1050 to 1350 Å. The photo ionization efficiency of nitric oxide at Lyman-α is 81%. The absolute quantum efficiencies of all ion chambers were determined by first calibrating one Li F - NO chamber at Lyman-α and then using this chamber as a secondary standard to calibrate the others.

Figures 3.8 and 3.9 show the experimental arrangement for using the standard parallel plate ion chamber. The exit beam from the monochromator passes through the monitor grid, coated with sodium salicylate, and then entered the standard ion chamber through a 1 cm. diameter lithium fluoride window. The window was fixed in an aluminium mounting electrically insulated from the ion chamber mounting plate. Radiation not absorbed in the ion chamber struck a coating of sodium salicylate on a glass plate at the end of the chamber. This radiation excited the phosphor and the fluorescent radiation was detected by a photomultiplier mounted behind the plate. The stainless steel plates protruded past the window at one end and touched the glass plate at the other. An electrical contact between the window mounting and the anode of the standard ion chamber ensured that a collecting field would be provided for ions produced near the window. A portable vacuum system was used to evacuate the chamber and the nitric oxide was admitted through a needle valve.

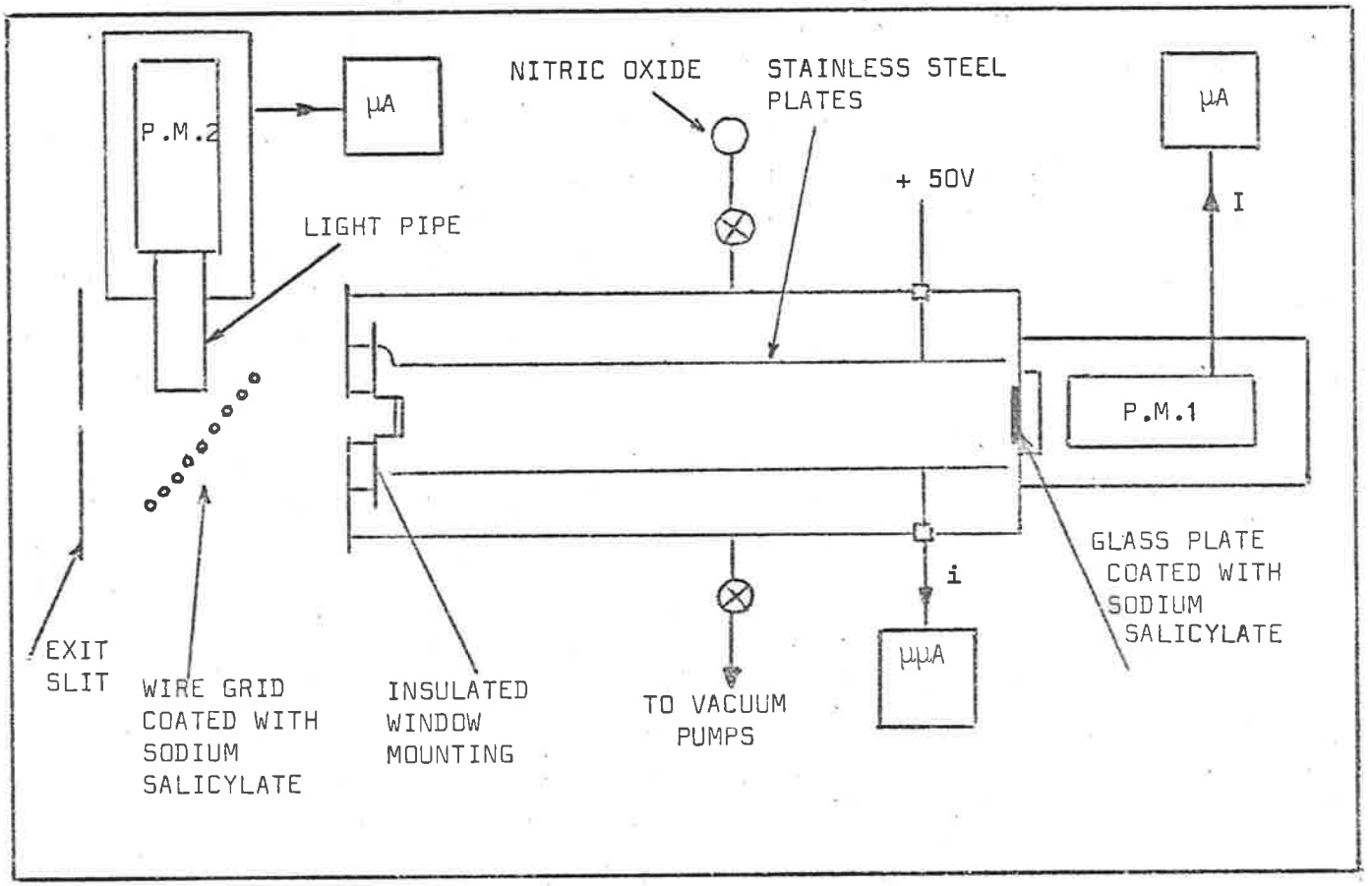

Fig. 3.8. The experimental arrangement for absolutely calibrating ion chambers.

Fig. 3.9. The experimental arrangement for determining the absolute calibration of the ion chambers. A portable vacuum system was used to evacuate the standard ion chamber and nitric oxide was admitted through the glass tube shown.

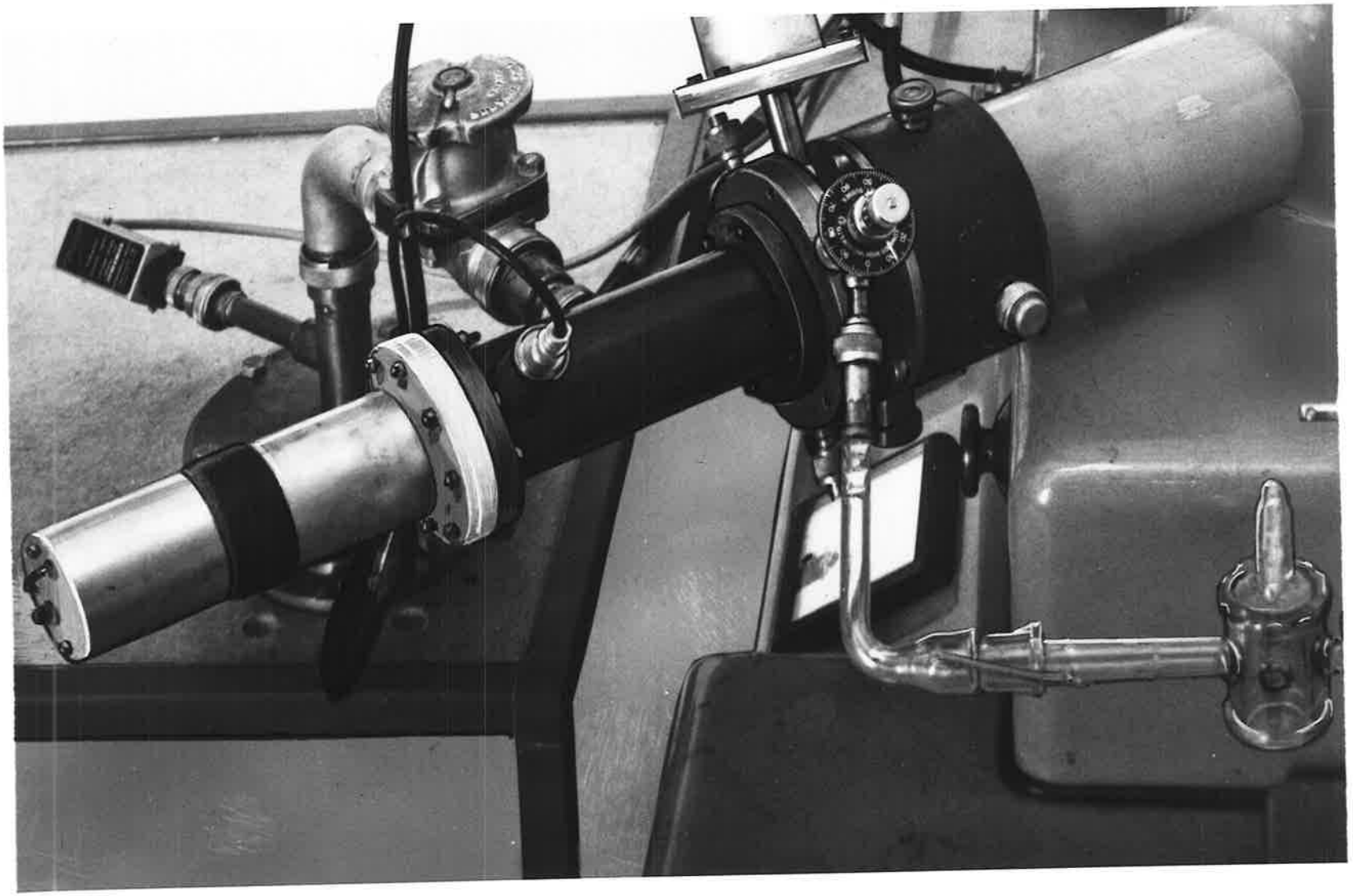

The procedure for determining an absolute calibration for a Li F - NO ion chamber was as follows:

Lyman-α radiation with a spectral bandwidth of 2 Å was transmitted from the monochromator to the standard ion chamber. The currents from the photomultipliers at the end of the chamber (P.M.1) and at the end of the light pipe (P.M.2) were first noted, and then nitric oxide was admitted to the chamber at a series of pressures in the range 0.1 to 10 torr. At each pressure the collecting voltage in the ion chamber was adjusted until a plateau was obtained, then the current I given by P.M.1 and the ion current (i) were noted. The current from the monitor photomultiplier (P.M.2) was used to correct I for any variation in beam intensity. The currents I and i were then plotted (see Figure 3.10). If all the ions were collected, the decrease in I when gas was admitted to the chamber would be proportional to the increase in i, and a straight line graph would result. As the pressure was increased, I decreased to a small value I_0 representing the scattered visible light in the monochromatic beam. A straight line was drawn through the experimental points, and from the line i_0, corresponding to I_0 was determined. The ion current which would be obtained if all the Lyman-α photons emerging from the window had been absorbed and the ions collected is represented by i_0. If all the Lyman-α photons had produced an ion the current would have been $i_0/0.81$. After the measurements with the parallel plate ion chamber had been completed it was removed, leaving the window in place, and replaced by a Li F - NO ion chamber. The space between the ion chamber

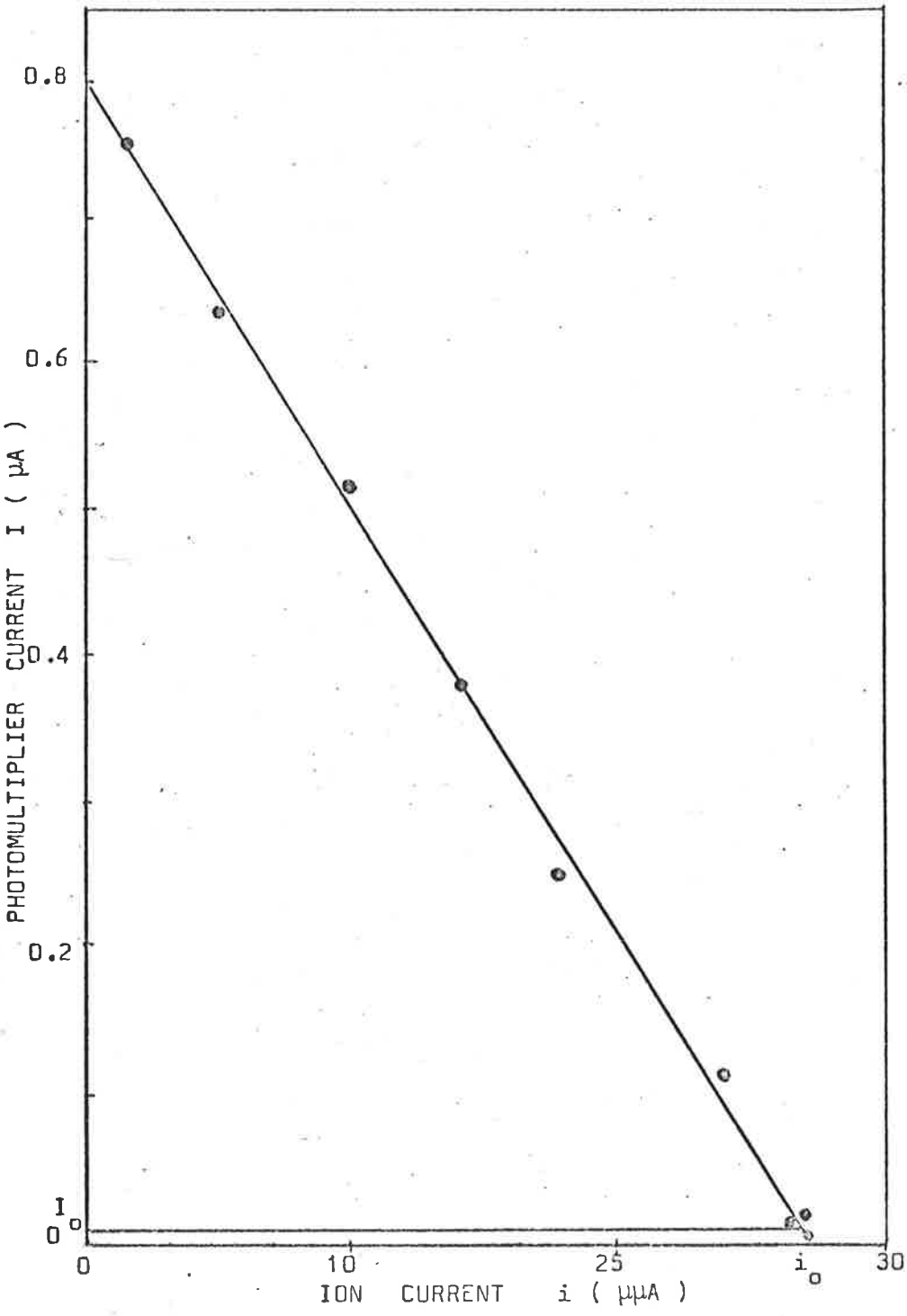

Fig. 3.10. The results from using the standard, parallel plate ion chamber.. The values for the parameters i_o and I_o can be easily obtained from this graph.

and the window was evacuated and the current i_L given by this chamber, operated at unit gain, was measured. The quantum efficiency at Lyman-α for this chamber was then given by:

$$Q_L = 0.81\ i_L/i_O$$

This one point for the quantum efficiency established a linear scale for the spectral responses of the ion chamber as determined in Section 3.3.2.

To determine the absolute quantum efficiency for any other chamber, the photomultiplier current (I_c) and the ion chamber current (i_c), were noted for wavelengths within the sensitive range of the chamber. The absolutely calibrated Li F - NO chamber was then placed in position and the corresponding currents at Lyman-α, I_L and i_L noted. The quantum efficiency for the ion chamber at the wavelength chosen for measuring i_c and I_c was given by:

$$Q_c = Q_L \frac{i_c}{I_c} / \frac{i_L}{I_L}$$

and hence a linear quantum efficiency scale was constructed.

Figures 3.11 and 3.12 show the variation of quantum efficiency with wavelength for the ion chambers used in the present work. Some of the fine detail on these curves has been lost as data points were taken at 5 Å intervals. The curve for the Li F - NO chamber follows very closely the photo-ionization efficiency of nitric oxide as given by Watanabe and Matsunaga (1961) and shows the effects of photo-ionization leading to the first and second vibrationally

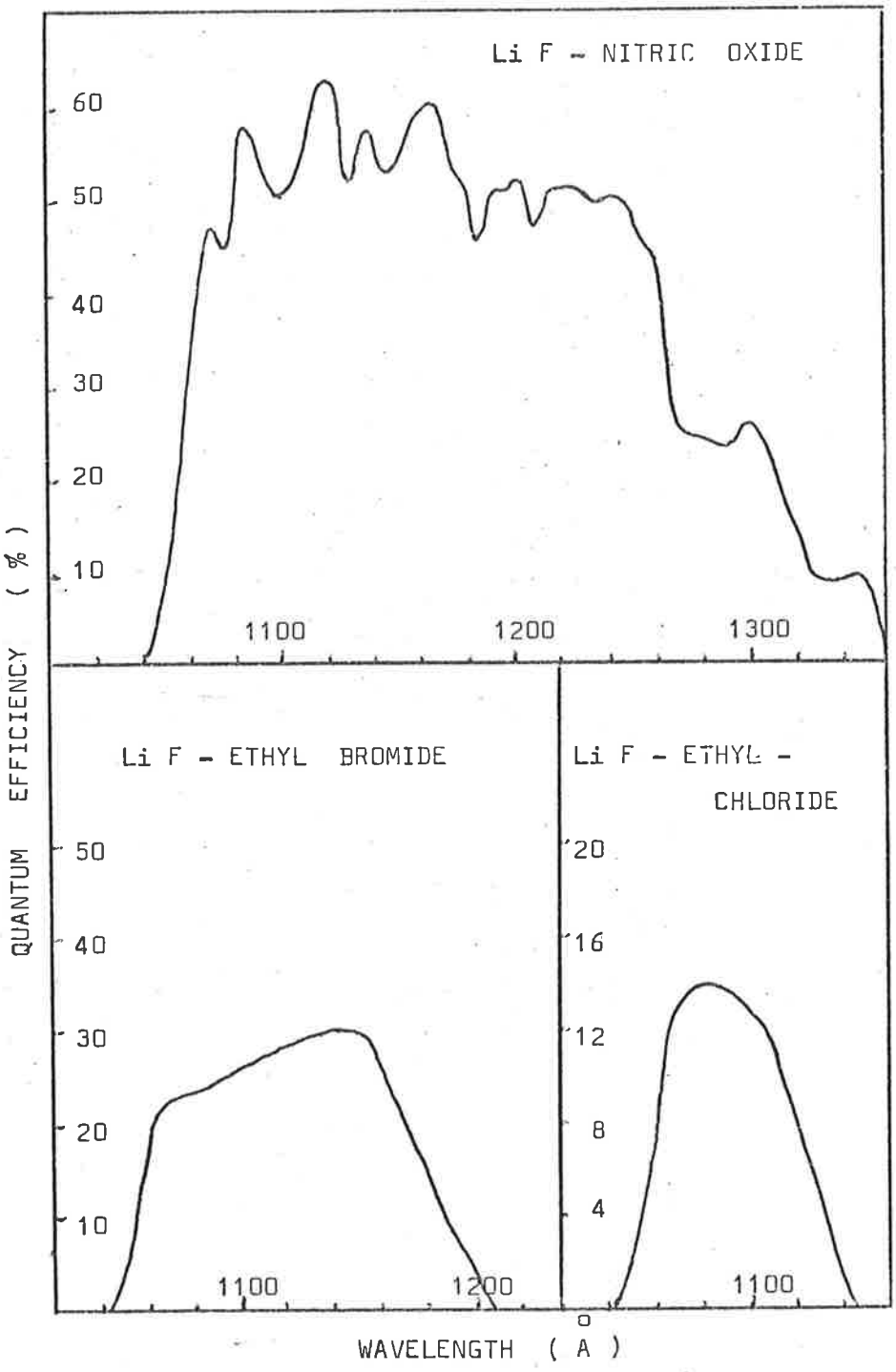

Fig. 3.11. Response curves of the Li F windowed ion chambers.

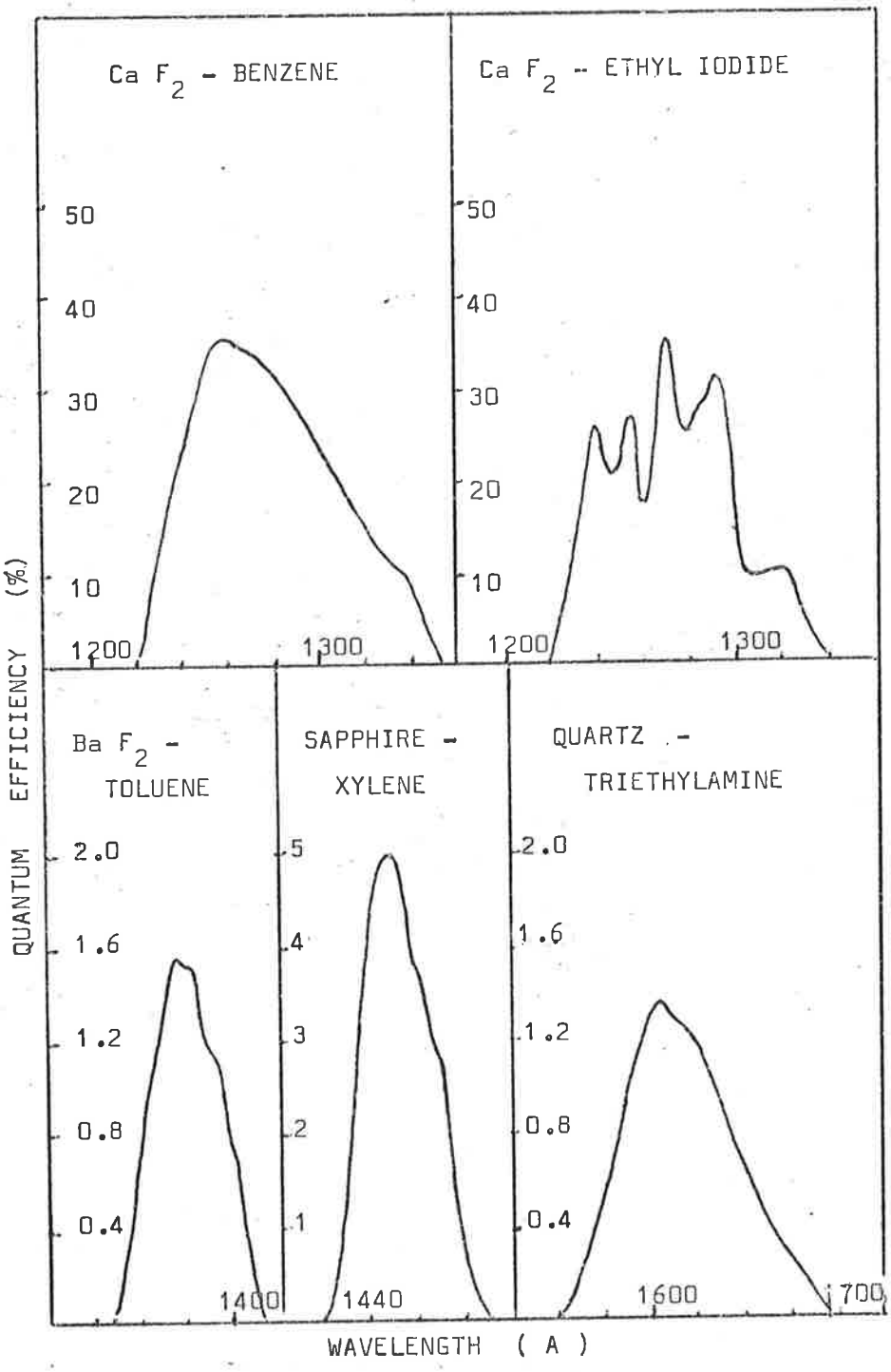

Fig. 3.12. Response curves for the ion chambers not included in Fig. 3.11.

excited levels of the nitric oxide ion, the thresholds of which lie at 1300 Å and 1260 Å respectively.

The complete method of calibration was checked by determining the spectral responses of ceramic sapphire-Xylene ion chambers which had been calibrated by an absolutely calibrated photomultiplier instead of a parallel plate ion chamber. These chambers were calibrated as part of a pre-flight check for Skylark 406, 407 and 408 (Wildman et al 1969). The two methods of calibration agreed to within 5% for the quantum efficiency at a wavelength of 1450 Å (Wildman, private communication).

The ion chambers, as well as being used for rocket experiments, were used as detectors in the laboratory for measuring ultraviolet flux. The ion chamber produced a signal current which was directly proportional to the flux incident upon it. The current, i, from the ion chamber was given by the following expression:

$$i = \phi.\lambda.Q.\ 1.01 \times 10^{-11} \text{ amps.}$$

for a monochromatic flux ϕ(erg $cm^{-2}sec^{-1}$) of wavelength λ(Å). The term Q, in the above equation, refers to the quantum efficiency of the ion chamber at the wavelength λ. The constant 1.01×10^{-11} applies only to the ion chambers used in the present work as it depends on the geometry of the chamber.

3.3.4. ANGULAR RESPONSE OF THE ION CHAMBERS

When analysing the data from a rocket flight, the ion chamber data has to be corrected for zero aspect.* The angular responses of the ion chambers were required for this purpose. Under favourable conditions these may be determined during the actual flight, making use of the roll of the rocket (see Section 4.3.3.), but as this cannot be relied upon, the angular responses of the chambers used were determined before flight.

The portable hydrogen discharge lamp was mounted in the side of a chamber and the ion chamber was mounted on the end of a rotatable shaft passing through the lid. The chamber was flushed with oxygen-free nitrogen whilst the ion chamber was rotated in front of the lamp. Angular responses taken in this way would not be exactly the same as that obtained during a rocket flight as the beam from the lamp was not strictly parallel. During the Long Tom rocket flight, the aspect angle was zero and a comparison of the response obtained in the laboratory with that obtained during flight could be made. The laboratory response was not in error by more than 5%. Figure 3.13 shows a typical angular response for all ion chambers as they have the same geometry.

---

*The aspect angle is defined as the angle between the direction of the sun and the normal to the ion chamber window.

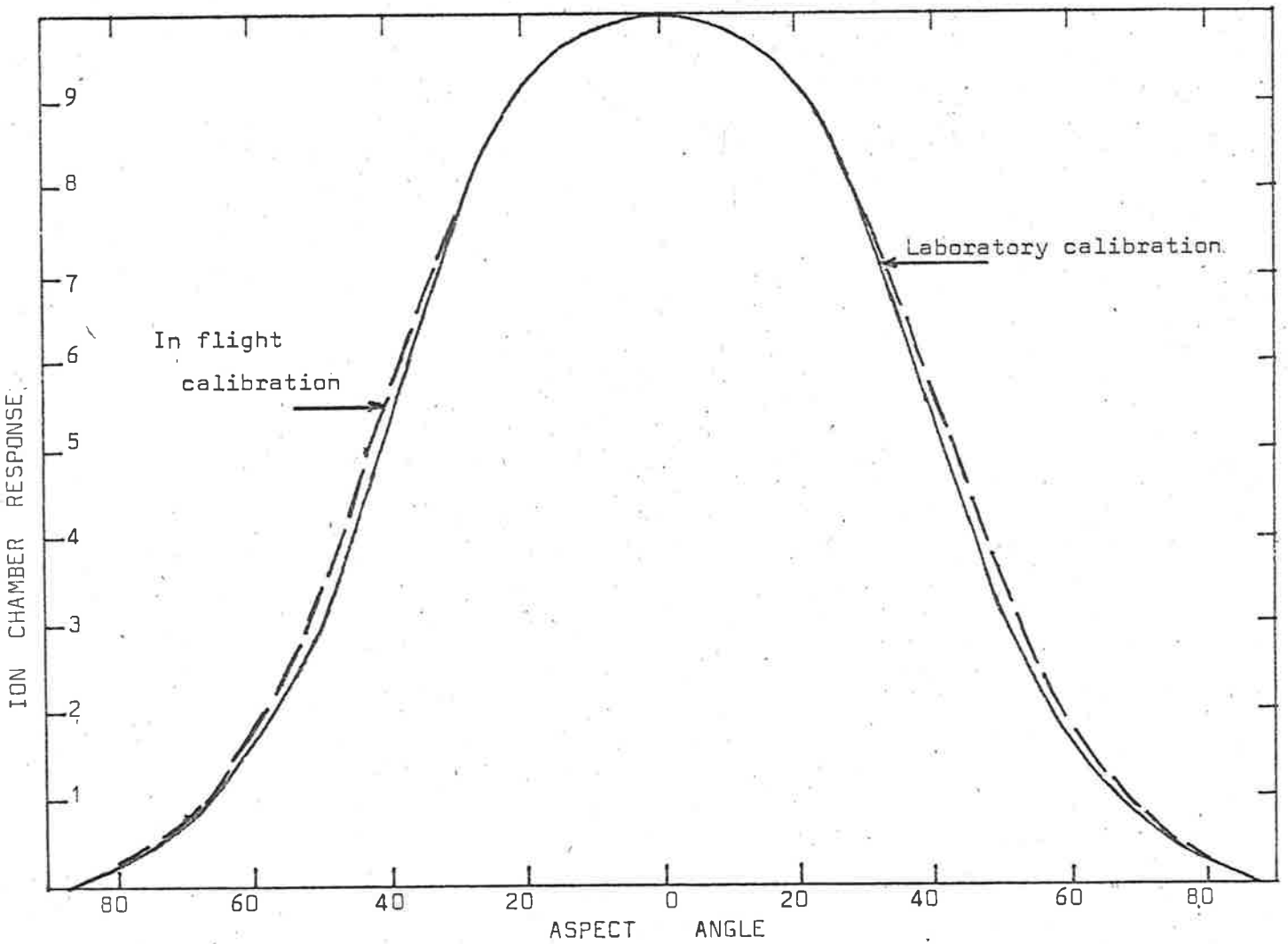

Fig. 3.13. Angular response of one of the ion chambers flown in Long Tom. Full curve: Laboratory calibration. Dashed curve: Inflight calibration. The response curves have been normalized at 0^{o}.

3.3.5. EFFECT OF TEMPERATURE ON THE ION CHAMBERS

As rockets are subject to considerable aerodynamic heating during flight, the effect of temperature on the ion chambers was investigated by Carver and Mitchell (1967). All ion chambers were investigated in the range 15°C to 100°C. The main effect of a temperature rise was a shift to longer wavelengths of both the short and long wavelength limits of the spectral range. Variations with temperature produced by variations in window transmission were much larger than the variations at the long wavelength limit. Knudson and Kupperian (1957), Laufer et al. (1965), Edmonds (1966) and Carver and Mitchell (1967) were all in agreement that the temperature variation of window materials were linear. Carver and Mitchell observed the rates of variation were 0.22, 0.23, 0.37, 0.21 and 0.16 $\mathring{A}\ deg^{-1}$ C for windows of lithium fluoride, calcium fluoride, barium fluoride, sapphire and quartz respectively, although they pointed out that there may be some variability in different batches of window materials.

The shift at long wavelengths which probably arises from thermal excitation of the gas molecules was also investigated by Carver and Mitchell. They observed a long wavelength shift of 0.02, 0.03, 0.02, 0.03, 0.03 $\mathring{A}\ deg^{-1}$C for nitric oxide, benzene, toluene, xylene and triethylamine respectively.

It can be seen from the above data the larger shift in the short wavelength limit can be particularly important in measurements

of the solar spectra using ion chambers if solar emission lines are near the window transmission limit.

3.3.6. ION CHAMBER LINEAR AMPLIFIER

The circuit for the amplifier used on the ion chamber is shown in Figure 3.14. The current from the ion chamber was passed through a resistor connected between the grid of a miniature electrometer valve and earth. A maximum input resistance of 1000 MΩ could be used with this valve and was used for chambers with small quantum efficiencies, i.e. Sapphire-Xylene and Quartz-Triethylamine ion chambers. Resistances of the order of 30 MΩ were required for the Li F - NO ion chambers. The input resistance had to be specially selected for each individual ion chamber flown, as the current from the ion chamber varied with the quantum efficiency. As the amplifier had a gain of four, and the maximum output required for the telemetry system was 1.5 V, the input resistor was adjusted to give an expected output of 1.0 V which required the ion chamber current to develop a voltage of 0.25 V across the input resistor.

Zero drift caused by temperature changes was compensated by a thermistor (M53) which was mounted on the same heat sink as the transistors (BCZ13), zener diode and the diode OA 202. During flight the observed zero drift was always less than 1% of full scale for a single ion chamber attached to the amplifier. In the Long Tom rocket

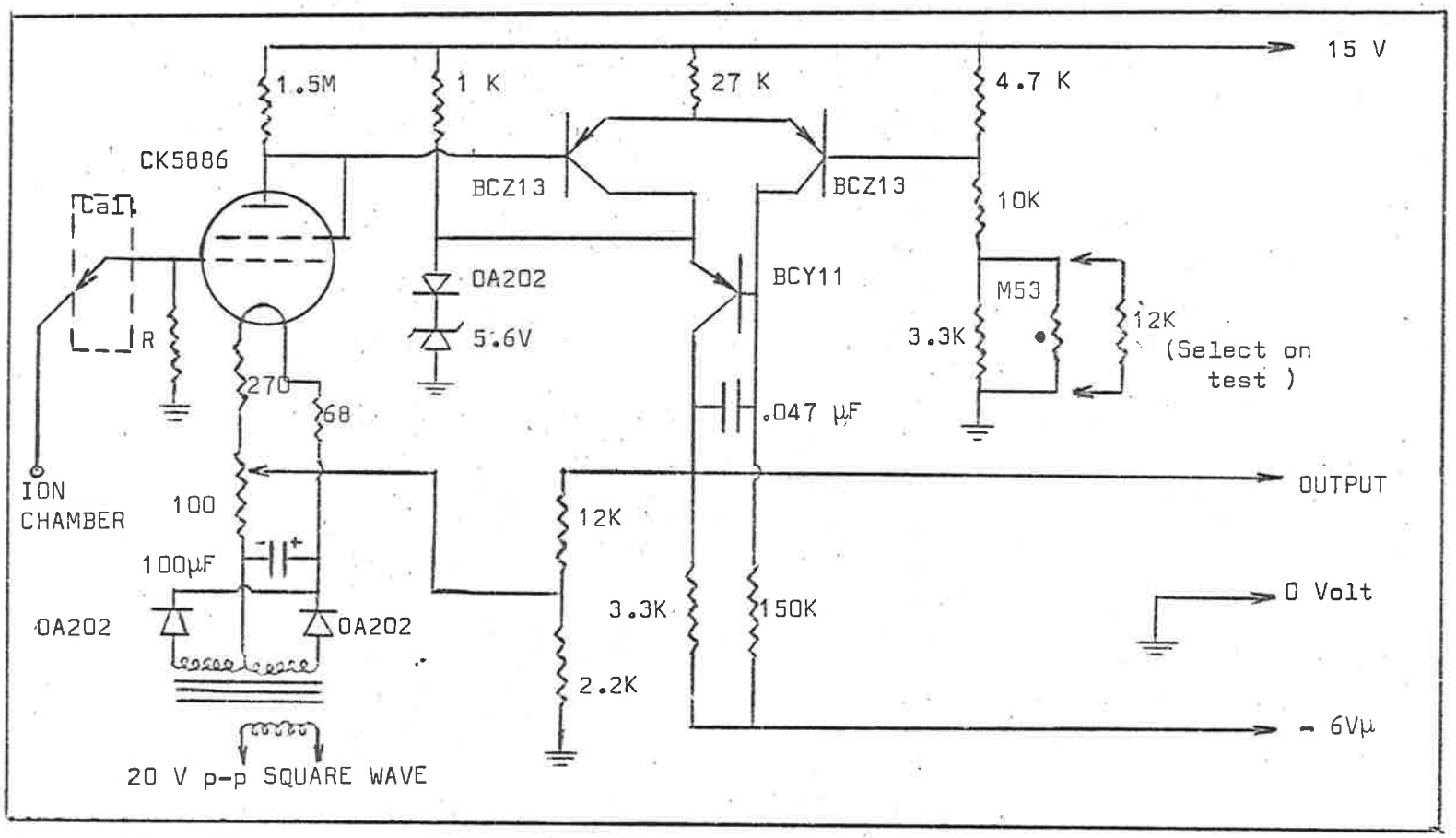

Fig. 3.14. Circuit for the ion chamber linear amplifier flown on Long Tom.

flight when two ion chambers were used on the one amplifier the zero drift was approximately double that for a single ion chamber.

A calibrator was included so that the amplifiers could be checked during flight. The ion chamber currents were disconnected by a relay every 20 seconds and two voltages of 0 and 0.35 V were applied to the inputs for 200 m sec. each. On the final telemetry record the distance between these levels corresponded to an input current of 0.35/R amps., where R was the input resistor of the particular amplifier.

3.3.7. GAS GAIN ION CHAMBERS

All of the ion chambers described can be operated at gas gain up to an amplification of 1000 before they become unstable. Figure 3.1 shows a typical gas gain characteristic for a Li F - NO ion chamber.

A special Li F - NO ion chamber was designed for use in WRESAT as the detector in a Lyman-α telescope. Figure 3.1 shows the cross-section of this chamber as well as the gas gain characteristic. The exterior geometry was identical to a normal ion chamber but the guard ring was extended inside the chamber to form the cathode. With the guard ring extended in this way a much greater electric field strength existed between the anode (central wire) and the cathode than in the normal ion chamber. This chamber had the same

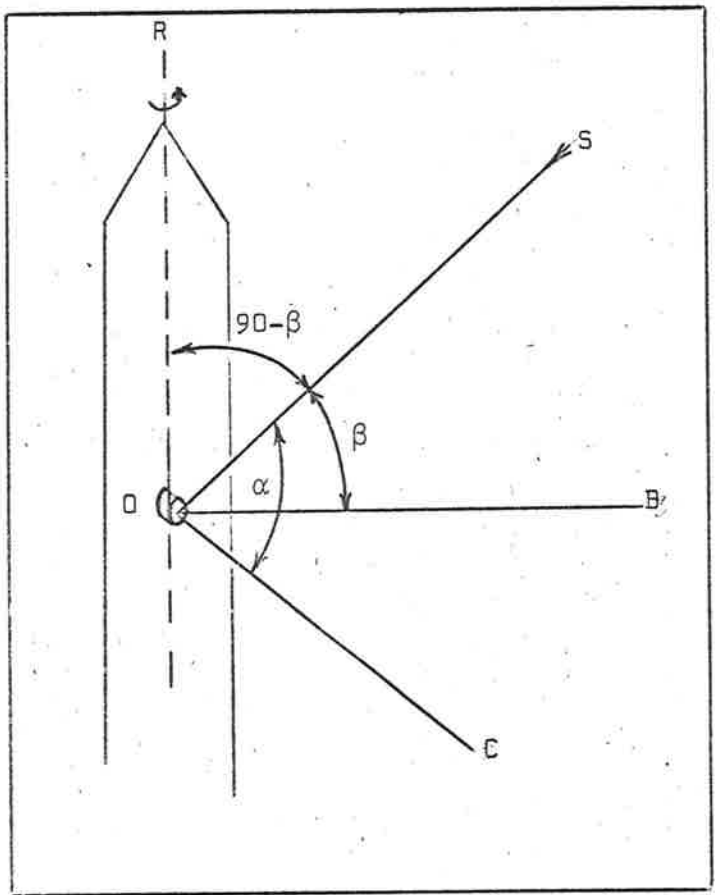

Fig. 3.15. Diagram illustrating the rocket aspect angle (β).

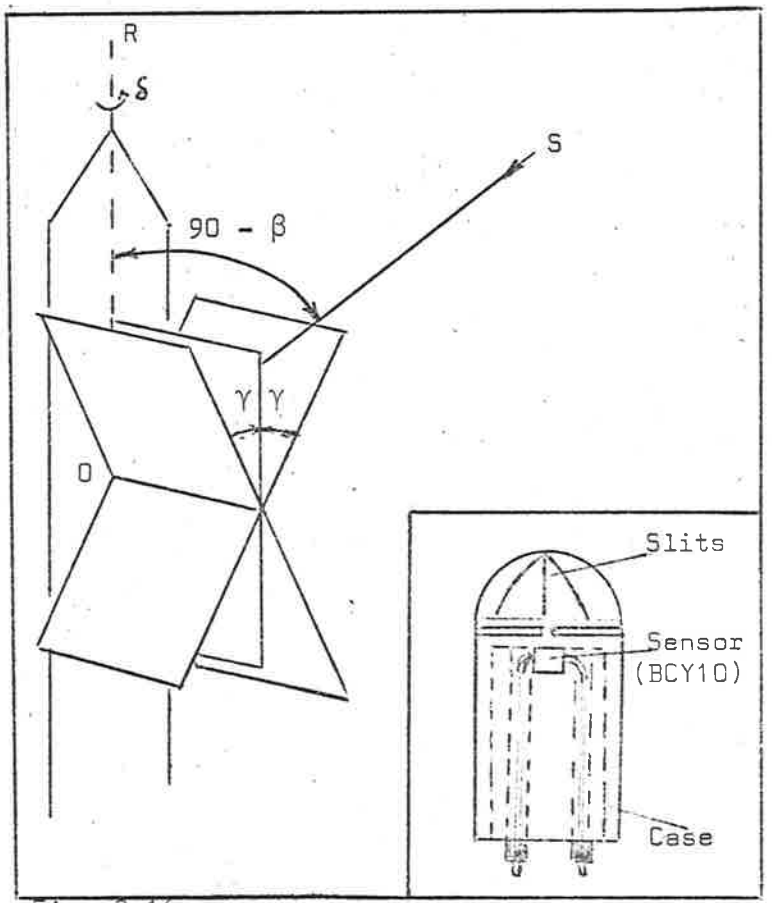

Fig. 3.16. Diagram illustrating the operation of the sunslits. The planes inclined at an angle γ are the planes of the slits cut in the sensor.

range of amplification as the normal ion chamber but achieved the gain at a much lower anode voltage. The gain used in WRESAT was 345 at an anode voltage of 565V. A quantum efficiency of 14% at Lyman-α was determined by the same method as for normal ion chambers.

As the gas gain ion chamber was used with the central wire positive there was no protection for long wavelength photoelectric response. The existance of a very weak photoelectric response was found by exposing the ion chamber to radiation from a high intensity monochromator. A long wavelength response peak centred at 2200 $\mathring{A}$ was measured. The maximum photoelectric current, with the ion chamber operating at a gain of 300, was 1.5×10^{-12} amps. No response could be detected for wavelengths between 1800 and 2000 $\mathring{A}$ or greater than 2300 $\mathring{A}$. Corrections for long wavelength response should be applied to any flight data from this chamber.

3.4.1 ASPECT ANGLE SENSORS

Since the response of the ion chamber varied with the angle between the direction in which the ion chamber was pointing and the direction of the incident light (aspect angle), it was essential to know the solar aspect angle during flight. The response of the ion chamber can then be corrected to what the current should have been if the chamber had been pointing directly at the sun. If the roll rate of the rocket is greater than the rate at

which the rocket axis changes its position due to precession, then the ion chamber will show one peak in its output for each roll. In Figure 3.15, OR is the rocket axis, OC the detector axis, OS the direction of the sun and OB is the detector axis when OC, OS and OX are all in the same plane. The angle α is the aspect angle for the detector and as the rocket rolls, α decreases until it reaches a minimum angle β when OC, and OB are coincident. At an angle β, the detector output would be a maximum and it was this angle that needed to be determined. Two types of detector were used to measure the aspect angle.

3.4.2. SUNSLITS

Sunslits were used for determining the aspect angle. They respond only when the sun crosses one of three planes fixed relative to the rocket body. Three slits 0.3 mm wide were cut in an aluminium hemisphere, one coinciding with the rocket axis and the other two making an angle of 45^{o} with it. All slits intersected along a line passing through the centre of the sensor. A small pinhole was placed in front of a photodiode which responded each time the passage of the sun crossed one of the slits. Figure 3.16 shows a schematic diagram of one of these sensors as well as a diagram illustrating the operation of the sunslits. On this diagram the angle γ represents the angle between the plane containing the slit parallel to the rocket axis and one of the other slits and δ represents the angle through

which the rocket has rolled whilst OS passes through γ. From the geometry,

$$\text{Tan } \beta = \text{Sin } \delta \text{ Cot } \gamma = \text{Sin } \delta \cdot 1,$$

so that by measuring the time between the pulses produced on the telemetry record as the sun crossed the slits and knowing the roll rate of the rocket, the aspect angle, β, can be determined. Three distinct pulses on the final telemetry record are visible only within the range $\beta = \pm 50^{\circ}$. Outside this range no response can be obtained through the two 45° slits. In flight, if only one pulse is recorded, then either the aspect angle occurred outside the range or was zero. The responses from other detectors flown can show which of these possibilities is correct.

The sunslits, as they relied on time modulation, gave results which were independent of the intensity of the solar visible and near infra-red radiation. However, the size of the pulses depend on the intensity of this radiation which is absorbed by ozone and water vapour and attenuated by Rayleigh scattering mainly below 70 Km. The main disadvantages with the sunslits occur if the roll rate of the rocket is too slow or irregular. With the telemetry system used, when the roll rate was too fast the sunslits were also unsuitable. The telemetry system sampled 80 times per sec., and with a roll rate of 2 cps leads to an error of $\pm 4.5^{\circ}$ in determining the position of the pulses, which would lead to a considerable error in aspect angle. Sunslits were not used in the WRESAT satellite as

the sampling rate in the telemetry system was not sufficient. As the use of sunslits was limited, they were flown in conjunction with the other form of aspect sensor described in Section 3.4.3.

3.4.3 ASPECT SENSOR USING AMPLITUDE MODULATION

The other method of determining aspect angle was by using the sensors designed by Mitchell (1966). Figure 3.17 is a cross-sectional diagram of this type of detector consisting of two silicon phototransistors (type LS 400) surrounded by a teflon insert. Teflon was used to diffuse the radiation falling on the detector, as the phototransistor peaked strongly in the forward direction. The teflon in front of one of the phototransistors protruded past the aluminium case and in front of the other was flush with the case. The effect of the protruding and flush teflon was to modify the angular response of the phototransistor so that each had a different response. (See Figure 3.18).

As the sun crossed the detector an output from each photo-transistor, which peaked once per roll was telemetered. The aspect sensors were mounted in the rocket so that they looked in the same direction as the ion chambers. Maximum output from the aspect sensors occurred at the same time as the maximum output from the ion chambers. The ratio of the outputs from the flush and protruding sensors at the peak response were independent of the intensity of the sun. By using

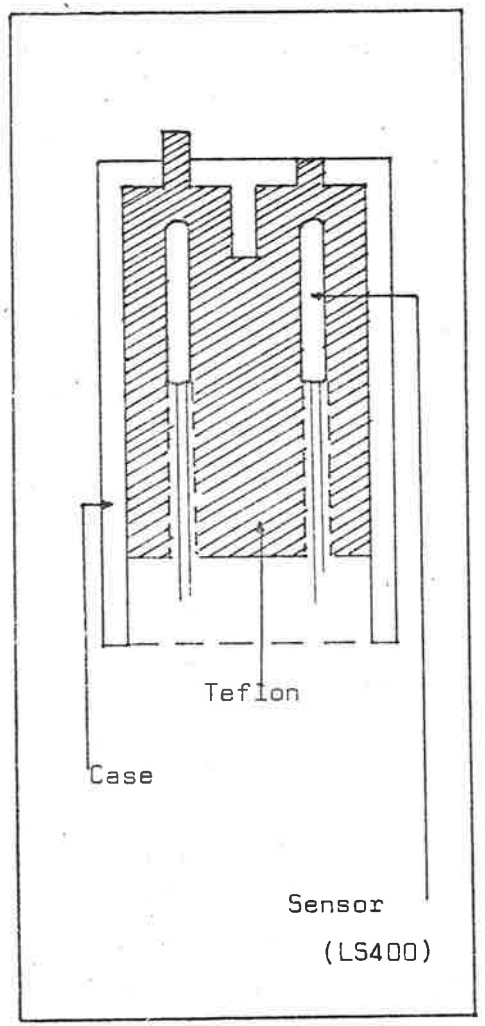

Fig. 3.17. A cross sectional diagram of the aspect sensors used in the Long Tom rocket and WRESAT

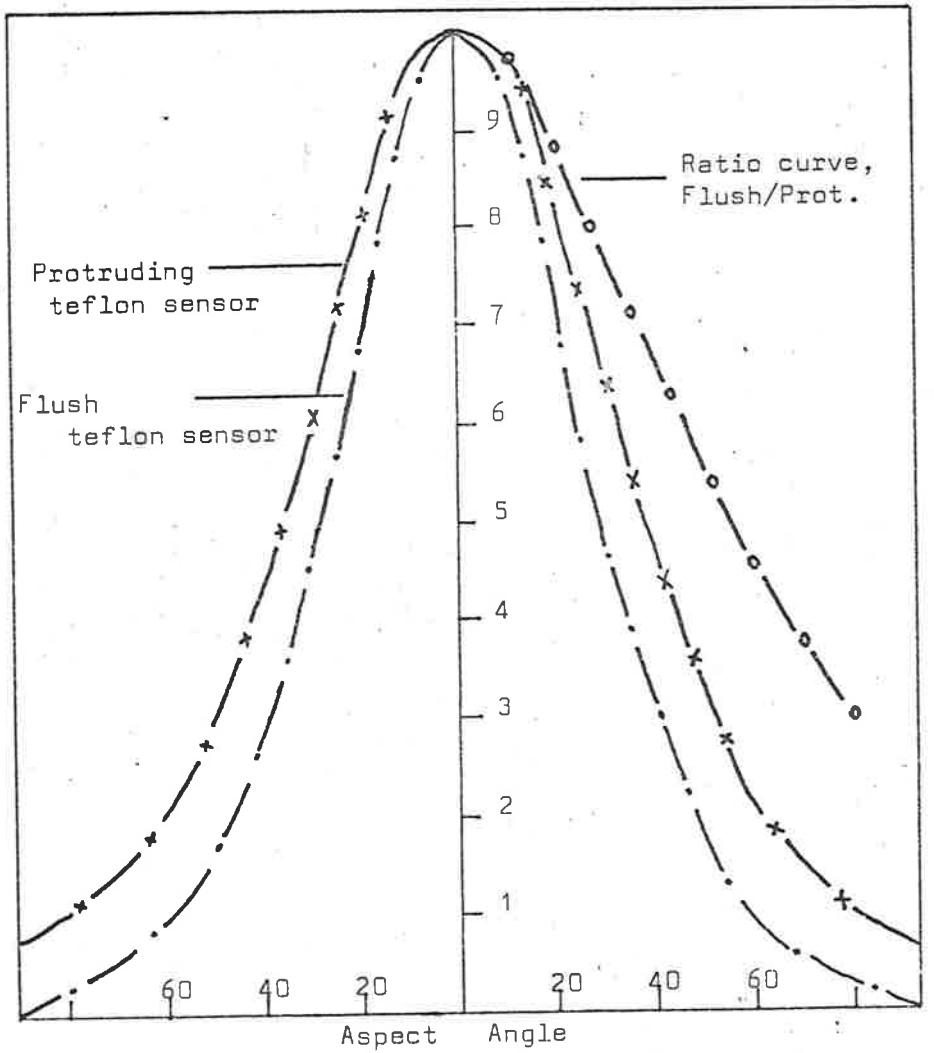

Fig. 3. 18. Laboratory angular response curves for a pair of aspect sensors. Also shown is the ratio curve for the two responses. All curves are normalized at 0^{o}.

laboratory calibrations of this ratio plotted against aspect angle, the aspect angle could be determined even in regions where considerable atmospheric attenuation of the solar visible radiation existed.

The laboratory calibrations were obtained by rotating the aspect sensors in front of a tungsten lamp. In the lamp housing a small hole was drilled and the distance between this hole and the sensor was adjusted so that the hole subtended an angle at the sensor equal to the angular diameter of the sun ($\approx 0.5^{o}$). Typical results of this calibration procedure are shown in Figure 3.18. Exposing the sensors in front of a tungsten lamp did not adjust the overall output level of the individual phototransistors. This was done, qualitatively, by exposing the sensors directly into the sun before launch at Woomera and adjusting each output level to approximately one third of full scale. The ratio of the two levels were noted and the laboratory ratio calibration normalized accordingly. By choosing one third of full scale meant that once the detectors reached an altitude above 70 Km. their outputs would not exceed 1.5 V (the limit of the telemetry system).

The laboratory calibrations would not be necessary if the detectors looked directly at the sun at some stage during the rocket flight above 70 Km. Above this height the intensity of the visible radiation from the sun can be assumed to be constant and as the sensors would be calibrated in flight the ratio of the detectors would not

have to be evaluated. The sunslits were useful for determining when this situation occurred in the Long Tom rocket flight. The sensitivities of the phototransistor were chosen so that both had identical temperature characteristics and the flush teflon detector had a sharp angular response. The flush teflon detector was used to determine aspect in the Long Tom rocket flight so that a sharp angular response was an advantage for accurate aspect angle determination.

The advantages of the amplitude modulation aspect sensor over the sunslits were that the aspect sensors were more accurate for large aspect angles and gave results as long as the telemetry system sampling rate was sufficient to define the curved shape of the output. However, as can be seen from the ratio curve drawn in Figure 3.18, the ratio does not change appreciably for angles < 20^{o} which leads to considerable errors in determining small aspect angles, whereas the sunslits are accurate in this region. This was not critical when determining aspect correction factors for ion chambers, as the ion chamber's angular response was also almost flat for small aspect angles, but it was critical for detectors with small fields of view like the Lyman-α telescope used in WRESAT.

Another disadvantage with the aspect sensor was that it responded to near infra-red radiation as well as visible. In a rocket flight, when the detector looks towards the earth it is possible for an appreciable infra-red signal to be recorded which has

to be allowed for in calculating aspect. In the Long Tom rocket flight this signal was negligible (<2%) in comparison with the visible signal, and aspect determinations were not corrected for this effect.

As can be seen from the above discussion it is advisable to fly both sunslits and aspect sensors so that as well as being complementary to one another, one can be used as a back-up system if the other fails.

CHAPTER 4. RESULTS FROM ROCKET EXPERIMENTS TO MEASURE Lα RADIATION

4.1.1 INTRODUCTION

Three HAD rockets were fired during the day carrying instrumentation to measure the intensity of solar Lα radiation and to determine molecular oxygen densities in the region 70 to 90 Km. Another HAD, instrumented with a Lyman-α telescope was fired at night to determine the amount of Lyman-α radiation reflected from the moon, scattered Lyman-α from geocoronal hydrogen and if possible, the nocturnal density of molecular oxygen.

A Long Tom rocket was successfully fired carrying a total of thirteen ion chambers to determine, in detail, molecular oxygen density between 70 and 120 Km., and to provide absolute determinations of the solar ultra-violet flux for several wavelength bands within the range 1050 to 1670 Å. The time of this flight was chosen to coincide with a pass over Australia by the Explorer 30 satellite so that comparison could be made between the solar flux obtained from ion chambers in Explorer 30 and that of Long Tom.

The WRESAT satellite was also put into orbit carrying a selection of ion chambers to complement and extend previous work done by Australia and the U.S.A. in rockets and also by the U.S.A. in satellites. One of the HAD day rockets (HAD 307) was fired as

WRESAT passed over Woomera so that a comparison could be made of Lyman α flux measurements.

4.2.1. HAD EXPERIMENTS

The HAD rocket, a two stage, solid fuel, five inch round had an apogee of approximately 90 Km. and was used to measure the absorption of solar Lyman α radiation. This meant that the rocket spent a major portion of its flight in the region 70 - 90 Km.; the height range where Lyman α is absorbed. Only the Li F - NO ion chamber can be flown as the other ion chambers do not start to respond until approximately 90 Km. All day HAD rockets had a complement of two Li F - NO ion chambers and their associated electronics, two sets of aspect sensors, sunslits and a photodiode interference filter combination for determining ozone concentrations.

Unfortunately, all the HAD rockets apart from HAD307 failed to reach 70 Km. and hence did not give any results for Lyman α flux or molecular oxygen density.

4.2.2. HAD 307

HAD 307 was fired from Woomera on 30th November, 1967 in conjunction with a WRESAT satellite pass over Woomera. It s purpose was to obtain Lyman α flux and oxygen densities to compare with that of WRESAT. Although it reached an apogee of 104 Km. it

precessed badly and at no time was the aspect angle less than 45^{o} which gave very grave errors to any flux and density information. The Lyman-α flux measured was 3.8 ± 1.8 erg/sec/cm^2 and the average molecular oxygen density, between 80 and 90 Km., was 2.10^{14} molecules/cm^3.

4.3.1 LONG TOM EXPERIMENT

The rocket LONG TOM 18, a two stage, solid fuel, nine inch round was fired from Woomera (Lat 30^{o} 35' S, Long. 136^{o} 31" E) on the 11th November 1966 at 08.35 hr. local time when the solar zenith angle was 48^{o}. The time corresponded to an Explorer 30 pass over the satellite receiving station at ~~Caravron~~ Carnarvon W.A. (Lat. 24^{o} S Long. 107^{o} E).

The rocket reached a maximum altitude of 121.2 Km. 172.27 seconds after launch and satisfactory telemetry signals were received throughout the flight. Tracking by FPS16 radar was incomplete as the rocket was only tracked on the upwards portion of its trajectory from 30 sec. after launch to approximately 130 sec. The method used to interpolate the heights of the missing part is described in Section (4.3.2.). Above 70 Km. the solar ultra-violet radiation was observed each time the rocket, which was rolling with a period of 4 sec., pointed the detectors in the direction of the sun. For the Li F - NO ion chamber a total of 57 scans were made. The roll period of 4 sec. was ideal for

this experiment as too long a period produces insufficient scans of the sun for accurate oxygen densities to be deduced. A short roll period introduces significant errors in the aspect angle results from sunslits as the telemetry system samples 80 times per second. This sample rate at a 4 sec. roll period corresponds to 1^{o} in roll.

The rocket carried aspect sensors described previously (Chap. 3) as well as the detectors listed in the Table (4.1) below.

TABLE 4.1

Detector (ion chamber)	Spectral Response	Effective Absorption Cross Section
Li F - nitric oxide (2)*	1050-1340Å	1×10^{-20} (Lα)
Li F - ethyl bromide (1)	1050-1200Å	highly variable
Li F - ethyl chloride (1)	1050-1130Å	
CaF_2 - ethyl iodide (1)	1220-1320Å	1×10^{-18}
CaF_2 - benzene (2)	1220-1340Å	1×10^{-18}
BaF_2 - toluene (2)	1350-1410Å	1.4×10^{-17} cm^2
Sapphire - Xylene (2)	1420-1470Å	1.5×10^{-17}
Quartz-Triethylamine (2)	1570-1680Å	3.0×10^{-18}
Geiger counter		
Phillips 18504 (2)	8Å	All constituents 5×10^{-20}

*The figure in brackets indicates the number of detectors of each type carried in the rocket.

The construction and properties of the ultra violet ion chambers has been described previously (Chap. 3). The effective absorption cross sections were determined by combining the measured spectral response of each detector with the molecular oxygen absorptions cross sections (Watanabe, 1958 ; Blake et al., 1966) together with Tousey's (1963) solar spectrum data. This is a simple procedure when the absorption cross section varies only slowly over the response range of the detector (Figure 2.2) as is so for the BaF_2 - toluene, Sapphire - Xylene and the Quartz - Triethylamine ion chambers. In the case of the Li F - nitric oxide ion chamber, the Lyman-α line so dominates the solar spectrum in the wavelength region to which the detector is sensitive that, at least for altitudes below 90 Km., the effective cross section is that at the Lyman-α wavelength. The effective molecular oxygen absorption cross sections listed in Table 4.1 for other ion chambers corresponded approximately to unit optical depth in the atmosphere, i.e. to a height range over which the ion chamber current is expected to be changing most rapidly with height. For the Li F - ethyl chloride and the Li F - ethyl bromide ion chambers, the absorption cross section varies so strongly over the bandpass that it is not possible to define an effective absorption cross section even for the limited height range near unit optical depth. The data from these two ion

chambers was therefore used for solar flux measurements only and not for the determination of atmospheric densities. The ion chambers were mounted in the rocket as in Fig. 4.1 and Fig. 4.2 which show the layout of the rocket experiment and the completed nose section.

The telemetry system was assembled from standard components. The outputs from the ion chambers were taken to a 24 channel rotating switch which sampled each channel 80 times per second. From the switch the signals went to a frequency modulator which was used to modulate the 465 MH_z signal from the main oscillator. As there was such a large number of detectors in the round and only 24 main channels not every detector could have a channel. Sub-commutated channels were used for maintaining voltages and thermistors. Rather than sub-commutate the detector signals, three things were satisfactorily attempted. First the aspect sensors in bank B (X-ray Bank) and bank C were sampled i.e. the flush and the protruding aspect sensor were switched such that only one channel was used for both detectors. Second, the calcium fluoride-ethyl iodide ion chamber and the calcium fluoride-benzene chamber shared the same amplifier. As these chambers were in Bank A and Bank C the roll of the rocket automatically gave the full signal for one chamber and then the other. The barium-fluoride-toluene chambers also shared one amplifier.

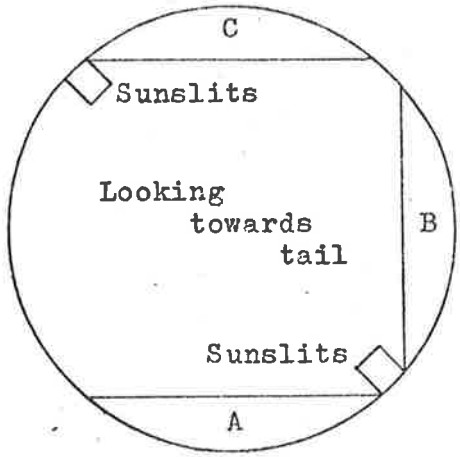

A Bank		B Bank		C Bank	
Posn. No.	Chamber	Geiger Counters		Posn. No.	Chamber
1	Li F-Ethyl chloride			1	Li F-Ethyl Bromide
2	Li F-NO			2	Li F-NO
*3	CaF_2-Ethyl iodide	← shared amplifiers →		3	CaF_2-Benzene
4	BaF_2-Toluene			4	BaF_2-Toluene
*5	Sapphire-Xylene			5	Sapphire-Xylene
6	Quartz-Triethylamine			6	Quartz-Triethylamine

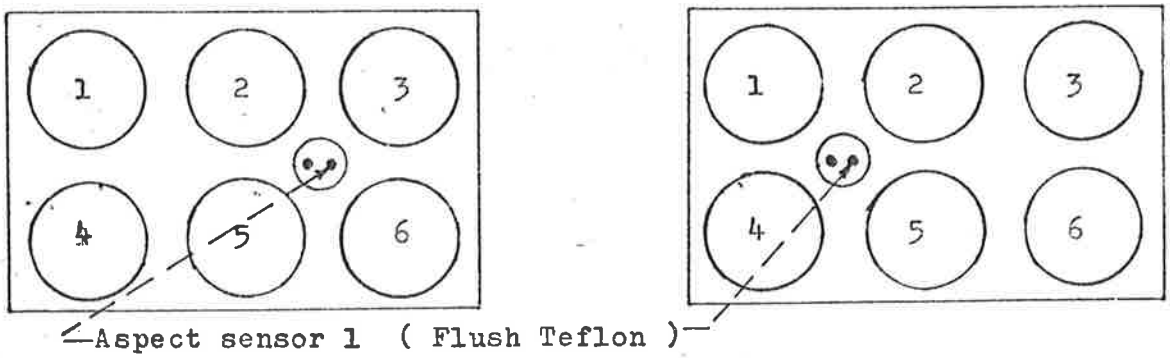

*Thermistors were mounted on these chambers.

Fig. 4.1. Layout of the ion chamber experiment in the Long Tom rocket flight.

Fig. 4.2. The completed Long Tom rocket head showing one bank of ion chambers as well as one ion chamber outside the cover band. To the left of the experiment block is the cover band release mechanism.

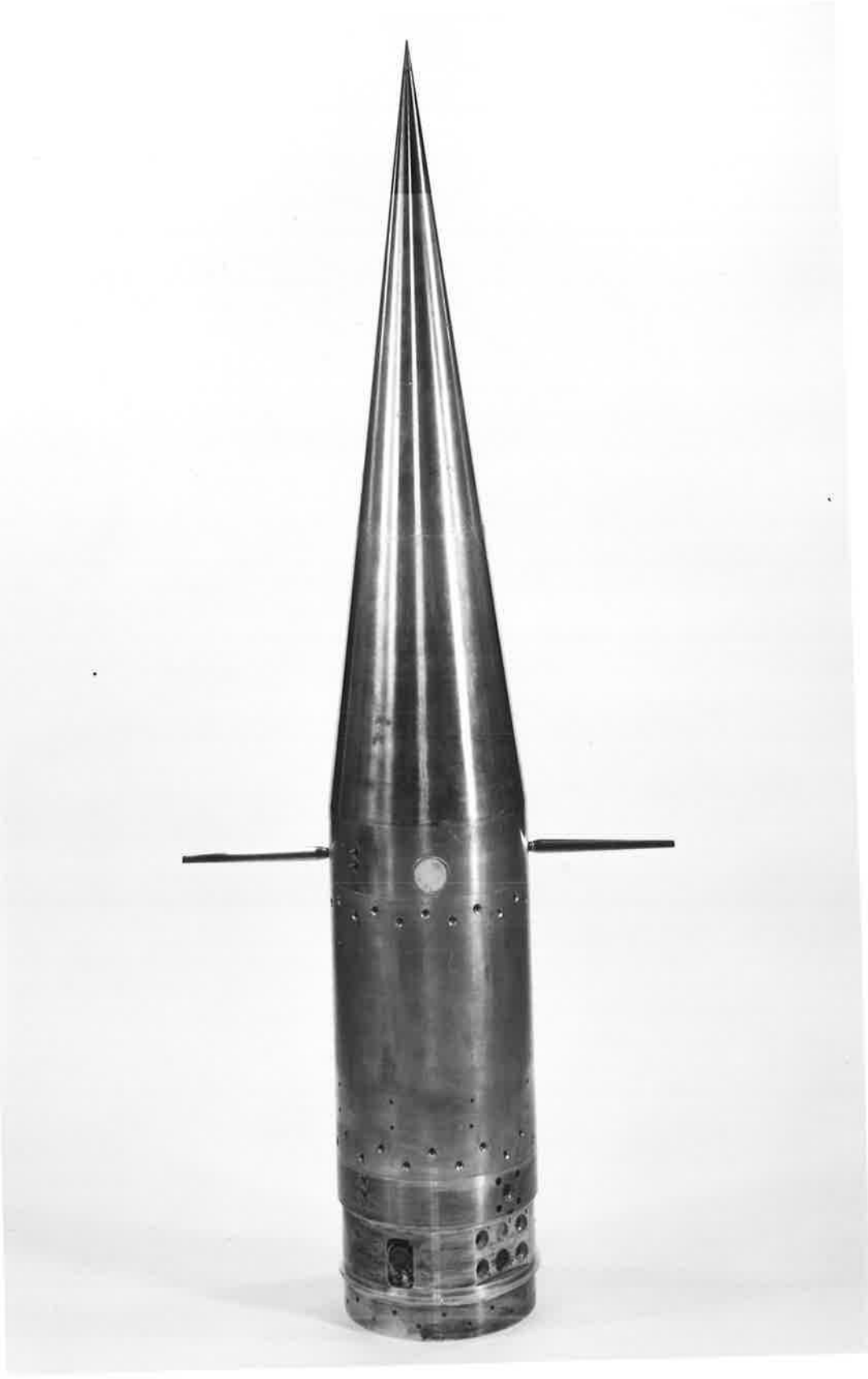

The drawbacks with sharing amplifiers were, first, that care had to be taken selecting chambers as both ion chambers had to take approximately the same input resistor for the amplifier; otherwise one signal may go off scale. Second, the zero drift in the amplifier was approximately double. There was a maximum of 2% of full signal level compared with 1% for one ion chamber. Both drawbacks can be overcome if the input resistor is chosen smaller than that required to give 1.5 Volt in full sunlight.

The aspect sensors and sunslits mounted in Banks A and C were displaced from center because of mounting difficulties but as the aspect angle for the rocket did not change considerably in flight (see Section 4.3.3.) no significant errors were introduced by these sensors not looking exactly in the same direction as the ion chambers.

Among the Explorer 30 photometers were Li F - NO and CaF_2 - NO ion chambers, which provided information for the comparison with the rocket determination of absolute fluxes over the range 1050 - 1350 Å and 1225 - 1350 Å. The spectral response and quantum efficiency of the Explorer 30 chambers were supplied by the U.S. Naval Research Laboratory.

4.3.2. ANALYSIS OF TRAJECTORY DATA

Before describing the method used for determining the

trajectory it would be useful to discuss the factors which cause the trajectory to deviate from the simple form $h(t) = h(o) - \frac{1}{2}gt^2$. (In this section all time measurements will be measured from the time of maximum height or apogee). The most important factors are (a) air drag, and (b) variation in the gravitational acceleration.

(a) Air Drag.

The effect of air drag is to make the trajectory unsymmetrical and the effect will decrease as the height increases. In this case the Lyman α detector does not respond until approximately 70 Km. so that the trajectory is only required from 70 Km. up and the effect of air drag may be ignored.

(b) Variation in the Gravitational Acceleration.

The value of g varies inversely as the square of the distance from the center of the earth but over a limited height range the decrease in g can be approximated by a linear formula and we may write

$$a(t) = -\{g_0 + k(h_0 - h(t)\} \qquad (1)$$

where $a(t)$ is the vertical acceleration of the rocket, g_0 is the value of g at the maximum height h_0, and k is a very small positive constant. ($k = 2.98 \times 10^{-6}$ sec^{-2} according to the U.S. Standard Atmosphere 1962).

As k is small and time is measured from apogee then

$$h_0 - h(t) \simeq \tfrac{1}{2} g_0 t^2 \qquad (2)$$

Therefore, $a(t) = -\{g_0 + \frac{1}{2} k g_0 t^2\}$ (3)

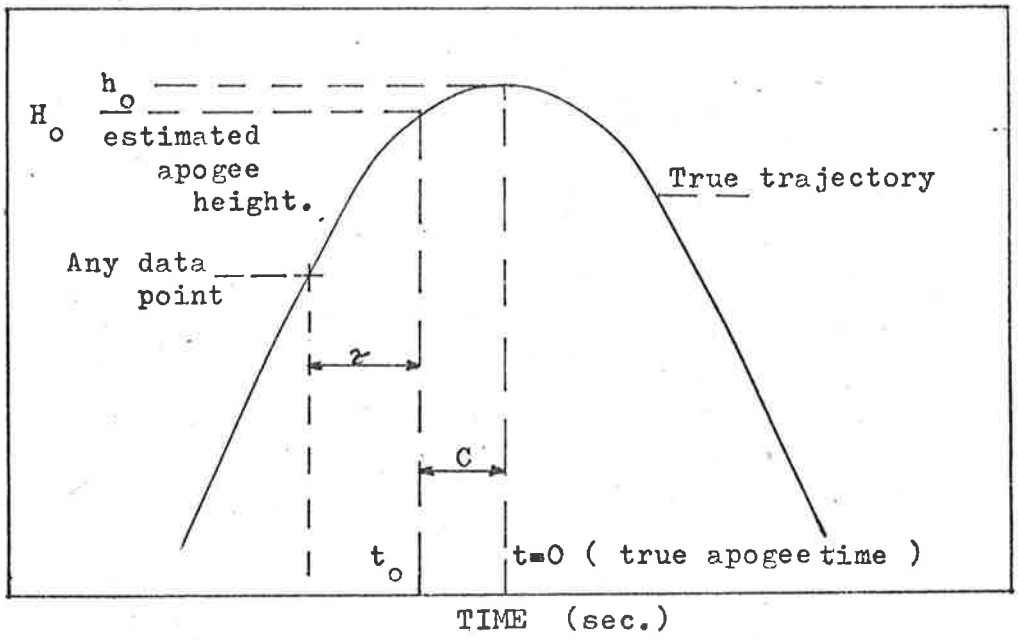

Fig. 4.3. Diagram illustrating the notation used for obtaining the true trajectory from raw radar tracking information.

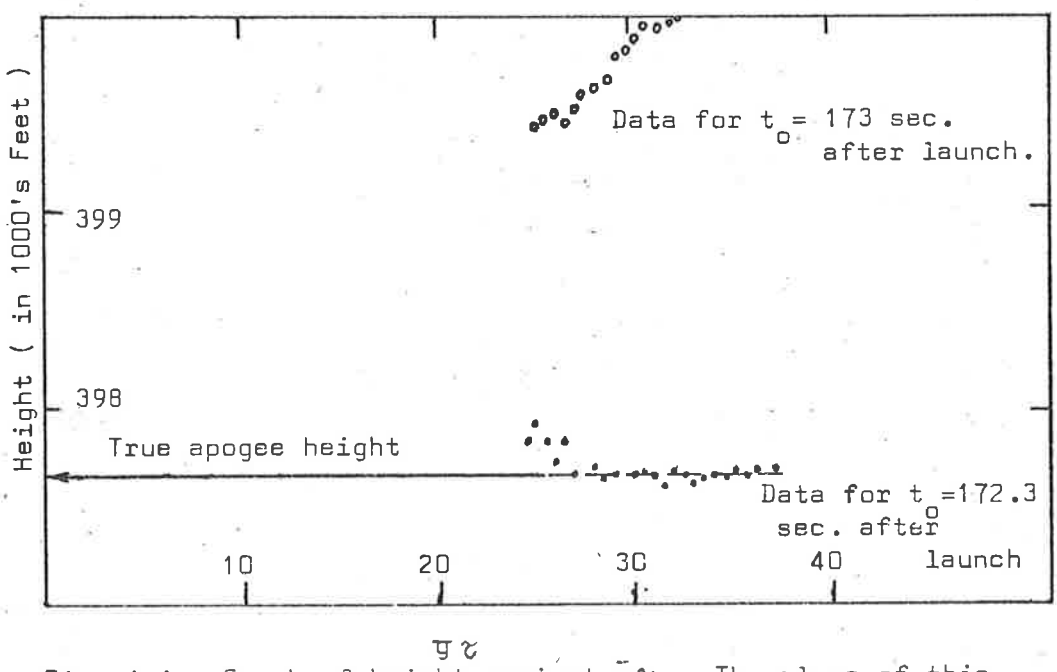

Fig. 4.4. Graph of height against $\bar{g}\tau$. The slope of this graph determines the error made in estimating the apogee time.

Then $v(t)$ = Vertical velocity of rocket

$$= \int_0^t a(t)\,dt = -\{g_0\,t + \frac{1}{6}\,k\,g_0\,t^3\} \qquad (4)$$

Note that $v(t) = 0$ when $t = 0$

$$h(t) = \int_0^t v(t)\,dt = h_0 - \tfrac{1}{2}\,g_0\,t^2 - \frac{1}{24}\,k\,g_0\,t^4$$

$$\text{or } h(t) = h_0 - \tfrac{1}{2}\,g_0\,t^2\,\{1 + \frac{1}{12}\,k\,t^2\} \qquad (5)$$

This equation describes quite accurately the trajectory taking into account variation in g. To use this equation two quantities have to be determined from the radar data. (a) h_0 or apogee height and (b) the apogee time as this defines when $t = 0$.

Unfortunately the radar data was not complete. Only a small section on the upward leg was available. From this data the following method was used to predict apogee time and height.

By plotting vertical velocity against time after launch, the extrapolation of this graph to $v(t) = 0$ will give a first estimate of apogee time.

Let t_0 = estimate of apogee time, $\tau = (t_0 - t)$ or the time from any data point to the estimated apogee time, H_0 = estimated apogee height and C = error between the estimated apogee time t_0 and the true apogee time (see Fig. 4.3).

Then H_0 approximately equals

$$H_0 \approx h(t) + \tfrac{1}{2}\,\bar{g}\,\tau^2 \qquad (6)$$

where $\bar{g}$ is average value of g over the range

$t = c$ to $t = \tau + c$

The true apogee height

$$h_0 = h(t) + \tfrac{1}{2}\,\bar{g}\,(\tau + c)^2$$

$$= h(t) + \tfrac{1}{2}\,\bar{g}\,\tau^2 + \bar{g}\tau c + \tfrac{1}{2}\,\bar{g}\,c^2$$

$$= H_0 + \bar{g}\tau c + \tfrac{1}{2}\bar{g}\,c^2$$

If the approximation for apogee time is very good c will be a small quantity and then $h_0 \simeq H_0 + \bar{g}\tau c$ (7)

To establish the average value of g, use is made of equation (3).

From equation (3) $g = g_0\{1 + \tfrac{1}{2}\,k\,t^2\}$

Therefore, $\bar{g} = g_0 \int_c^{\tau+c} (1 + \tfrac{1}{2}kt^2)\,dt \;/\; \int_c^{\tau+c} dt$

$$\bar{g} \simeq g_0\{1 + \frac{1}{6}\,k\,\tau^2\} \; * \qquad (8)$$

By using equations (7) and (8) the estimate of h_0 and c were determined in the following way:

(a) Estimate t_0 as mentioned previously

(b) Estimate H_0 and hence g_0

(c) From equation (7) if a plot of H_0 against $\bar{g}\tau$ is performed a straight line graph results of slope C and height intercept of h_0.

(d) The value of $\bar{g}$ can be obtained from equation (8).

---

*If equation (8) is substituted into equation (6) then

$$h(t) = H_0 - \tfrac{1}{2}\,g_0\tau^2\{1 + \frac{k}{6}\,\tau^2\}$$

when $c = 0$

then $h(t) = h_0 - \tfrac{1}{2}g_0\,t^2\,\{1 + \frac{k}{6}\,t^2\}$

This does not compare exactly with equation (5) because the approximations and method used for predicting h_0 and c are not the same approximations used for equation (5). The value for k is so small that either equation could be used with only minor errors in h(t).

By following this procedure a new value of apogee time can be determined and the procedure repeated until a horizontal graph for H_0 versus $\bar{g}\tau$ is obtained. (See Fig. 4.4). It was found that the trajectory for Long Tom was described accurately by the equation

$$h(t) \text{ km} = 121.15 - 4.722t^2|1+2.48 \times 10^{-7}t^2| \times 10^{-3}$$

Although this accuracy is not required for determining oxygen densities it is required for determining the maximum height and hence an accurate height scale.

4.3.3. ANALYSIS OF ASPECT DATA

Each time the rocket rolled and pointed the aspect sensors in the direction of the sun a peak occurred on the telemetry record for that sensor. As mentioned previously (see Chap. 3) the ratio of the signals from a pair of sensors would be dependent on the aspect angle and not on the intensity of the visible light from the sun. It was found that whenever the ratio of sensors 1 and 2 in bank A was a particular value, the signal from sensor 1 was also a particular value. This meant that in the height range considered the output from sensor 1 was proportional to the aspect angle. The same applied for bank C.

At 139 seconds after launch the ratio of the aspect sensors indicated that the aspect angle was zero. This was achieved by comparing the ratio with that obtained by laboratory

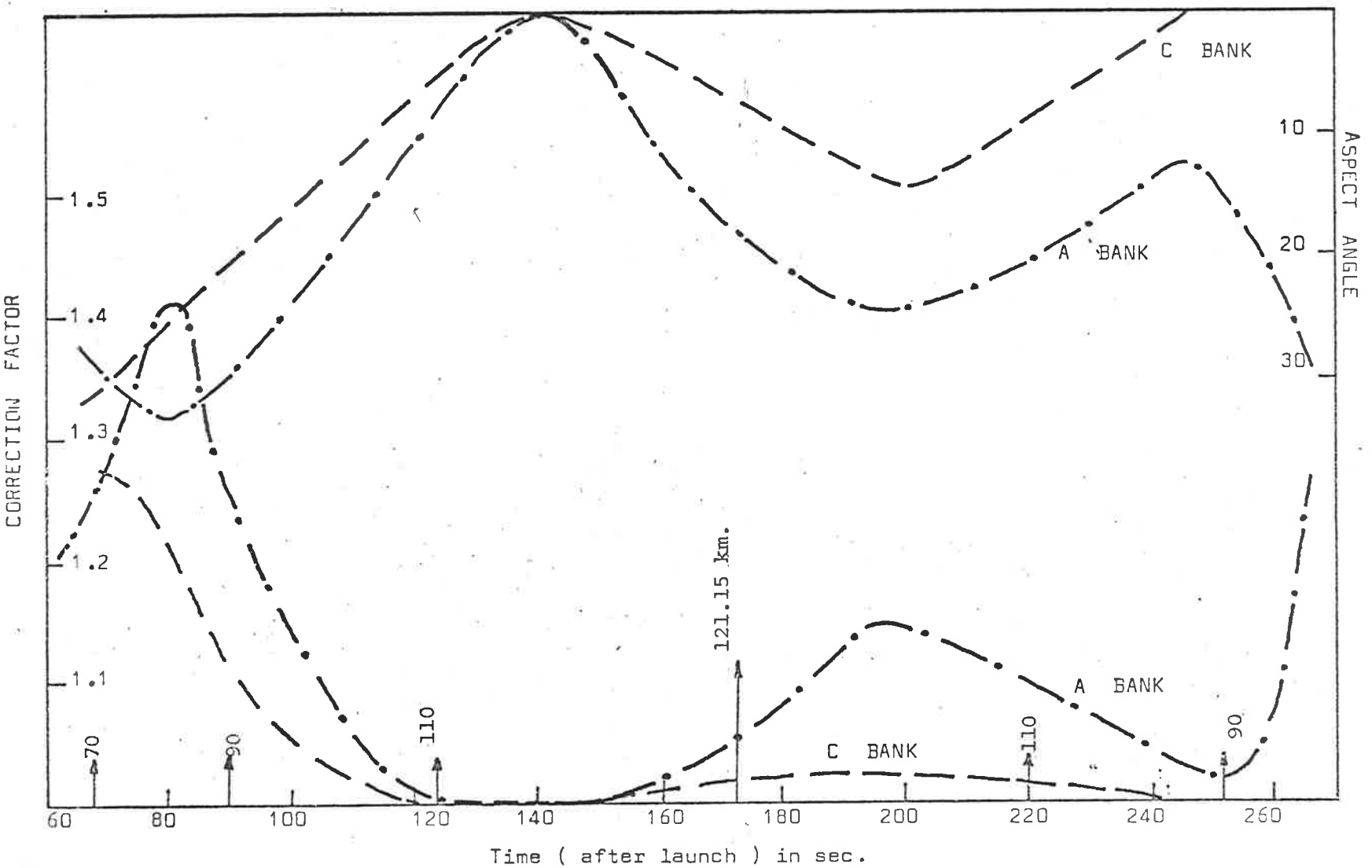

Fig. 4.5. The aspect angle and correction factor for aspect from the Long Tom rocket flight.

calibrations. The sunslits even though they were displaced from the aspect sensors also indicated approximately zero aspect.

One spike on the telemetry record for the sunslits indicates either a zero aspect or an aspect greater than 50^{o}. The 50^{o} possibility was ruled out as at this angle the signal from the aspect sensors should be very low and this was not the case. The fact that the ratio of the aspect sensors agreed with the laboratory calibration provided independent confirmation of the laboratory calibration.

As there was at least one point in the flight where the aspect angle was known meant that aspect sensor 1 (flush teflon) in each bank could be calibrated to give aspect angle directly. Also as this one point coincided with zero aspect, an in-flight calibration of the way in which the detector signal varied with angle could be made. This in flight calibration agreed very well with the laboratory calibration. Calibrating one sensor in each bank meant a considerable simplification in determining aspect angles, for the complete flight. Using the calibration obtained during the flight the rocket aspect angle was determined for the period during which the height of the rocket was between 70 Km. and 121.15. This is shown in Fig. 4.5. The angular response of the ion chambers were also determined from the signal obtained during one roll of the rocket when the aspect angle was 0^{o}, and was found to agree well with the calibration made before the flight. The

calibration made during the flight was used to derive the correction factor (see Fig. 4.5) by which the peak height of the signal from the ion chambers had to be multiplied to convert it to zero aspect angle. As all the ion chambers were basically of the same geometry the correction factor for one ion chamber applied for all the different types. The Sapphire-Xylene ion chamber had a thinner window than the others but the difference in the angular response of this ion chamber with the others was found to be negligible.

It can be seen from Fig. 4.5 that the correction factor was never greater than 1.41 in the height range 70 to 121 Km. and for most of the flight less than 1.15. The greatest correction factors occur in the 70 Km. to 90 Km. region which is the absorption region for Lyman-α. An error of 5% occurred with the aspect angle which in this height region corresponds to a 10% error in the correction factor. Therefore the molecular oxygen density profile must be slightly more in error for this region than the rest of the flight.

4.3.4. MOLECULAR OXYGEN DENSITY PROFILE

Figure 4.6 which includes data from both the upward and downward portion of the flight, shows, as a function of altitude, the measured response of the different ultraviolet and X-ray detectors after corrections for zero aspect angle and amplifier drift (see Section 3.3.6.) had been made. There is no significance in the relative intensities shown for the different detectors.

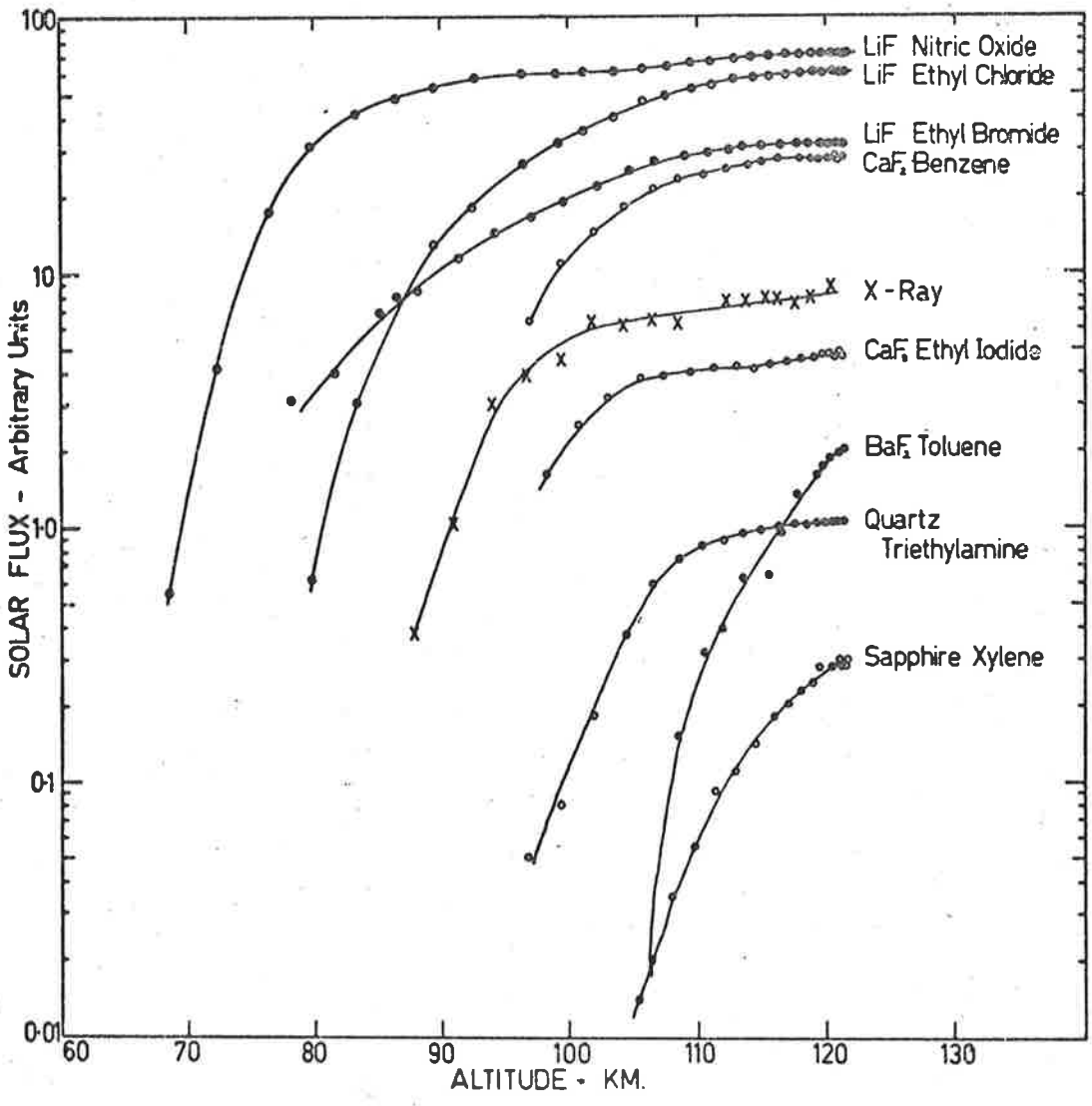

Fig.4.6. Solar ultra-violet and X-ray fluxes measured by each detector as a function of rocket altitude. The Figure indicates the shapes of the measured atmospheric absorption curves. There is no significance in the relative intensities shown for different detectors.

In principle the molecular oxygen density is proportional to the slope of the response curves, but in practice the analysis is best carried out by determining the average densities in a series of equal height intervals, h, within which the number density, n, is constant and that the attenuation of the solar flux over a height interval h is given by

$$\exp(-hn\,\sigma\sec Z)$$

where σ is the absorption cross section and Z the solar zenith angle (48° in this case). The densities derived in this way for a layer height of 2.5 Km. are shown in Figure 4.7 using the cross sections listed in Table 4.1. The total atmospheric density derived from the X-ray absorption measurements (upper histogram) is compared in Fig. 4.7 with the 1962 U.S. standard atmosphere values (full curve) and it may be seen that there is fair agreement in the altitude range 90 - 110 Km. Below an altitude of 90 Km. the derived molecular oxygen densities depend upon measurements made with the Li F - nitric oxide, (Lyman - α), ion chamber. At higher altitudes there is very good agreement between the oxygen density determinations obtained independently from the BaF_2 - toluene, CaF_2 - benzene, CaF_2 ethyl iodide, sapphire - xylene and quartz - triethylamine chambers; the lower histogram shows the average of the molecular oxygen densities determined by all ion chambers. The observed molecular oxygen density profile below 90 Km. runs very nearly parallel to the standard atmosphere total density curve but at higher altitudes the effects of

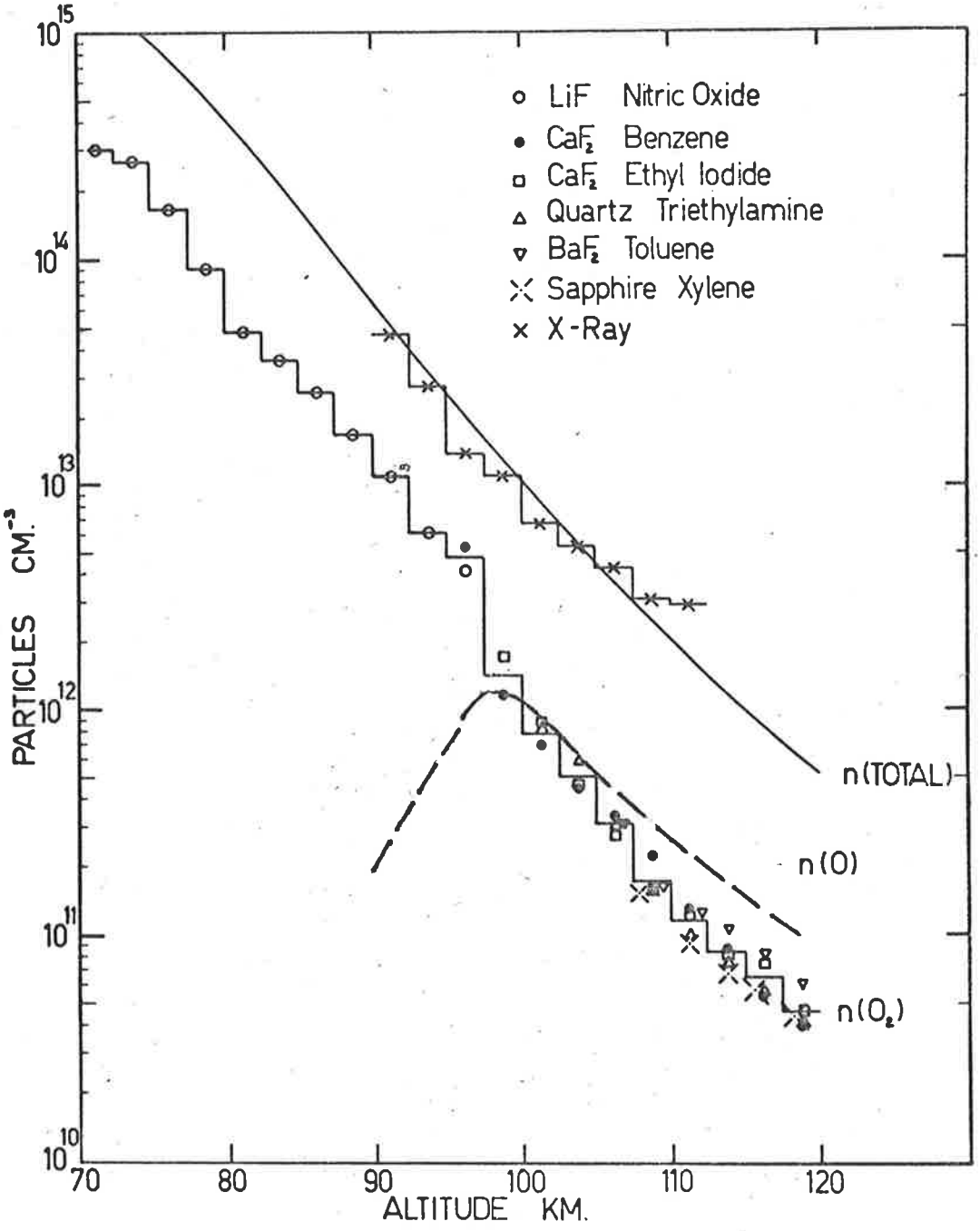

Fig. 4.7. Particle density profiles as a function of altitude. Upper histogram: total particle density determined from X-ray observations. Lower histogram: average value of ion chamber determinationsof molecular oxygen density. Full curve: 1962 U.S. standard total number density. Dotted curve: atomic oxygen number density inferred from present measurements.

molecular dissociation are clearly evident.

The dotted curve in Figure 4.7 shows the atomic oxygen density profile implied by the measured molecular oxygen and total density profiles (the latter is not significantly different from the 1962 U.S. standard).

The present results suggest that the atomic oxygen concentration exceeds the molecular oxygen concentration above 100 Km. A comparison of these results with others will be made in chapter six.

4.3.5. SOLAR FLUX

The data shown in Fig. 4.6 have also been used to determine absolute solar ultra-violet fluxes in terms of the laboratory calibrations of each of the ion chambers. Some of the ion chambers (e.g. BaF_2 - toluene, sapphire - Xylene) are sensitive to radiation which is very strongly absorbed in the atmosphere and did not reach saturation currents at the maximum rocket altitude of 121 Km. It was necessary therefore to extrapolate the measurements to zero optical depth and this was done by assuming that the observed molecular oxygen density curve of Fig. 4.7 could be extended to higher altitudes with constant scale height i.e. by plotting the logarithm of the flux as a function of the absorbing mass in units of slant mass above 100 Km.

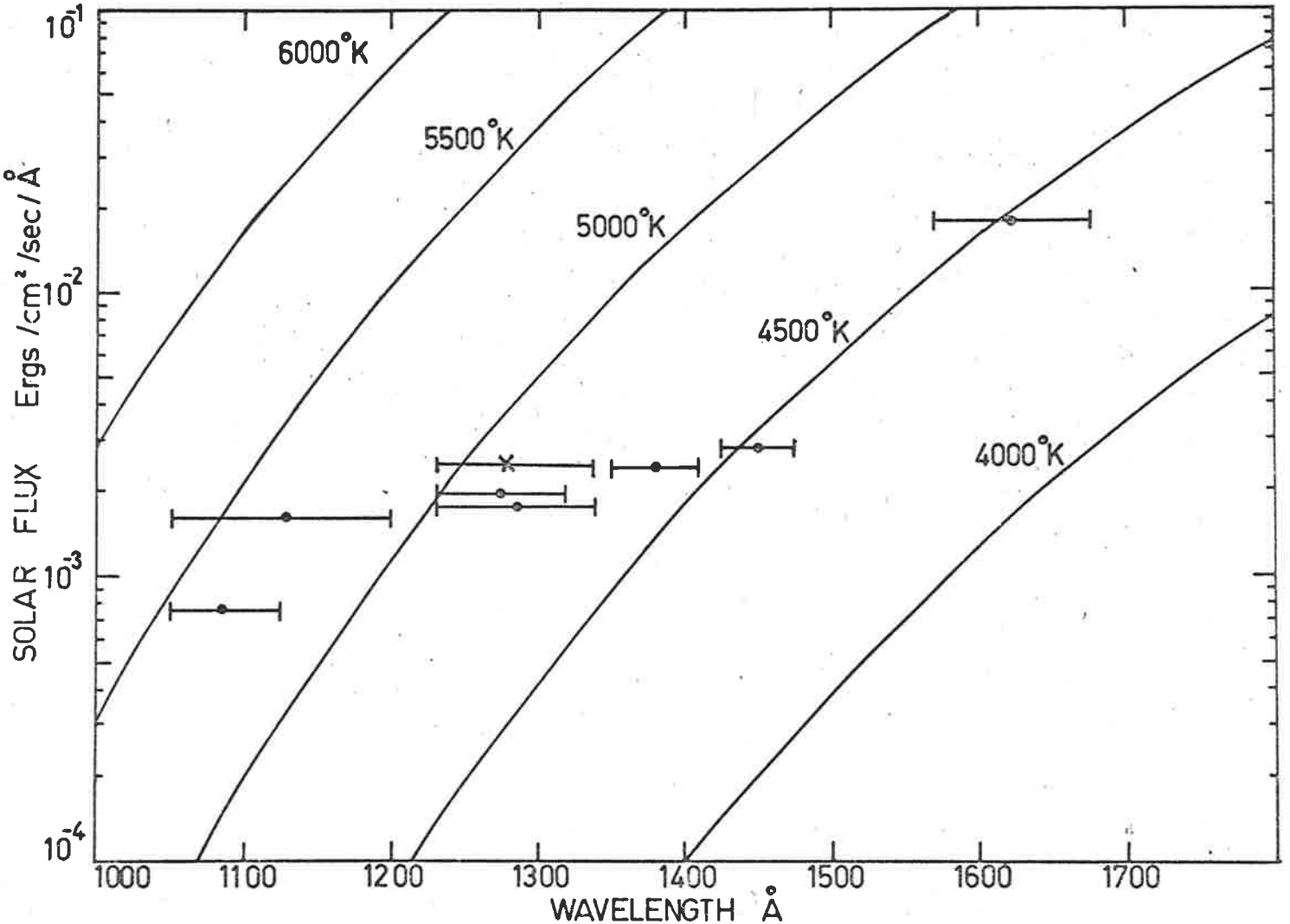

Fig. 4.8. Solar ultra-violet intensity distribution according to present ion chamber measurements compared with black body curves. The cross indicates the solar flux measurement made with a CaF_2-NO ion chamber on Explorer 30.

The solar ultra-violet fluxes determined in this way are shown in Fig. 4.8 where they are compared with the fluxes corresponding to various solar black body temperatures. The cross indicates the Explorer 30 Calcium Fluoride - nitric oxide ion chamber results and the bars indicate the effective band pass of the various ion chambers. Tousey's (1963) measurements of the solar spectrum suggest that for wavelengths longer than 1340 Å the solar flux is predominately in the continuum. The (small) contribution from emission lines was ignored and the results indicate that from 1400 Å to 1600 Å the continuum flux corresponds to that of a black body at a temperature of 4500°K; between 1000 Å and 1100 Å the equivalent black body temperature has increased to 5300°K.

Ion chambers with their comparatively broad spectral sensitivities respond both to solar ultra-violet emission lines and to continuum radiation. In the case of the lithium fluoride - nitric oxide chamber, the solar Lyman α line is by far the strongest source within the bandpass of the detector. This line, as it corresponds with a "window" in the oxygen absorption cross section, penetrates more deeply into the atmosphere than other radiation within the band pass of the detector. At higher altitudes there is a small but significant ion chamber response to other radiations as shown by the rise in ion chamber current above 95 Km. The Lyman α contribution to the ion chamber current

can be clearly identified from the atmosphere absorption curve as the curve flattens out from about 90 to 95 Km. This contribution amounts to approximately 85 per cent of the total current which would be observed above the atmosphere. For the Explorer 30, lithium fluoride - nitric oxide chamber the Lyman-α contribution was calculated to be 81 per cent. The measured Lyman-α flux was found to be 4.25 erg/cm^2/sec., which was in excellent agreement with the Long Tom flux value of 4.2 erg/cm^2/sec. (These points are not represented on Fig. 4.8).

Explorer 30 X-ray detectors indicated the existence of a solar flare, lasting for approximately 2 to 5 minutes, which peaked one minute after the Long Tom rocket flight. This indicated that all rocket flux measurements taken were values for quiet conditions. The Lyman-α flux measured from Explorer 30 suffered no significant change during the flare. (Carver et al 1969).

CHAPTER 5. WRESAT (AUSTRALIA'S FIRST SATELLITE)

5.1.1. INTRODUCTION

WRESAT (Weapons Research Establishment Satellite) involved the design, development and launching of a small scientific satellite from Woomera. The scientific objectives of the satellite were to extend the work already done by the Long Tom rocket flight. Experimentation was designed to provide information on molecular oxygen densities in the height range 100 to 180 Km. and solar fluxes in both the ultraviolet region between 1050 and 1660 $\mathring{A}$ and X-ray at 8 $\mathring{A}$. In measuring oxygen densities from a satellite, it was planned that information would be obtained on day to day variations and seasonal variations. In addition to these objectives, experimentation was included to determine ozone densities in the upper atmosphere and to measure the albedo of the earth in the wavelength band 1050 to 1350 $\mathring{A}$ as well as the intensity of resonantly scattered Lyman-α radiation from the geocoronal hydrogen belts.

The actual satellite was developed by Weapons Research Establishment and the Physics Department, University of Adelaide. The U.S. Department of Defence provided the launch vehicle and the U.K. Ministry of Technology, through its association with Woomera, the launch facilities. In addition, the U.S. National Aeronautics

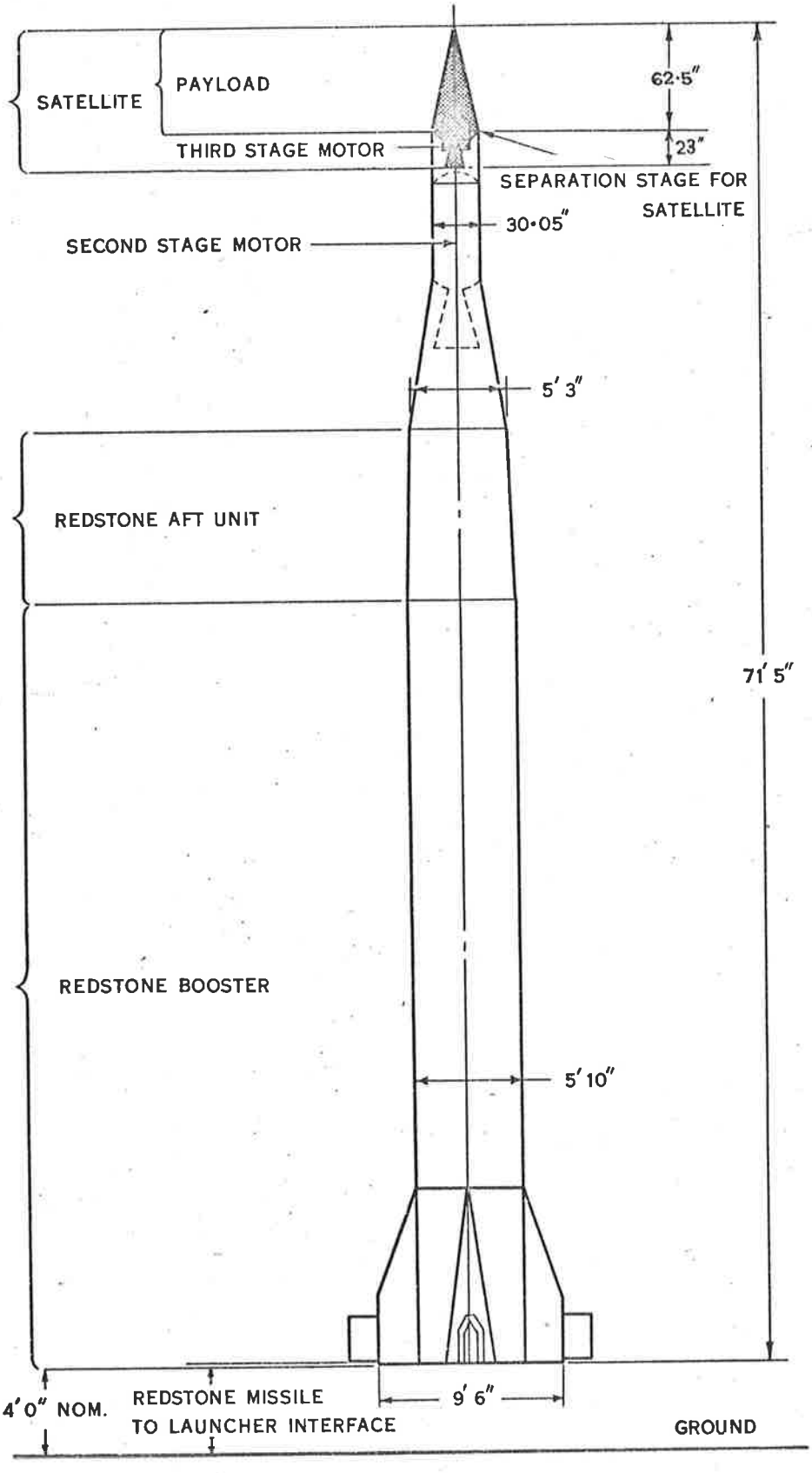

Fig. 5.1. Sparta missile with the WRESAT satellite.
(from WRESAT information booklet 1967)

and Space Administration supported the project with satellite tracking and data acquisition.

The launch vehicle was a Redstone first stage modified to accept two solid propellant upper stages. The complete vehicle was about 70 feet high, 6 feet in diameter and weight of approximately 57,000 lb. at launch. (see Fig. 5.1). The conical satellite including the experiments and instrumentation weighed about 100 lb. and had a base diameter of about 30 inches and a height of about 5 feet. The third stage motor was not jettisoned after burnout but went into orbit with the satellite cone. This was done as no operational penalties were involved and there were less mechanical complications in the design. This made the total weight of the orbiting body approximately 160 lbs.

The satellite cone was made of light alloy frames and skin, and all instrumentation units were thermally isolated from the main flight structure. The outside of the cone was painted with special high temperature black paint so that a satisfactory temperature within the cone would be obtained during the orbit phase. Inside of the cone was painted white to assist in obtaining temperature equilibrium of the internal equipment.

Comprehensive environmental testing of the satellite was undertaken by Weapons Research Establishment. This included

vibration testing, static and dynamic loading, testing at elevated temperatures and dynamic balancing. In addition the complete satellite was tested in a vacuum chamber at the Physics Department, University of Adelaide, at a pressure of 10^{-5} mm of Hg while being cycled in temperature between +50°C and -15°C, over a period of about one week, running from an external power source. Satellite power was obtained from batteries which limited its transmitting lifetime to 5 days, although its orbital lifetime was about 40 days.

The satellite WRESAT, 1967-118A, was launched from Woomera on November 29th, 1967. After burnout of the Redstone first stage it was jettisoned and the rest of the vehicle allowed to coast to a height of about 100 n miles. During this time the inertial guidance unit caused the vehicle to be pitched into an approximately horizontal position. The vehicle was then spun to a roll rate of 2.5 rev/sec before ignition of the second stage motor. After burnout the second stage was discarded and the third stage ignited injecting the satellite into orbit with a tangential velocity of 26000 ft/sec at a height of 100 n miles, a latitude of near 27°S and an azimuth angle of about 6° East of North from Woomera. A nearly polar elliptical orbit was obtained with an apogee of 700 n miles and a perigee height of 100 n miles. (see Fig. 5.2).

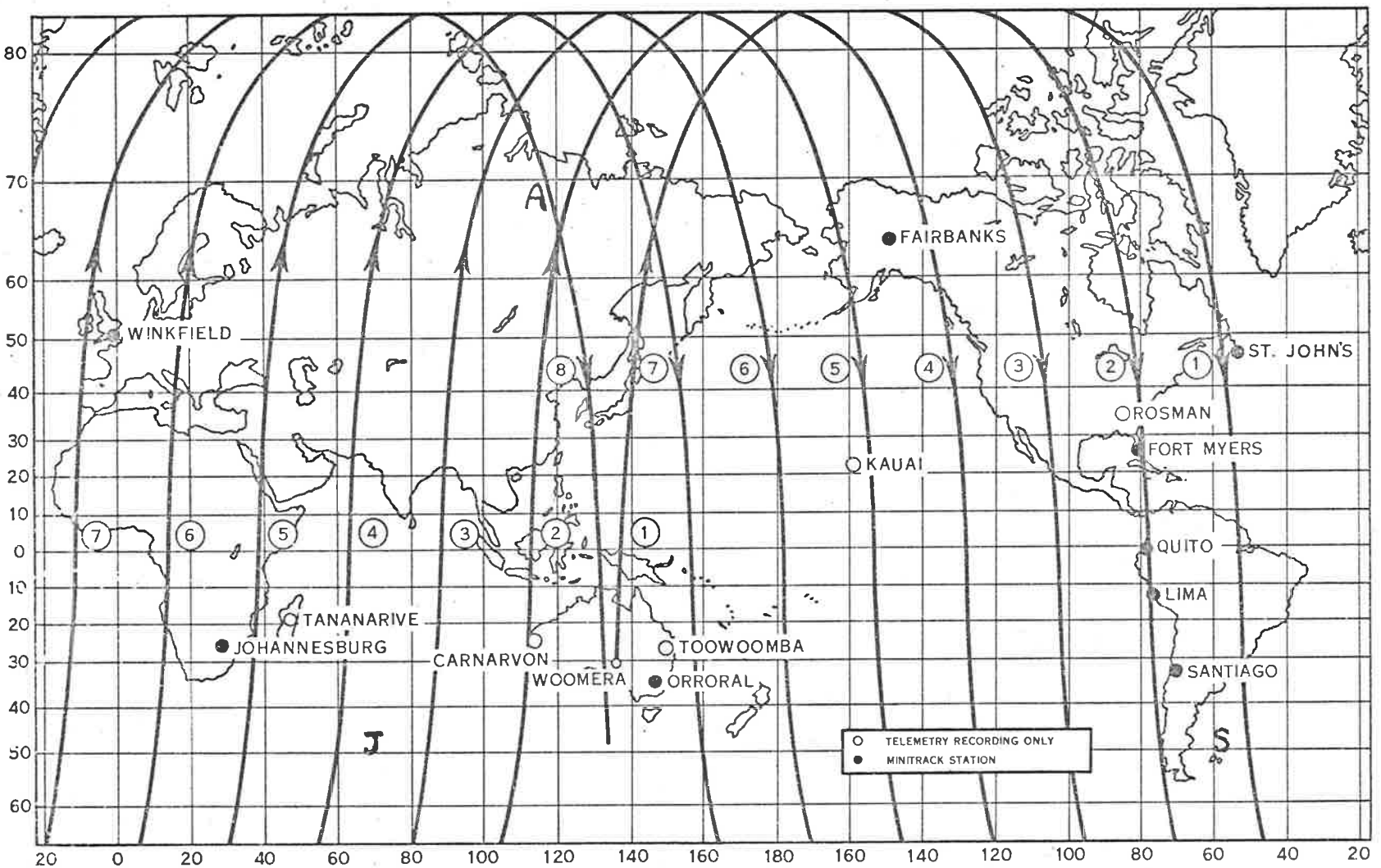

Fig. 5.2. The first eight orbits of the WRESAT satellite. The large letters indicate the minimum ray height position for the three satellite passes considered in this work.

The satellite, including the burnt out third stage motor entered orbit with a spin rate of 2.5 rev/sec about the cone axis; the attitude of this axis was about 27^{o} to the earth's rotational axis. Theoretically if the satellite was a rigid symmetrical body, not acted on by external forces, this attitude would be maintained. But, as the satellite was not infinitely rigid and balanced perfectly the axis of spin would nutate and the motion would assume that of a flat spin about the axis of maximum moment of inertia. This axis was normal to the satellite cone axis and parallel to the original spin axis on insertion into orbit. The rotational rate of the flat spin was approximately one half a revolution per second, as the ratio of the moments of inertia about cone axis and flat spin axis was 1:5. As the satellite would assume this motion it was decided to make use of the flat spin in the positioning of the detector banks in the satellite. One detector bank was placed in the nose of the satellite and another at the side. This meant that as the satellite spun, first the nose bank would look at the sun and then the side. In order to encourage this flat spin mode an energy dissipator was placed inside the satellite. This was of the form of a hollow tube partially filled with silicon oil running around the satellite in the plane of the cone axis. The energy dissipator worked extremely well as the transfer of the motion from the original to the final rotational mode occurred within the first orbit.

5.2.1. SATELLITE INSTRUMENTATION

The WRESAT experiment was designed to provide information on molecular oxygen density in the height region 100 to 180 Km., density of ozone, solar flux in both the X-ray (at 8 Å) and ultra-violet region between 1050 and 1660 Å. A Lyman-α telescope, containing the gas gain ion chamber described in Section (3.3.7.) was also flown. The telescope was flown to determine the albedo of the earth in the wavelength band 1050 to 1350 Å and to measure the resonantly scattered Lyman-α radiation from the geocoronal hydrogen belts. These measurements formed the inputs to two basic experiments which would extend the work done in the Long Tom rocket flight. They were (a) the sunset-sunrise experiment and (b) the orbital measurements in sunlight.

(a) The Sunset-Sunrise experiment.

Whenever there occurred a satellite sunrise or sunset, radiation from the sun would reach the satellite after passing through the atmosphere close to the earth. (see Figure 5.5). As the satellite continued on its orbit, radiation from the sun reached the satellite through different regions of the atmosphere and hence, as this radiation was detected, profiles of molecular oxygen and ozone may be determined. The ozone sensor was a photo-diode sensing the solar flux after transmission

through an interference filter centered around 2500 Å in the Hartley band. During the launch phase the interference filter became broken and hence this experiment provided no information on ozone concentration.

The instruments which were included to determine molecular oxygen concentrations were the same as that flown in previous rocket flights. The lithium fluoride-nitric oxide, Sapphire-Xylene and the Quartz-Triethylamine ion chambers were chosen as these chambers provided data which overlapped between the height range 100 to 180 Km. The Quartz-Triethylamine chamber (1560 to 1660 Å) was chosen in preference to other ion chambers flown in the Long Tom flight as this chamber had not previously been flown from a satellite vehicle and provided valuable information on solar flux. As the satellite had a short transmitting lifetime, no protection was provided for the ion chambers against deterioration of the filling gases by prolonged exposure to ultraviolet radiation.

The experiment block located forward, looking from the nose, the tip of which was separated after injection, comprised three ion chambers (one of each type), the ozone sensor and a set of aspect sensors. The sideways looking instrumentation of three ion chambers, the

Lyman-α telescope, X-ray counter and aspect sensors was in the same rotational plane as the forward looking sensors but perpendicular to them. Figure 5.3 shows the satellite during construction. The arrangement of the sideways viewing experimental block can be clearly seen. The solar aspect sensors were identical with those flown previously relying upon the response of a photo-transistor to the light collected from a flat teflon surface and a nipple of teflon. Originally two magneto-meter units were included to determine aspect at night and provide attitude information during the day as well as providing a check on the solar aspect sensors. One of the magnetometer units had to be left off the satellite because of weight considerations. This meant that the aspect angle determination for the sideways detector block relied almost exclusively on the solar aspect sensors. It had to be assumed that the attitude of the satellite would not change significantly during the night.

Basically, the experiments were the same as used on previous rocket experiments but there were two important changes in the instrumentation necessitated as they were flown in a satellite. The first of these was in the amplifier for the ion chambers and the Lyman-α telescope and the second in the telemetry system. (see Sections 5.2.2. and 5.2.3.).

Fig.5.3. A view of the WRESAT satellite during construction. The sideways facing experiment block,in which the detectors are protected by teflon caps,can be seen. The white tube on the right is the energy dissipator which converted the spin mode of the satellite into a flat spin within one orbit.

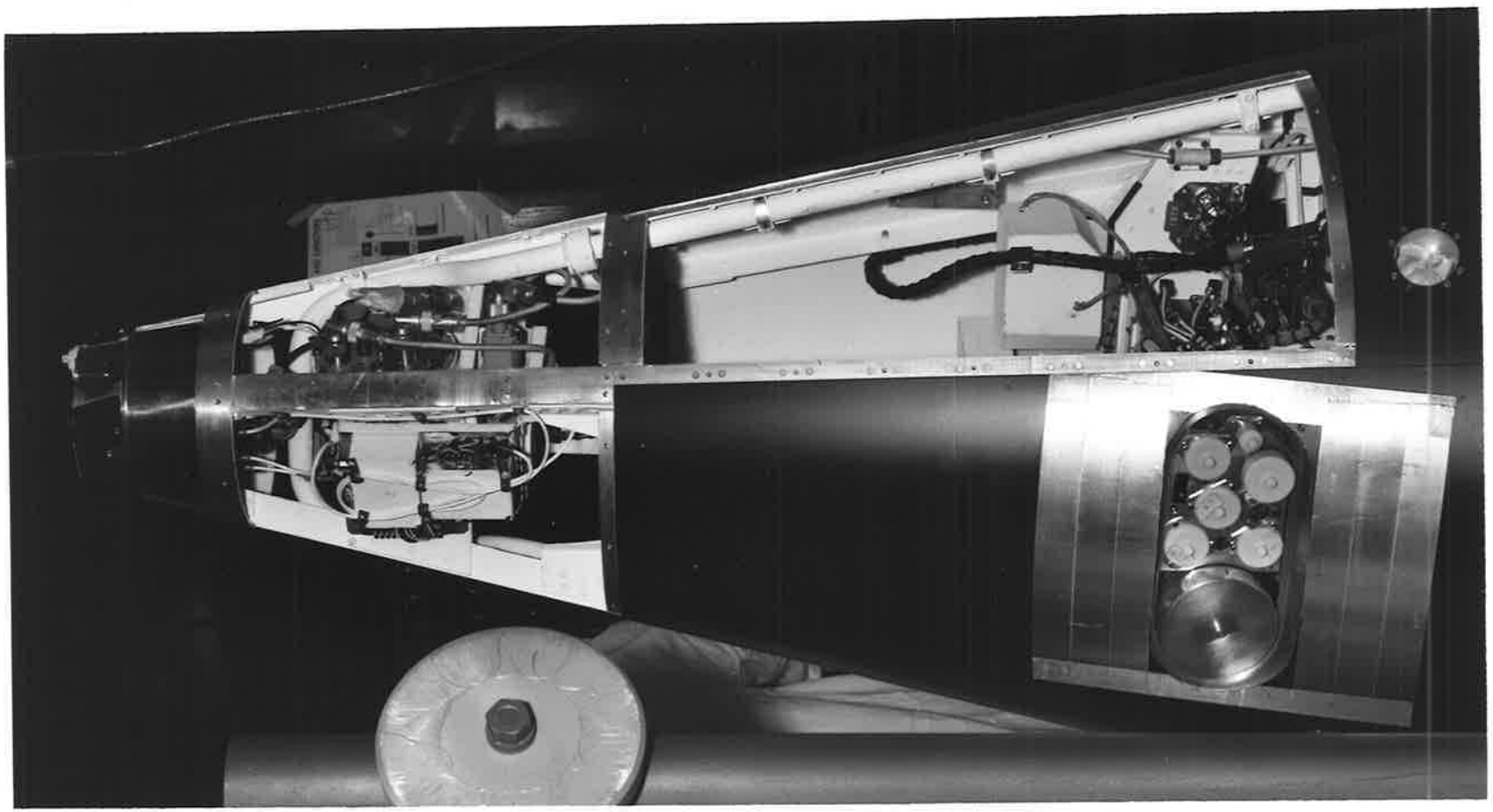

(b) Orbital measurements in sunlight

The orbital daylight experiment provided measurements of the solar flux in the ultraviolet and X-ray wavelengths. The X-ray counter was collimated and had a mica window with a gas filling of neon and argon. The response was a narrow window centered at 8 Å. This detector as well as measuring X-ray fluxes responded to particle fluxes so that a monitor was available on the activity of the sun. In measuring X-ray flux at sunrise and sunset a total atmospheric density profile could be obtained and by combining this information with molecular oxygen data, atomic oxygen densities can be determined. However, sunset and sunrise passes were marred by high particle fluxes.

The ion chambers provided data on the intensity of the solar Lyman-α flux as well as in the important region from 1400 to 1660 Å. Measurements of the intensity in this region on the Long Tom rocket flight implied an equivalent black body temperature of 4500°K. As this temperature was about 250°K less than that estimated previously, the solar flux measurements were extremely important in verifying the Long Tom result.

5.2.2. THE AMPLIFIERS USED IN WRESAT

As the output from the Lyman-α telescope could not be accurately estimated it was decided to fly a logarithmic amplifier instead of the linear amplifier flown in Long Tom. This amplifier was made such that it would give a voltage output from zero to five volts for an input current from 10^{-12} amp to 10^{-8} amp i.e. 1.2 volts per decade. Calibration for the amplifier during flight was also different from the linear rocket amplifier in that a current of 2×10^{-9} amp was fed in every 30 seconds and the output monitored. This calibration pulse was then used to correct the signal from the detector. As this amplifier required different supply voltages than the linear amplifier it was decided to use logarithmic amplifiers for the ion chambers. The logarithmic amplifier with this current range was suitable for the sapphire-Xylene and quartz triethylamine ion chamber but for the lithium fluoride-nitric oxide ion chamber the current range was too sensitive. Therefore, a less sensitive amplifier was developed for the lithium fluoride-nitric oxide ion chamber with a current range from 10^{-10} amp to 10^{-6} amp and a calibration current of 1.7×10^{-7} amp.

Apart from the obvious advantage of current range of the logarithmic over the linear amplifier the logarithmic amplifier has one main disadvantage; that is the time constant, with the most sensitive amplifier. The rise time for the amplifier was

very fast but the fall time was slow. This meant that when the ion chamber scanned the sun the signal would be the correct shape for the upward portion of the scan but the tail of the signal would be distorted. As only the maximum value of the signal was used for molecular oxygen densities and solar flux measurements, this distortion would not directly affect these measurements.

5.2.3 WRESAT TELEMETRY SYSTEM

The 465 MH_z telemetry system used by Weapons Research Establishment in rocket flights was not suitable for WRESAT. As tracking and data acquisition was being performed by the National Aeronautics and Space Administration, a telemetry system compatible with their system had to be employed. The system used was purchased from the U.S.A. and sampled 256 samples per second. The sampling format was in the form of a sixteen by eight matrix where each position was sampled in turn and the complete matrix scanned in half a second. This meant that each of the 128 sample positions had to be allocated to the experiments and to general engineering and voltage monitoring. Figure 5.4 shows the allocation of the different experiments to particular positions in the telemetry matrix. Notice that each particular experiment was sampled as close as possible to equal intervals of time and not bunched together.

S	S	S	S	L	I1f	I2f	I3f	A1f	A2f	O_3	I1s	I2s	I3s	A1s	A2s
5V	OV	Th1	X	Th7	I1f	I2f	I3f	A1f	A2f	O_3	I1s	I2s	I3s	A1s	A2s
5V	Clock	Th2	L	Th9	I1f	I2f	I3f	A1f	A2f	O_3	I1s	I2s	I3s	A1s	A2s
5V	OV	Th3	X	M	I1f	I2f	I3f	A1f	A2f	O_3	I1s	I2s	I3s	A1s	A2s
OV	HK1	Th4	Th6	L	I1f	I2f	I3f	A1f	A2f	O_3	I1s	I2s	I3s	A1s	A2s
OV	5V	Th5	X	Th7	I1f	I2f	I3f	A1f	A2f	O_3	I1s	I2s	I3s	A1s	A2s
5V	HK2	HK3	L	Th9	I1f	I2f	I3f	A1f	A2f	O_3	I1s	I2s	I3s	A1s	A2s
OV	5V	Th8	X	M	I1f	I2f	I3f	A1f	A2f	O_3	I1s	I2s	I3s	A1s	A2s

LEGEND.

A1f = Flush, forward facing, aspect sensor.
A1s = Flush, sideway " " "
A2f = Protruding, forward facing, aspect sensor.
A2s = " sideway " " "
I1f & I1s = LiF - NO ion chamber.
I2f & I3s = Sapphire - Xylene ion chamber.
I3f & I2s = Quartz - Triethylamine ion chamber.

S = Syncr. channel.
Th = Thermistor.
M = Magnetometer.
L = Lyman - Telescope
X = X-ray Experiment
HK = Housekeeping channel
O_3 = Ozone experiment.

Fig. 5.4. Allocation of experiments to the telemetry system matrix. The telemetry system scanned horizontally. i.e. Starts with S,S, to A2s, and then to 5V.

The telemetry system as a whole worked extremely well during the satellite's lifetime and although all experiments could have done with more samples per second, sufficient points were available to define the shape of the signals from the detectors.

It was because of the sampling rate available that sunslits were not included in the experiment blocks. To define the spikes which occur on the sunslit signal, a very large number of samples were required which would be at the expense of the other experiments involved.

5.3.1. THEORY OF THE SUNSET-SUNRISE EXPERIMENTS

The flux of radiation (ϕ) at the observing point is related to the incident flux (ϕ_0) by the absorption law as given in Chapter 2.

$$\phi = \phi_0 \exp(-\sigma n_T) \qquad (1)$$

where σ is the absorption cross-section at the wavelength of radiation and n_T is the columnar number density between the observing point and the source.

In its differential form, equation (1) becomes

$$\frac{1}{\phi}\frac{d\phi}{dz} = -\sigma\frac{dn_T}{dz} \qquad (2)$$

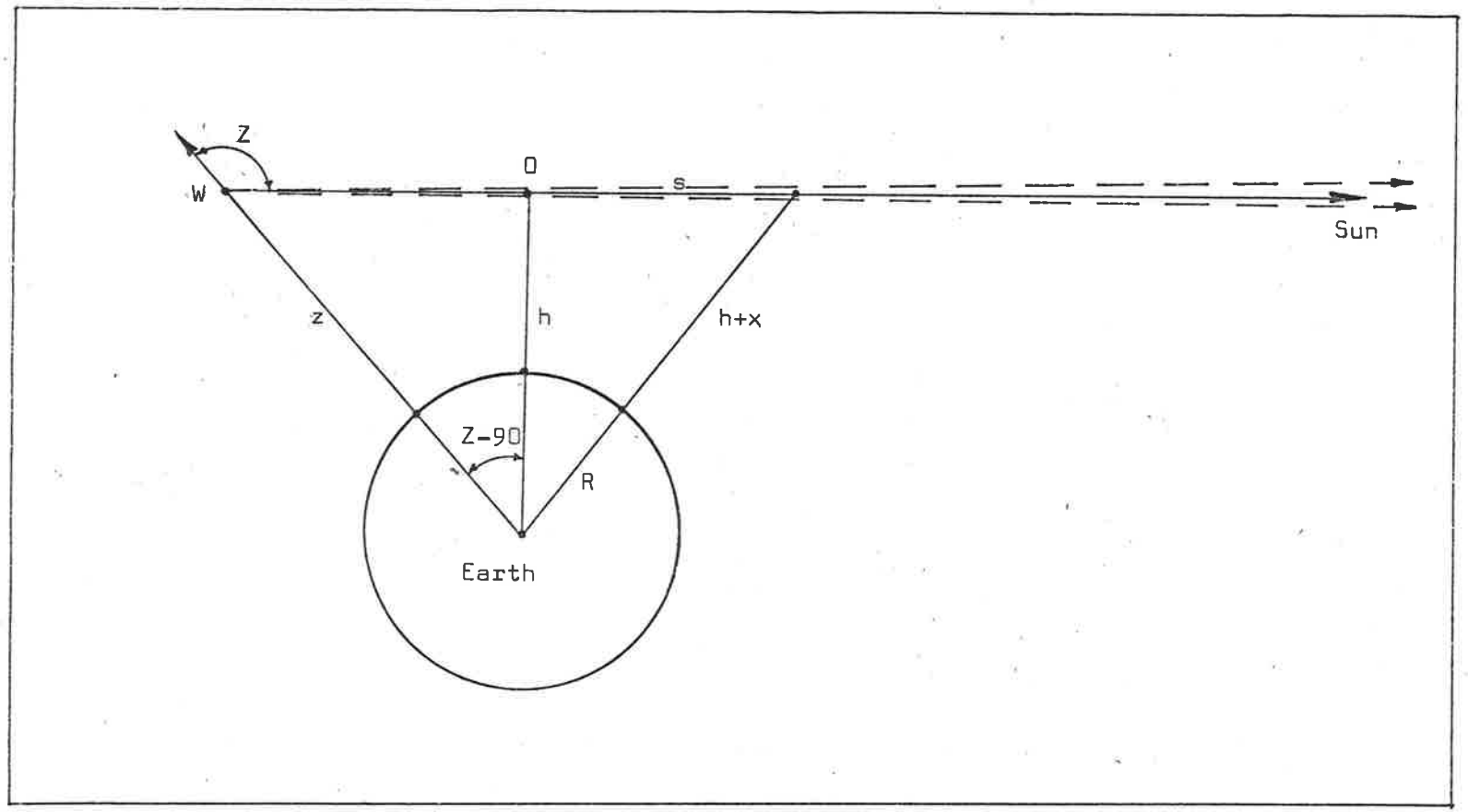

Fig. 5.5. The goemetry of the satellite sunrise-sunset experiment. The dashed lines indicate the errors which exist in the minimum ray height (h) when the sun is considered as a point.

The evaluation of n_T for the earth's atmosphere in the most general case presents considerable mathematical difficulty, but several approximate expressions have been developed.

When the solar zenith angle is not too large, the curvature of the earth may be ignored. This was done for the Long Tom rocket flight. where

$\frac{dn_T}{dz} = -n(z)$ Sec Z, where Z is the solar zenith angle.

Therefore, $n(z) = \frac{1}{\sigma \text{Sec } Z} \cdot \frac{1}{\phi} \frac{d\phi}{dz}$ (3)

The flat earth approximation results in an error of less than 1% for the Lithium Fluoride-nitric oxide chamber if $Z < 73^{\circ}$. The error is 10% at 85° and increases rapidly for larger zenith angles. In the case of a satellite sunrise-sunset experiment the zenith angle is greater than 90°, therefore by using the same approximation as the rocket flight this would lead to very large errors. In the following, even though the theory takes into account the "spherical" shape of the earth, the final result is still an approximation as no allowance has been made for the finite size of the sun.

The geometry for zenith angles greater than 90° is shown in Fig. 5.5. The ray from the sun to the satellite position at W passes a point of maximum particle density at O. Since most of the

absorption is occurring in the vicinity of O, the intensity at W ultimately leads to the number density at O.

In this case the satellite position is defined in terms of the minimum ray height h; which is given by

$$h = (R + z) \text{ Cos } (90 - Z) - R \qquad (4)$$

By integrating along the ray from the satellite to the sun one obtains the columnar density $n_T(h)$. If s is measured along the ray from 0 then,

$$n_T(h) = \int_0^\infty n \, ds + \int_0^W n \, ds \qquad (5)$$

To evaluate the integrals, it is necessary to specify the variation of n with height and the relationship between s, x and h.

$$n(x) = n(h) \exp (- x/H) \qquad (6)$$

where n(x) is the number density at a height (h + x),

n(h) is the number density at height h and

H is the scale height.

From Figure 5.5

$$s^2 = (R + h + x)^2 - (R + h)^2$$

or

$$s^2 = x(2R + 2h + x) \qquad (7)$$

Therefore

$$\int n \, ds = n(h) \int \frac{\exp(-x/H).(R + h + x)}{x^{\frac{1}{2}}(2R + 2h + 2x)^{\frac{1}{2}}} \, dx \qquad (8)$$

Since over the region of importance, R >> h or x, equation (8) can be simplified as,

$$\int n\,ds \approx n(h) \int \frac{\exp(-x/H)\,R}{(2Rx)^{\frac{1}{2}}}dx$$

$$= \left(\frac{R}{2}\right)^{\frac{1}{2}} n(h) \int \frac{\exp(-x/H)}{x^{\frac{1}{2}}}\,dx \qquad (9)$$

To evaluate equation (9) a change of variable will have to be made to convert the integrand to a standard form.

If $y^2 = x/H$, then, $dx = 2Hy\,dy$ and equation (9) becomes

$$\int n\,ds = (2RH)^{\frac{1}{2}}\, n(h) \int \exp(-y^2)\,dy$$

We are now in a position to evaluate equation (5)

$$n_T(h) = \int_0^{\infty} n\,ds + \int_0^{W} n\,ds$$

As $s \to \infty$, $x \to \infty$ and therefore $y \to \infty$

and as $s \to W$, $x \to (z - h)$ and therefore $y \to \left(\frac{z - h}{H}\right)^{\frac{1}{2}}$

Therefore

$$n_T(h) = (2RH)^{\frac{1}{2}}\, n(h) \left| \int_0^{\infty} \exp(-y^2)dy - \int_0^{(z - h/H)^{\frac{1}{2}}} \exp(-y^2)dy \right|$$

$$= (2RH)^{\frac{1}{2}}\, n(h) \left| \frac{\pi^{\frac{1}{2}}}{2} + \frac{\pi^{\frac{1}{2}}}{2} \operatorname{erf}\,(z - h/H)^{\frac{1}{2}} \right|$$

$$= \left| \frac{\pi RH}{2} \right|^{\frac{1}{2}} n(h) \left| 1 + \operatorname{erf}\,(z - h/H)^{\frac{1}{2}} \right| \qquad (10)$$

Now $(z - h/H)^{\frac{1}{2}}$ can be regarded as nearly independent on h and a large number so that $\operatorname{erf}(z - h/H)^{\frac{1}{2}}$ approximates to unity.

Therefore, equation (10) becomes

$$n_T(h) = (2\pi RH)^{\frac{1}{2}}\, n(h)$$

and

$$\frac{dn_T(h)}{dh} = (2\pi RH)^{\frac{1}{2}} \frac{dn(h)}{dh} \qquad (11)$$

Equation (2) can be written in terms of h instead of z,

as

$$\frac{1}{\phi}\frac{d\phi}{dh} = -\sigma\frac{dn_T}{dh}$$ and by substituting equation (11)

becomes

$$\frac{1}{\phi}\frac{d\phi}{dh} = -\sigma(2\pi RH)^{\frac{1}{2}}\frac{dn(h)}{dh} \qquad (12)$$

From equation (6), $\frac{dn(h)}{dh} = -n(h)/H$ (13)

and by substituting equation (13) into equation (12)

$$\frac{1}{\phi}\frac{d\phi}{dh} = \sigma\left(\frac{2\pi R}{H}\right)^{\frac{1}{2}} n(h)$$

Therefore, $n(h) = \frac{H^{\frac{1}{2}}}{\sigma(2\pi R)^{\frac{1}{2}}}\frac{1}{\phi}\frac{d\phi}{dH} = \frac{H^{\frac{1}{2}}}{\sigma\ 202.8}\cdot\frac{1}{\phi}\frac{d\phi}{dH}$ (14)

In equation (14), the radius of the earth was taken to be 6550 Km. Equation (14) was used in the method outlined in Section 5.4.1. for the determination of the preliminary results in Section 5.5.1.

5.4.1. METHOD OF ANALYSIS OF WRESAT RESULTS

The passes considered in this preliminary look at WRESAT data were those of Santiago 2, Alaska (Fairbanks) 16, and Johannesburg 42. In the terminology used above, the place names refer to the tracking station and the numbers refer to the orbit number past that station. These three passes were considered for the following reasons:

(a) All three passes were extremely "clean" passes i.e. very little noise on the records.

(b) They represent data taken from the beginning, near the middle and near the end of the satellite's transmission lifetime. By measuring solar flux, information was gained on the decay of the ion chambers throughout the satellite lifetime. Even though the ion chambers decayed due to deterioration of the filling gases, only one ion chamber decayed sufficiently to affect molecular oxygen measurements.

(c) The Santiago and Johannesburg passes were both from southern hemisphere stations of approximately the same latitude and a comparison could be made between these results and the Long Tom oxygen densities.

(d) The Alaska pass was a winter sunset pass, whereas the other two were summer sunrise so that a comparison could be made on seasonal variations in molecular oxygen densities.

The decoding of the signals from the satellite was performed by Weapons Research Establishment who provided the Physics Department, University of Adelaide, with computer printouts of detector signals at particular times during a pass. From this telemetry record and by using the calibration pulses the ion chamber responses were obtained as a function of time.

Figure 5.6 shows a typical calibration graph for an amplifier coupled to a lithium-fluoride ion chamber. As can be seen from this graph the voltage output from the amplifier is proportional to the logarithm of the current input. Below a current of 10^{-9} amps this proportionality no longer exists and hence currents less than 10^{-9} amps cannot be measured with this amplifier. The slope of the graph does not change with environmental conditions but the graph as a whole can move left or right with temperature variations. The calibration pulse could fix one point on the true calibration graph and hence the true graph could be plotted.

Nominally, a current of 1.28×10^{-7} amps was fed into the amplifier from a 1.28V battery during the calibration pulse for the lithium-fluoride-nitric oxide ion chamber. In this case, however, the grid of the electrometer valve in the amplifier was sitting on -0.39V so that allowance had to be made for this. The true calibration current was 1.67×10^{-7} amps.

For other ion chambers, with the more sensitive amplifier, a similar calibration graph was obtained but capable of measuring accurately currents of 10^{-11} amps. Nominally, the calibration pulse current for these chambers was 1.28×10^{-9} amps, but allowing for the grid voltage of -0.75V a true calibration current of 2.03×10^{-9} was supplied.

Because of the dependence of calibration current on the grid voltage care had to be taken on the selection of calibration pulses. When there was a signal on the ion chambers, the grid of the electrometer valve could be sitting on any voltage so that calibration pulses occurring when there was a signal had to be ignored. The remaining calibration pulses were averaged to define the true calibration graph for that particular pass. The computer programme for determining ion chamber currents from the voltage output relied on the original laboratory calibration graph rather than the new, in flight, calibration. The true current would be that current corresponding to the same voltage output i.e. from Fig. 5.6, Santiago 2, an original current of 1×10^{-8} amps would actually be a current of 5×10^{-9} amps.

From the satellite orbit data, the minimum ray height (h) was obtained as a function of time and hence the corrected ion chamber response could be plotted as a function of minimum ray height. The solar aspect sensor data varied little during a satellite pass so it was assumed that solar aspect was essentially constant. To determine molecular oxygen densities the absolute measurement of aspect was unnecessary however, the determination of aspect angle was essential for absolute solar flux measurements.

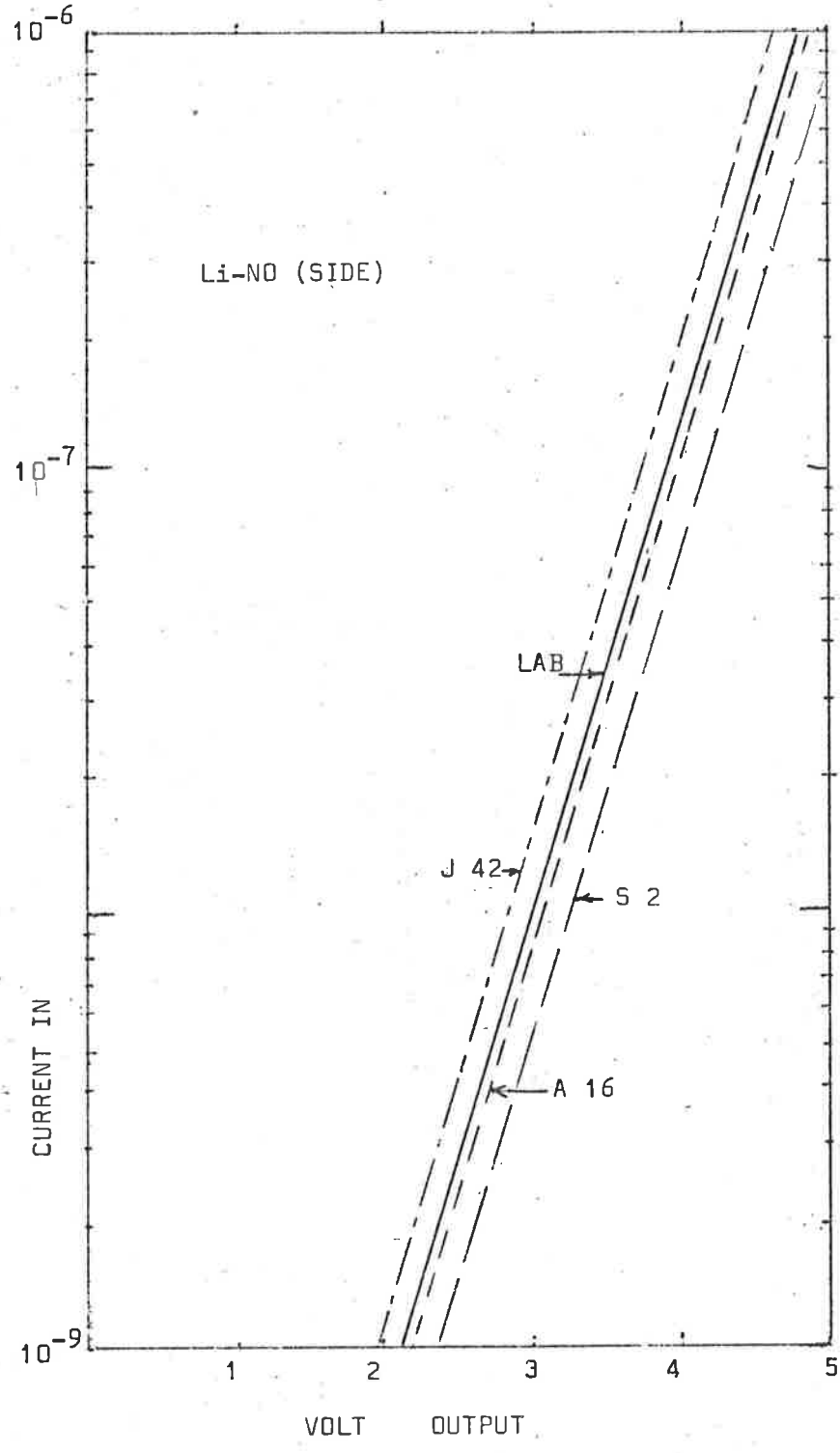

Fig. 5.6. Laboratory calibration of the logarithmic amplifier. Included in the diagram are the calibrations for the three WRESAT passes considered.

From the ion chamber current versus minimum ray height a plot of $\frac{1}{I}\frac{dI}{dh}$* versus minimum ray height could be obtained. (In this case dh = 2 Km.). Over the height range dh, it was assumed that the scale height H did not vary then;

if $\frac{1}{I(h)}\frac{dI(h)}{dh} \Big/ \frac{1}{I(h+dh)}\frac{dI(h+dh)}{dh} = R'$

then $R' = n(h)\left[H(h+dh)\right]^{\frac{1}{2}} / \left[H(h)\right]^{\frac{1}{2}} n(h+dh)$

where I(h) equals the ion chamber current at height h,

I(h + dh) equals the ion chamber current at height (h + dh), and

n(h) and n(h + dh) are the molecular oxygen densities at height h and (h + dh) respectively.

Now $n(h+dh) = n(h) \exp\left[-dh/H(h+dh)\right]$

Therefore,

$$R' = \exp\left[dh/H(h)\right]$$

and $\ln R' = dh/H$ and hence the scale height may be calculated for each height interval.

Once the scale height had been determined for each height interval, equation (14) section 5.3.1. could be used to determine the molecular oxygen density as a function of minimum ray height. The absorption cross-sections used were the same as used in the Long Tom rocket experiment. (See Table 4.1).

To obtain the best results the finite size of the sun must be considered. This involves the production of a theoretical

---

* As the ion chamber current (I) is directly proportional to the solar flux (ϕ) then $\frac{1}{I}\frac{dI}{dh} = \frac{1}{\phi}\frac{d\phi}{dh}$.

response curve for an assumed molecular oxygen profile. By an iteration procedure, the molecular oxygen profile can be obtained which gives a response curve agreeing with the data. For a preliminary look at the data the point sun method, being simple, was preferred even though some data points had to be discarded. (see Section 5.5.1.).

5.4.2. DETERMINATION OF ASPECT ANGLE

The aspect sensors flown in WRESAT were the same as flown in the rocket experiments. To determine the aspect angle for the detectors, the ratio of the signal from the flush teflon to the protruding teflon detectors had to be obtained.

The pair of aspect sensors in the forward detector banks performed satisfactorily for the transmitting lifetime of the satellite. As a ratio of two signals had to be obtained, this ratio was very sensitive to errors in determining the maximum value of the individual aspect sensor signals. As the aspect sensors were only sampled a limited number of times (see Fig. 5.4) and the estimated error for the telemetry system plus noise was ± 5%, care had to be taken in determining the maximum value of the aspect sensor signals. This was done by assuming that the aspect angle would not change during five consecutive passes across the sun and a composite curve of the aspect sensor response was drawn

for these five passes. By repeating this procedure for the complete satellite pass an average value was produced for the maximum value of the detectors. The ratio obtained in this way was then compared with laboratory calibrations and the aspect angle, for the forward experimental block was determined as between 0^{o} and 5^{o}. For the three satellite passes considered in this thesis the aspect angle determined was between these limits. This agreed with magnetometer data and theoretical predictions on the satellite motion. An aspect angle between these limits would not introduce significant errors in the determination of ion chamber response.

The side-facing aspect sensors did not perform satisfactorily as the flush teflon aspect sensor discontinued giving signals after pass eight. The reason for this breakdown is unknown but it possibly could be due to a dry joint in the connecting leads. On one of the passes considered, Santiago 2, the flush teflon sensor was still working and the same method of analysis was applied for this pass as with the forward detectors. For Santiago 2, an aspect angle of 17^{o} was determined. This figure for aspect was considered to be doubtful as there was no supporting evidence for it. As there was no magnetometer for the sideways experiment and the flush teflon aspect sensor ceased to function after pass eight then it may have been giving false signals before that pass. Santiago 2, being an early pass for the satellite was

still affected by aerodynamic heating caused by the launch. As the sensor was a phototransistor the signal given by the aspect sensor varied exponentially with temperature. The pair of photo-transistors used in a set of aspect sensors were matched as close as possible for their sensitivity and temperature response, but any slight mismatch could cause significant errors in the ratio of the two detectors.

To try and confirm this value of 17^{o} for aspect angle an analysis was carried out on the shape of the aspect sensor and the ion chamber response curve. From the laboratory calibrations for the aspect sensor curve for normal aspect, a family of normalized theoretical curves could be drawn, each curve corresponding to a different aspect angle, had a different shape. Theoretically a composite curve, normalized to the same value should lie on this family of curves and therefore limits could be placed on the aspect angle. Because of errors in the telemetry system and noise this procedure was not successful. All that could be gained from Santiago 2 aspect by this method was that the aspect was greater than 15^{o}.

The same procedure was tried with ion-chamber response curves instead of the aspect sensor curves, but this again proved unsuccessful as the theoretical ion chamber curve shape for different aspect angles was very insensitive to aspect angle change.

However, it was noted that the maximum signal received from the protruding teflon sensor remained practically constant for the three passes considered. This indicated that the sideways aspect angle for Santiago 2 was close to the aspect angle for the other passes. The other passes considered, Alaska 16, and Johannesburg 42 being later in the satellite's lifetime would not be affected by temperature as was Santiago 2 but the flush teflon aspect sensor was not operating. To overcome this difficulty use was made of the forward facing flush aspect sensor and the sideways facing protruding sensor, and using these as a pair. This could be done, as in the laboratory calibrations, to determine the level to which the individual sensors could be set, measurements were taken, in sunlight, for normal aspect of each individual sensor. The ratio of the laboratory reading, after allowing for differences in the circuit for the individual sensors gave a calibration point for which the ratio of these two sensors, could be determined for different aspect angles. The method of analysis was identical to that for the forward aspect sensors. Composite curves were drawn for five consecutive scans of the sun and the average value for the peaks of these curves were used to determine the ratio for the detectors and hence the aspect angle. For these passes an average aspect angle of 33^{o} was determined. As mentioned previously, the aspect angle does not affect molecular oxygen

density results if the aspect is constant but it does affect solar ultra violet flux values. For the purposes of this preliminary analysis a value of 33^{o} was taken for the aspect angle for all passes considered.

5.5.1. MOLECULAR OXYGEN DENSITY RESULTS

Figures 5.7 and 5.8 show the variation of ion chamber current plotted against minimum ray height for Santiago Pass 2. Figure 5.7, applies for the forward detectors and Figure 5.8 applies for the sideways facing detector bank. The vertical scale has been changed for each detector. As the errors in the data points were large it was decided to run the Santiago 2 tape through the computer twice. Each data point on these graphs was determined by plotting the ion-chamber response for both runs and determining the line of best fit for these points. The maximum value was then taken from the line of best fit. Even after these precautions it can be seen that there is considerable scatter in the data points. It can be also seen from these graphs that by choosing the lithium-fluoride nitric oxide, Sapphire-Xylene and Quartz-triethylamine chambers that the oxygen densities could be derived for a height range from 90 Km. to 190 Km. Either side of this height range densities can not be derived with any accuracy as dI/dh was extremely small.

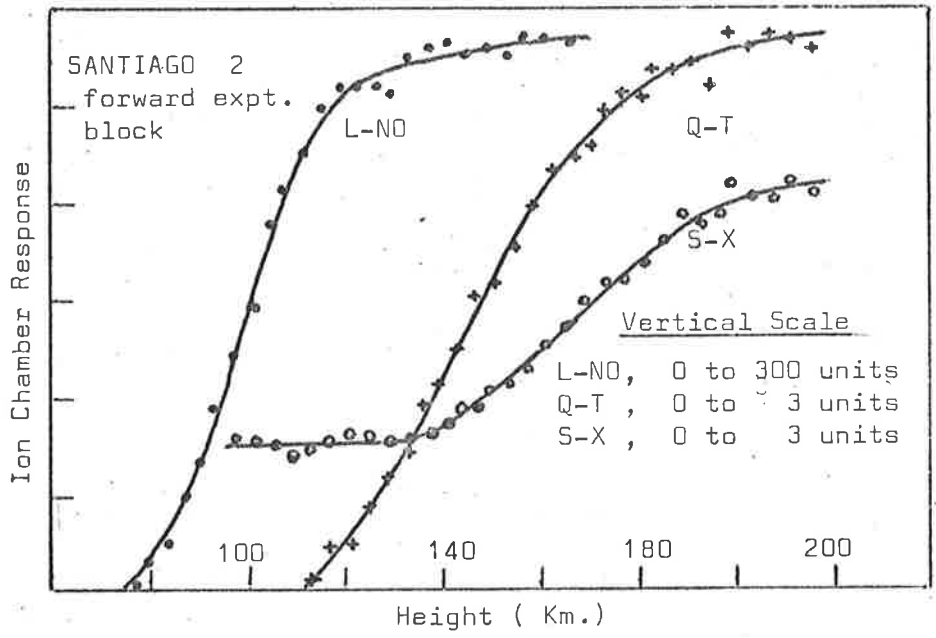

Fig. 5.7. The ion chamber current from each detector in the forward experiment block (Santiago pass 2) as a function of minimum ray height.

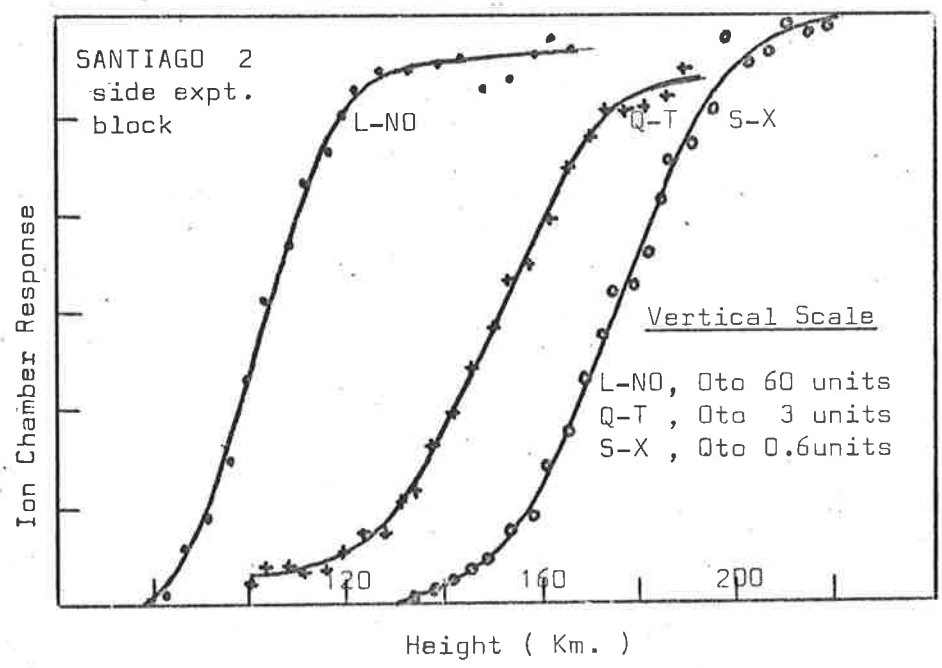

Fig. 5.8. The shapes of the measured atmospheric absorption curves from Santiago pass 2, sideways facing experiment block.

On the Sapphire-Xylene, forward facing detector, the base level was extremely high. This indicated that the ion chamber was not satisfactory and was slowly dying, due to the effect of ultraviolet radiation decaying the filling gas. The base level was due to leakage across the seal in the ion chamber and also to photo-electric effect from long ultra-violet wavelengths (up to 2300 $\mathring{A}$) on the central wire. For this reason this ion chamber had not been used for determining any oxygen densities. The maximum individual ion chamber currents for the two sets of graphs do not correspond, mainly due to aspect differences between the two banks. There was also a small contribution due to quantum efficiency differences, between any two chambers of the same type. Figure 5.9 shows the ion chamber current plotted against minimum ray height for the other passes considered: Alaska 16, and Johannesburg 42.

Figure 5.10 shows an example of the next stage of the analysis, i.e. a graph of $\frac{1}{I}\frac{dI}{dh}$ versus h, the minimum ray height. This graph was plotted from the data shown in Figure 5.8. Values of $\frac{1}{I}\frac{dI}{dh}$, as given by the line of best fit, were used to determine the scale height (H) for different values of minimum ray height. Similar graphs for each chamber analysed, had to be obtained for each pass.

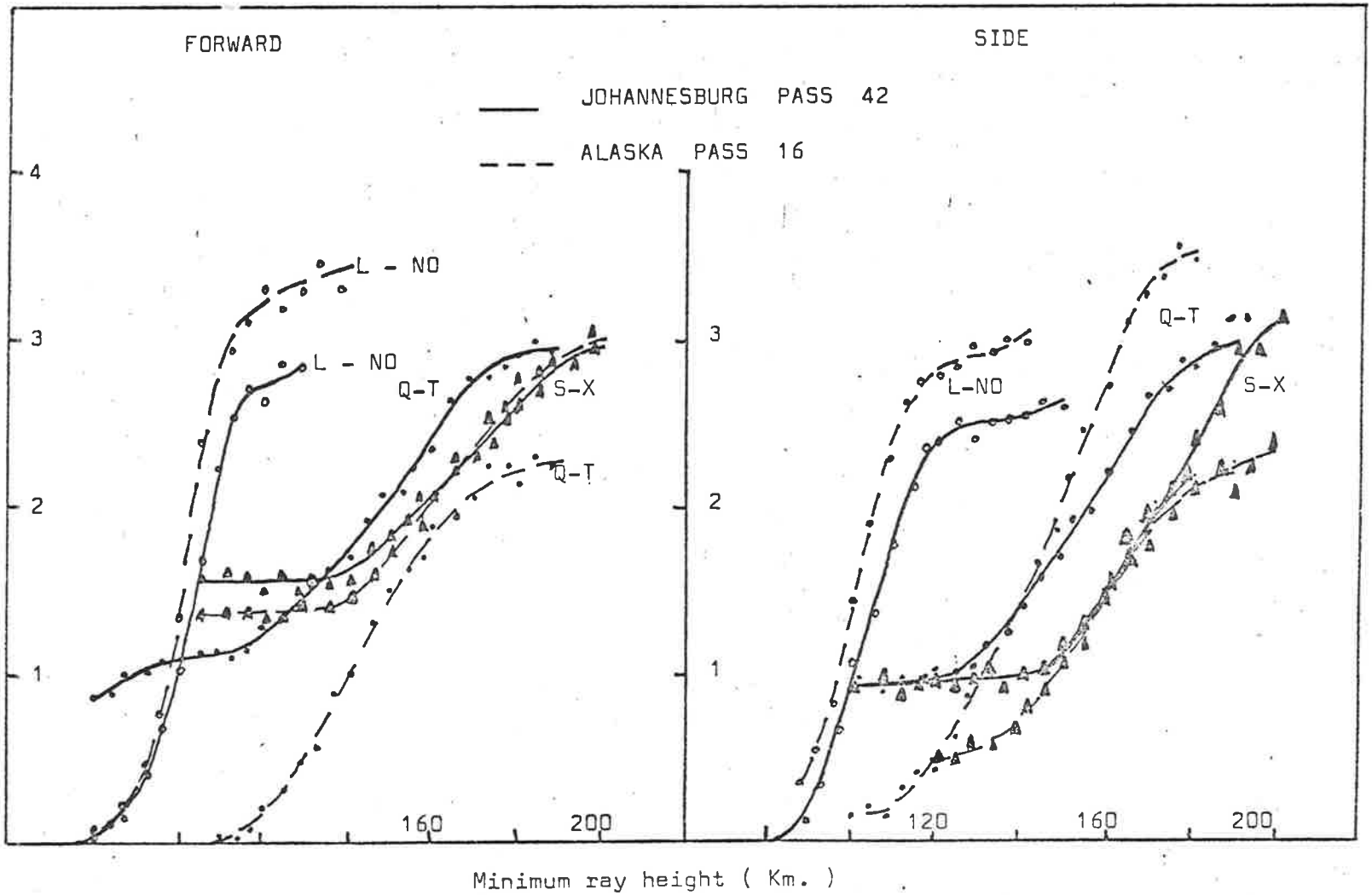

Fig. 5.9. The ion chamber current from each detector as a function of minimum ray height for two WRESAT satellite passes. There is no significance in the relative intensities shown for different detectors.

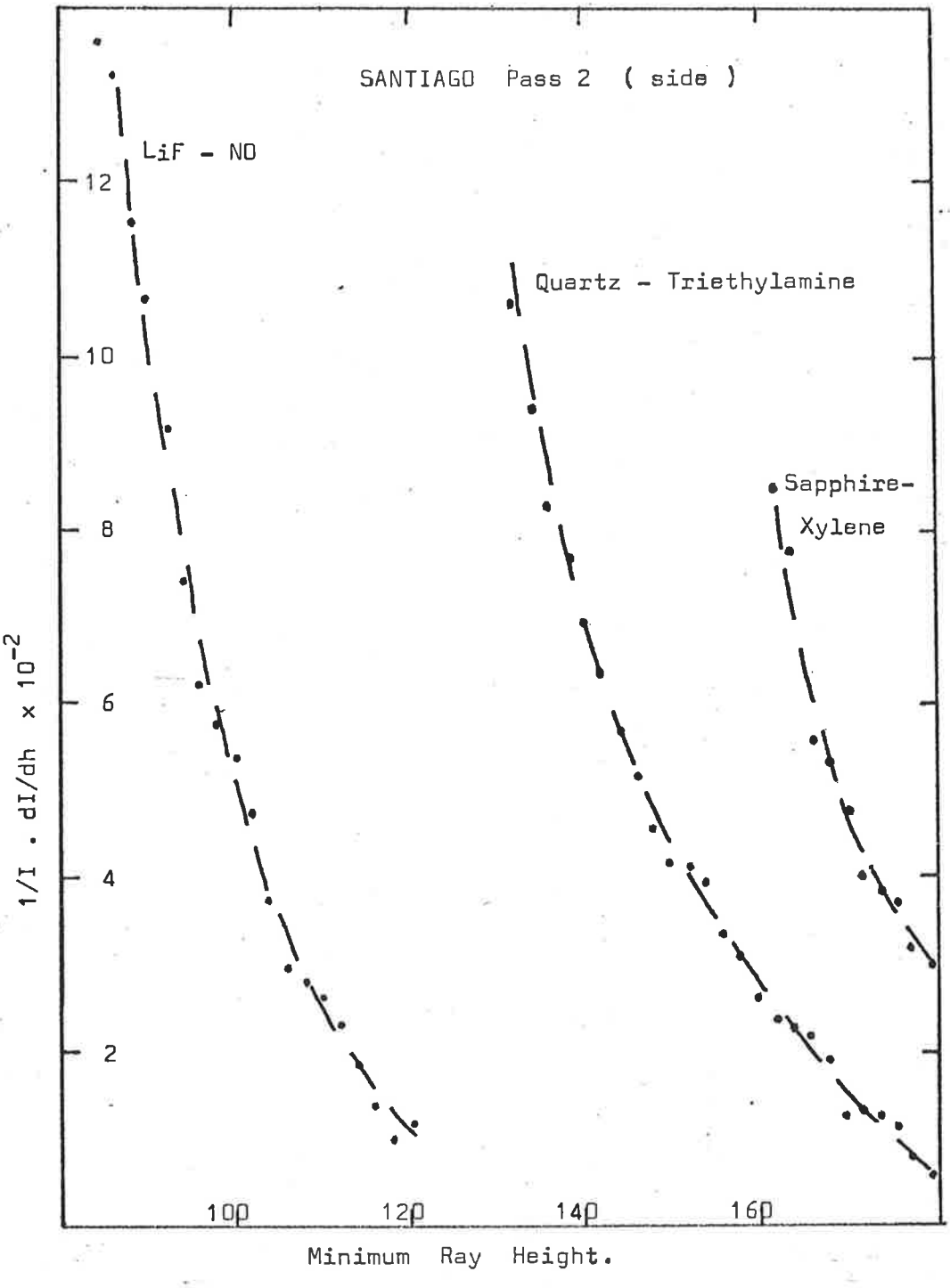

Fig. 5. 10. A plot of 1/I.dI/dh against minimum ray height for the sideways ion chambers from Santiago 2. These graphs enable the scale height to be determined.

Figure 5.11 shows the molecular oxygen density as measured by Santiago 2. There was good agreement between the two quartz-triethylamine chambers and the sideways sapphire-Xylene chamber. The line drawn was the line of best fit for the data points remembering that the vertical scale is logarithmic so that the higher points have a greater weighting than the lower. For each ion chamber the data points break away to the left from the line of best fit. This was a consequence of the method used in analysing the results.

For the analysis, it was assumed that the sun could be considered as a point source. In the height range which corresponds to the initial part of the ion chamber sunrise, the ion chamber is actually viewing a source of lower intensity than what is assumed with a point source. As a consequence the oxygen densities are lower than what they should be, hence the break away to the left. Another consequence of the assumption that the sun could be considered as a point source is that the oxygen densities derived from the lithium fluoride-nitric oxide chambers have very large errors associated with them. If rays are traced from the limbs of the sun to the satellite then, at the minimum ray height position, the difference between the minimum ray heights to each of these rays could be as much as 30 Km. If the scale height is much less than this difference then serious errors will exist in oxygen density results. This was the case

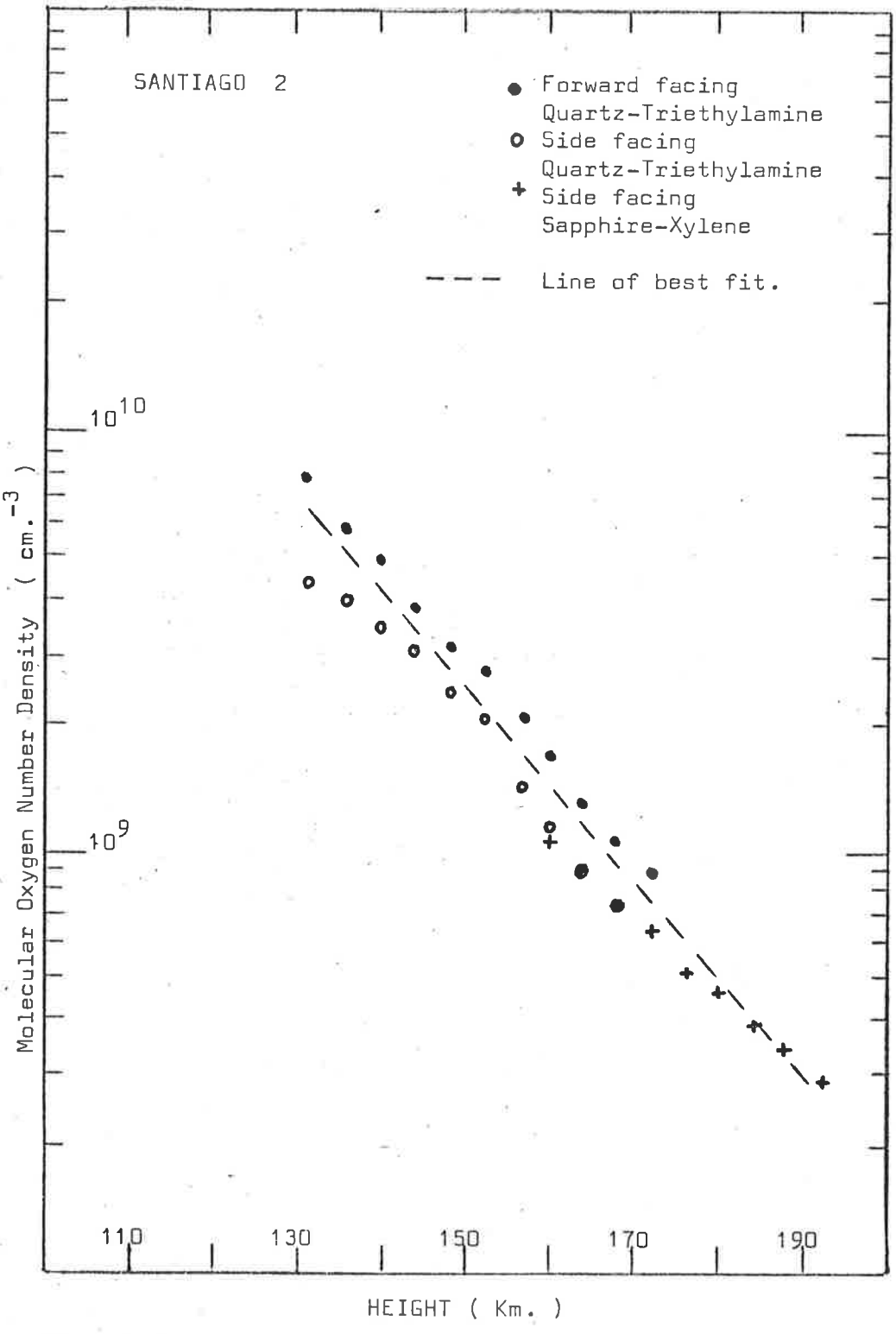

Fig. 5.11. The molecular oxygen density profile as a function of minimun ray height from Santiago pass 2.

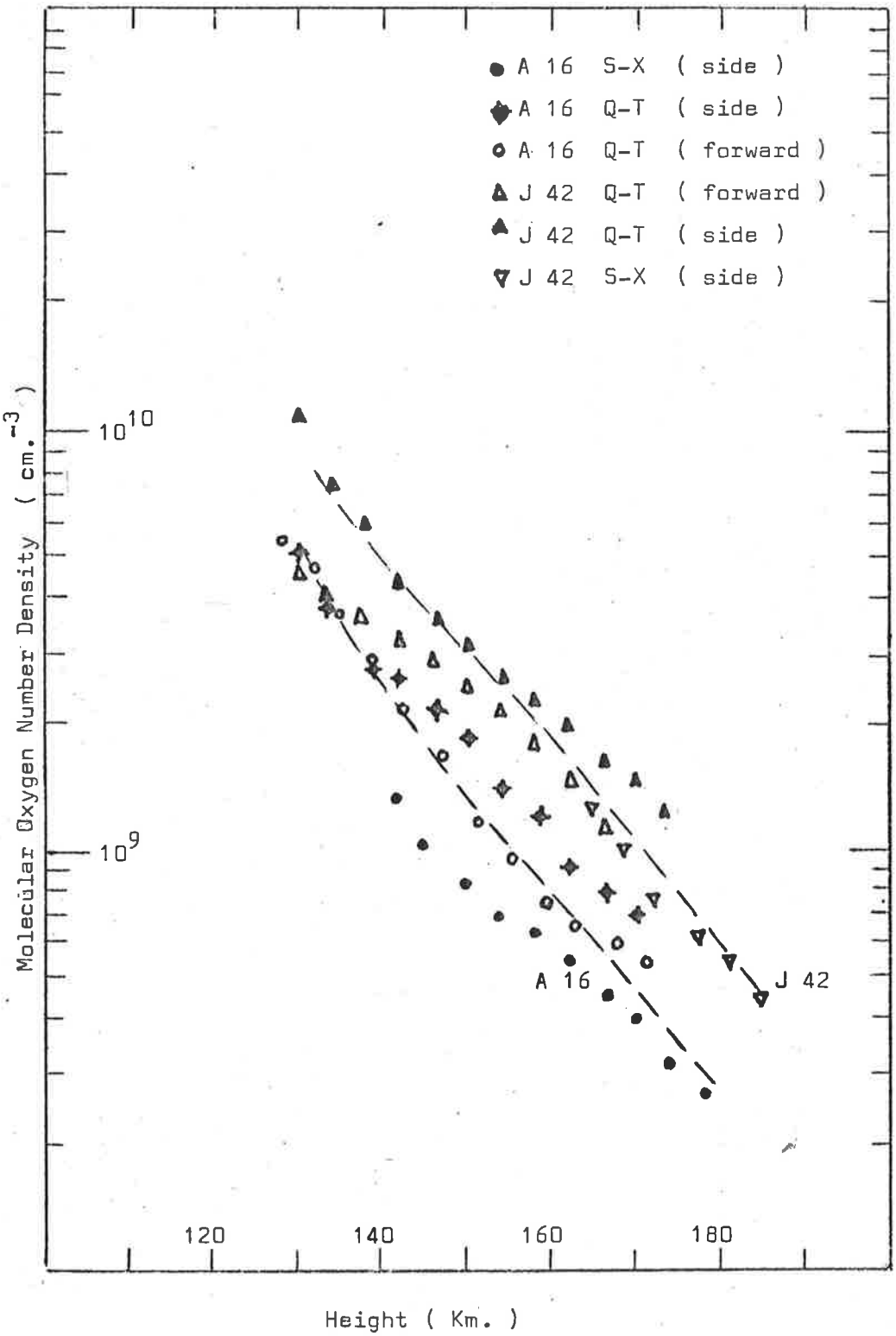

Fig. 5. 12. The molecular oxygen density profile as a function of minimum ray height from Alaska pass 16 and Johannesburg pass 42.

for the lithium fluoride-nitric oxide chamber which operates in a height range where the scale height could be as low as 6.5 Km.

For the other chambers, the scale heights are greater so that oxygen densities derived from these chambers are more accurate. Only the oxygen densities derived from the sapphire-xylene and quartz-triethylamine chambers have been shown on Figure 5.11. Figure 5.12 shows the oxygen densities obtained from the three passes considered. A comparison of these results with the Long Tom rocket flight and other workers in the field is included in Chapter six.

5.5.2. ULTRA-VIOLET SOLAR FLUX

The solar flux measurements were analysed in a similar manner to those of the Long Tom rocket flight. Figure 5.13 represents logarithm of the ion-chamber output versus the relative molecular oxygen mass above a certain height. The relative molecular oxygen mass has been given a value of unity for a height of 100 Km. for the lithium fluoride-nitric oxide chamber, 140 Km. for the quartz-triethylamine chamber and 160 Km. for the sapphire-xylene chamber. These graphs were then extrapolated to zero relative molecular oxygen mass to obtain an average value for the ion chamber current.

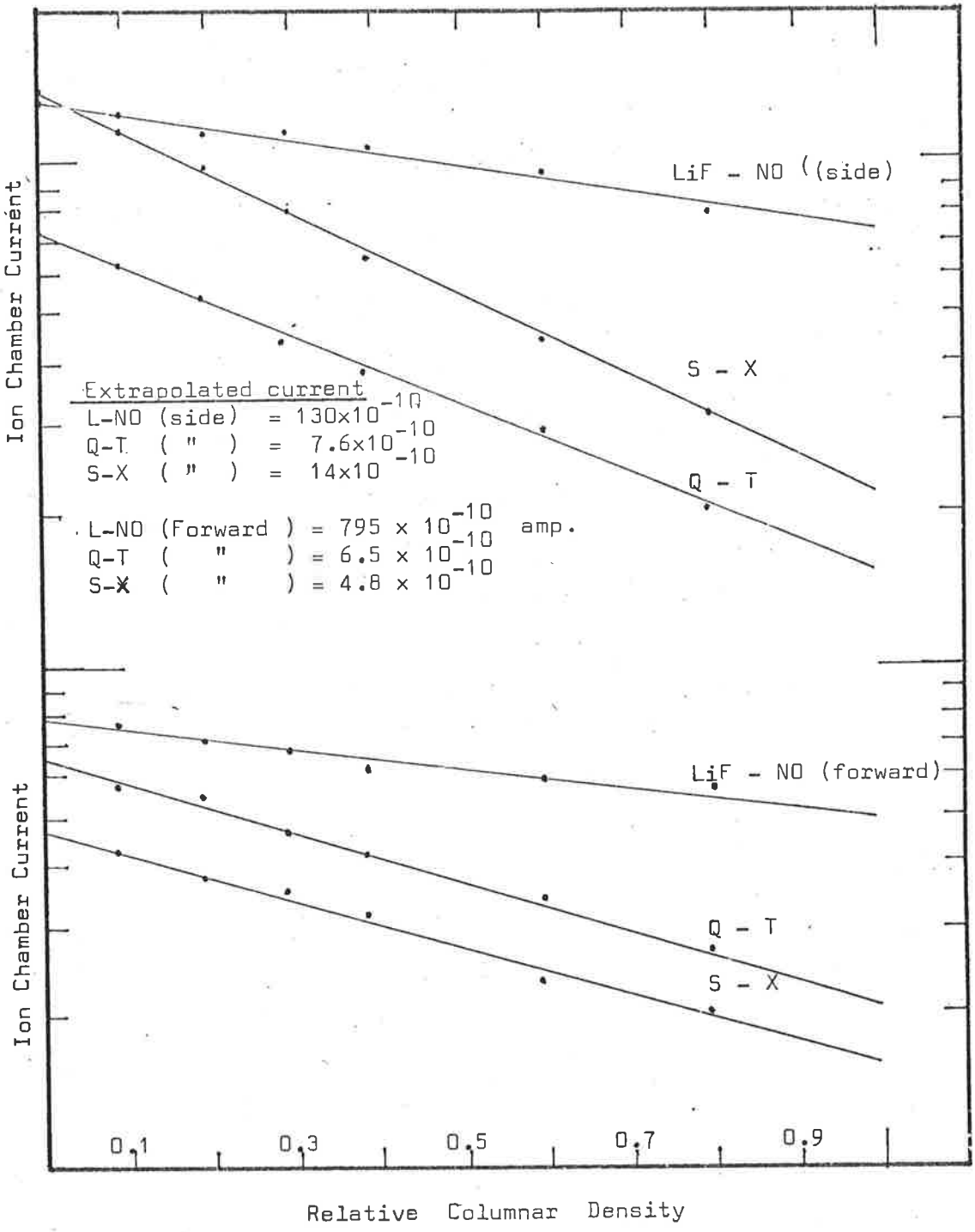

Fig. 5.13. The method of extrapolating the ion chamber current to its value above the earth's atmosphere. Only the Santiago 2 results are shown here; similar graphs were drawn for the other passes considered.

As the forward facing ion chambers had an aspect angle of effectively zero degrees an in flight calibration curve could be obtained for the angular response of the ion chambers. Figure 5.14 shows an in flight, normalized, composite angular response curve taken from the lithium fluoride-nitric oxide chamber in the forward bank of detectors. All chambers are of the same geometry, apart from slight differences in the width of the windows. This had only minor effects on the angular response. The aspect correction factor that had to be applied to convert the measured ion chamber currents to that for zero aspect is shown in Figure 5.14. No aspect correction was applied to the forward facing detectors but the sideways facing ion chamber currents had to be multiplied by 1.55. This aspect correction factor and the correction factor for the amplifiers (see section 5.4.1.) was applied to the values of ion chamber current from Figure 5.13 to imply the flux values as given in Table 5.1.

All fluxes listed in Table 5.1 are in erg $cm^{-2}cm^{-1}\mathring{A}^{-1}$ apart from those listed under the lithium fluoride-nitric oxide chambers which are fluxes for the Lyman α line alone and hence are in erg $cm^{-2}sec^{-1}$.

The three passes considered are at the beginning, middle and the end of the satellites lifetime. As can be seen from the fluxes only the forward facing lithium fluoride-nitric oxide and

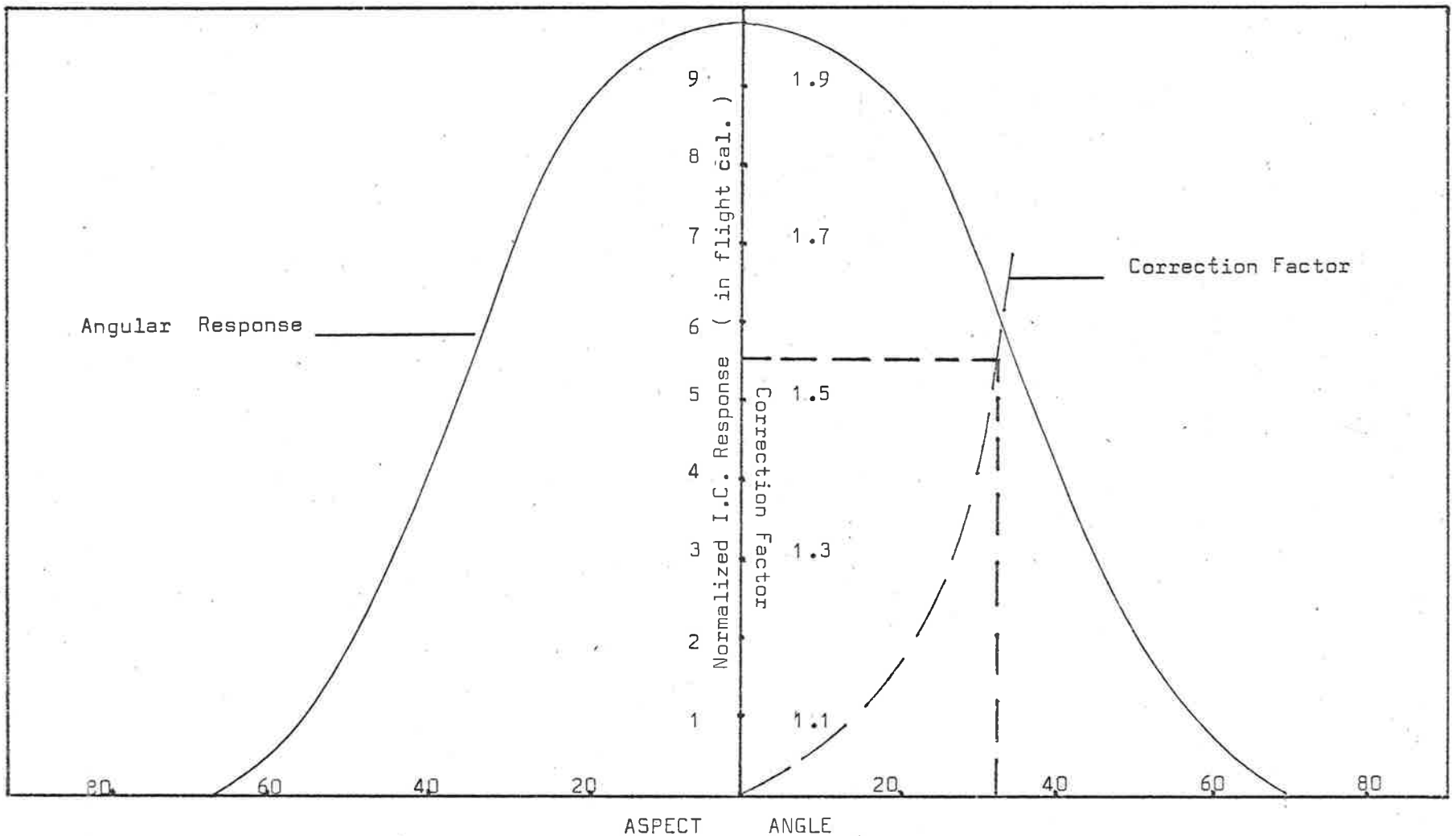

Fig. 5.14. An in flight angular response calibration curve for a LiF - NO ion chamber from the WRESAT satellite together with the correction factor necessary to convert ion chamber data to that for zero aspect.

TABLE 5.1

WRESAT ultra-violet fluxes from the three passes considered.

Li F NO (Lα) Forward	Li F NO (Lα) Side	S-X* Forward	S-X Side	Q-T Forward	Q-T Side
SANTIAGO 2					
5.0	4.7	5.4×10^{-3}	6.7×10^{-3}	3.7×10^{-2}	6.4×10^{-2}
ALASKA 16					
5.3	1.6	3.3×10^{-3}	3.4×10^{-3}	1.6×10^{-2}	4.3×10^{-2}
JOBURG 42					
4.8	1.0	1.8×10^{-3}	4.9×10^{-3}	4.1×10^{-3}	1.2×10^{-2}

sapphire-xylene sideways facing ion chambers did not deteriorate significantly during the lifetime of the satellite. The satellite was designed to have a short transmitting lifetime and no protection was placed in front of the ion chambers to limit the amount of ultra-violet radiation falling on them. Excessive radiation can break down the organic gases in the ion chambers. However, the deterioration in the sideways facing lithium fluoride-nitric oxide chamber was not expected and could

*From Fig. 5.6 this chamber appears to be suspect.

have been caused by a mechanical breakdown. This deterioration does not affect the determination of molecular oxygen densities unless the background leakage current becomes comparable with the ion chamber current.

The average fluxes taken from Santiago 2 and Alaska 16 for the quartz-triethylamine chambers and the sapphire-xylene chambers are 4 x 10^{-2} erg $cm^{-2}sec^{-1}\overset{o}{A}^{-1}$ and 4.7 x 10^{-3} erg $cm^{-2}sec^{-1}\overset{o}{A}^{-1}$. Ignoring the (small) contribution from emission lines the results indicate that from 1400 $\overset{o}{A}$ to 1600 $\overset{o}{A}$ the continuous flux corresponds to that of a black body at a temperature slightly greater than 4500^{o}K. These results are compared with the Long Tom data in Chapter six.

CHAPTER 6. DISCUSSION AND COMPARISON OF RESULTS

6.1.1 MEASUREMENTS OF MOLECULAR OXYGEN DENSITIES

The vertical distribution of molecular oxygen is fundamental to the description of the properties of the upper atmosphere. Evidence exists that molecular oxygen densities may vary significantly with seasons, latitude and longitude. Diurnal and day to day variations also occur particularly at altitudes higher than 100 Km. Molecular oxygen density measurements in the region 70 to 200 Km. fall into two main categories. First, measurements were made of the absorption of solar ultra-violet radiation with ion chambers, spectrographs and spectrometers. Second, mass spectrometer methods which are completely independent of a knowledge of the absorption cross-section but are difficult to calibrate. (Nier et al 1964, Mauersberger et al 1968) (See Section 6.1.3).

6.1.2 METHODS RELYING ON SOLAR ULTRA-VIOLET ABSORPTION

The first attempt to measure solar ultra-violet absorption in the atmosphere was made in 1949 (Friedman et al 1951). Two types of photon counter were used which responded to the ranges 1100 to 1300 $\overset{o}{A}$ and 1425 to 1625 $\overset{o}{A}$. No oxygen densities were determined as the counters which saturated had a long wavelength response making the analysis difficult. Similar experiments conducted in 1952 (Byram

et al 1953) were also unsuitable for determining oxygen densities. Later flights in 1953 (Byram et al 1955), 1955 and 1963 (Friedman et al 1964) contained a new counter responding to the wavelength 1425 to 1500 Å. This counter, which had a window of sapphire and a filling of nitric oxide, xylene and helium had a much lower long wavelength response than the previous counter sensitive to this range, so that oxygen densities were obtained. Densities in the height range 110 to 130 Km. were determined when the solar zenith angle was less than 60° and in the range 130 to 180 Km. when the zenith angle was close to 90 . Lithium fluoride-nitric oxide ion chambers were first used for absorption measurements in 1955 (Byram et al 1956) (Chubb et al 1958). The absorption of Lyman-α radiation was not used to determine molecular oxygen densities due to a misconception concerning the presence of water vapour ; their results indicated that the water vapour accounted for approximately half the absorption of Lyman-α radiation in the atmosphere. Kupperian and his colleagues had further flights in 1957 and 1958 (Kupperian et al 1959) using the Lyman-α ion chamber and a calcium fluoride-nitric oxide chamber responding to the range 1220 to 1340 Å. Oxygen densities were determined but the calcium fluoride-nitric oxide chamber analysis was complicated as the ion chamber responded to the "window" region for the absorption spectrum of oxygen (See Figure 2.2).

Ion chambers to measure the absorption of Lyman-α radiation have also been used by Smith and his colleagues. (Smith et al 1965,

Smith and Weeks 1965, Weeks and Smith 1968) to determine oxygen densities. Both ion chambers filled with nitric oxide and chambers filled with carbon disulphide were used on earlier flights but the latter showed an in-flight decrease in sensitivity due to a degradation of carbon disulphide from solar radiation. In a series of ten flights from 1964 to 1967 (Weeks and Smith 1968), other ion chambers apart from the lithium fluoride-nitric oxide were flown. They were magnesium fluoride-nitric oxide, calcium fluoride-nitric oxide, barium fluoride-xylene and sapphire-xylene ion chambers. Molecular oxygen densities were obtained for the height region 68 to 154 Km. by carrying out some measurements when the solar zenith angle was close to 90°. Most of the measurements were made at northern latitudes (between 38 and 40° N) but two were made in the southern hemisphere (44S and 32S) on 9th April, 1965 and 12th November, 1966. The results of these flights are shown on Figure 6.1 for comparison with the present work.

Very few rockets measurements of molecular oxygen densities by ion chambers have been made from the southern hemisphere. Apart from the two flights from Weeks and Smith, two flights carrying Lyman-α ion chambers have been made in 1963 and 1965 from Woomera (Carver et al 1964, 1965) determining densities in the height region 70 to 90 Km. Measurements from the Long Tom flight in 1966 which determined oxygen densities in the 70 to 120 Km. height region were the most detailed obtained to date as eight different types of ion

chamber were carried of which six were used to determine densities (See Table 4.1). In a series of three Skylark rocket flights from Woomera in March and November, 1967 and March, 1968, Wildman and his colleagues flew sapphire-xylene ion chambers (Wildman et al 1969). Measurements taken from these flights enabled oxygen density determinations to be made in the region 105 to 155 Km. The results of one of these flights together with Carver's 1963 and 1965 data are also displayed in Figure 6.1.

Ion chambers have been flown in satellites to determine oxygen densities by satellite sunrise-sunset experiments. Norton and Warnock (1968) have analysed Explorer 30 (SOLRAD 8) data from six winter (1966) and twenty-two summer (1967) passes over Boulder, U.S.A. telemetry station (40° N 105° W) ; in addition, six summer passes have been analysed from Ororal (36° S 149° E). Although there was some scatter on the data, preliminary results indicated that the density in winter was 1.5×10^{12} cm^{-3} compared with 2.3×10^{12} cm^{-3} for summer at 100 Km. Preliminary results from the British-American satellite Ariel 3, which included sapphire-xylene ion chambers indicated the possibility of longitudinal variations in the molecular oxygen density at 180 Km. (Stewart and Wildman, 1968, 1969). Further satellite measurements of the absorption of solar ultra-violet radiation should provide clearer information on the seasonal variations and indicate if there is a regular latitude and longitude variation.

Jursa et al (1959, 1963, 1965) have used normal incidence photographic spectrographs to measure the absorption of solar ultraviolet radiation in the atmosphere. The spectra produced which covered the wavelength range 500 to 2500 A, showed pronounced absorption by molecular oxygen in the form of the Schumann-Runge bands and continuum. The absorption was strong and easy to distinguish from the solar spectrum background, and the intensity changed noticeably from one spectrogram to the next with changing altitude. Oxygen densities were derived in the 60 to 100 Km. region from the variation with height of intensity in the Schumann-Runge bands. Above 100 Km., the Schumann-Runge absorption bands were too weak to provide useful information so that oxygen densities were obtained by measuring the change in photographic density of emission lines within the region 1000 to 2000 Å. The emission lines used were the C I line at 1657 Å and the C II line at 1335 Å which are wavelengths within the Schumann-Runge continuum. Spectra were taken in the laboratory with various path lengths of oxygen in front of the spectrograph to calibrate the instrument. In this way, the depths of the Schumann-Runge bands were determined as functions of the absorbing path length of oxygen. However, the major sources of error were in determining the "gamma" value for the film, which can vary from roll to roll and from one part to another of the same roll and accounting for scattered light which appeared as a background on the rocket

spectrograms. The results from this series of rocket flights are included in Figure 6.1.

Hinteregger and his colleagues have used the spectrometer described in Section 1.2.3. to measure the absorption of solar ultraviolet radiation in the atmosphere. The spectrometers were limited as they could only be operated above 120 Km., due to the effect of air on the open photomultiplier which responded only to wavelengths less than 1300 Å. Absorption analysis was carried out at the wavelengths of strong solar emission lines of which only the Si III line at 1207 Å is absorbed exclusively by molecular oxygen ; the others which occur at wavelengths below 1026 Å are absorbed by molecular nitrogen, molecular oxygen and atomic oxygen. Molecular oxygen densities can be derived directly from the 1207 Å measurements but absorption measurements from the other lines were combined to obtain molecular oxygen, molecular nitrogen and atomic oxygen density profiles. Hinteregger (1962) described the method used to obtain the density distributions and the results from two similar flights made in 1962 were given by Hall et al (1963b). The counting statistics and altitude resolution of the spectrometer was poor as the complete spectrum was scanned between 250 and 1300 Å which resulted in measurements being taken every 10 seconds.

Considerable improvement in this technique was achieved in 1963 by restricting the spectrometer so that observations were made on nine solar emission lines. These selected emission lines between

304 and 1207 Å were monitored in turn which resulted in an observation every 3 seconds and an improvement in the counting statistics by a factor of 3.5 (Hall et al 1965). The same improved spectrometer was flown on consecutive days in March, 1965, however, the main interest was to obtain molecular nitrogen and atomic oxygen densities in the region 180 to 240 Km. The molecular oxygen concentrations at the higher altitudes were too small for accurate determination of the vertical profile but the concentration at 150 Km. was measured and found to be 2.1×10^9, 2.7×10^9 and 2.4×10^9 cm^{-3} for March 2nd, 3rd and 4th respectively. These points from Hall et al (1967) together with the data from Hall et al 1965 are shown on Figure 6.1.

Of the three methods for determining oxygen densities by absorption of solar ultra-violet radiation, the spectrometers provide the most comprehensive information since molecular nitrogen, atomic oxygen and molecular oxygen can be determined. However, the instrument is limited to operation above 120 Km. and requires a pointing control. The photographic spectrograph which also requires a pointing control, is not limited with altitude but height resolution is poor as each exposure covers a height range of approximately 6 Km. The major disadvantage arises in the errors introduced (≈ 50%, Jursa et al 1963) with laboratory calibration of the film. The ion chambers have the advantage of not requiring a pointing control, being simple

to calibrate, and although they do not provide the comprehensive information supplied by spectrometers, the molecular oxygen density data is obtained with better height resolution than the other instruments.

6.1.3 MASS SPECTROMETER MEASUREMENTS OF MOLECULAR OXYGEN DENSITY

Nier et al (1964a, 1964b) reported on a rocket flight that had taken place at White Sands, New Mexico on 6th June, 1963, in which molecular nitrogen, molecular oxygen, atomic oxygen and argon were measured in the altitude region 100 to 200 Km. with a magnetic deflection mass spectrometer. The effect of contamination by gases given off by the rocket was minimized by sealing the ion source with a cap, which was cut off at approximately 100 Km. and pumping continuously with a sputter pump. A mass spectrum covering the range 10 to 50 A.M.U. was scanned every two seconds which resulted in molecular oxygen densities being determined from 100 to 200 Km. at 10 Km. intervals. Hedin et al (1964) made a more complete analysis of the data and obtained both atmospheric constituent number densities and temperature.

Nier and his colleagues (Kasprzak et al 1968) instrumented two Aerobee rockets flown on 30th November, 1966 (night) and 2nd December, 1966 (day) with the purpose of investigating day-night effects in the atmosphere. However, very little change was observed

in the molecular oxygen densities within the height range 120 to 220 Km. In the following year, the same group flew three rockets ; one in June, 1967 and two on 20th July (Krankowsky et al 1968). The July flights were a true day-night pair and substantial variations were found between the two (See Figure 6.2). As there was such a large variation between the day and night densities, it was suggested that day to day variations must be at least as large as day-night variations but in the opposite direction, as the 1966 flights gave practically identical results.

The mass spectrometer method for measuring molecular oxygen densities has advantages over the other methods discussed in 6.1.2 in that it does not require a pointing control, is completely independent of a knowledge of absorption cross-sections and can be operated at night. However, the main disadvantages are that mass spectrometers can only be operated above approximately 100 Km., are affected by contamination and orientation of the rocket and are very difficult to calibrate absolutely (Nier et al 1964a, Mauersberger et al 1968, von Zahn 1967). Errors in calibration occur as there are uncertainties with the relationship between the temperature of the molecules in the ion source and those in the surrounding air and the recombination of atomic oxygen. From Figure 6.1, it can be seen that in spite of these difficulties, the results obtained for molecular oxygen are in good agreement with those relying on ultra-violet absorption measurements.

6.2.1 DISCUSSION ON MOLECULAR OXYGEN DENSITIES

Figure 6.1 displays representative molecular oxygen density results taken from each of the techniques mentioned in 6.1.2. and 6.1.3. The histograms on the figure represent the present work for the Long Tom rocket flight and the preliminary results from three passes of WRESAT. The data points represented as circles, i.e. ●, o, ø, ⊙ are from the results of rocket flights made in the southern hemisphere so they are more directly comparable with the present results than the others. Also displayed on Figure 6.1 is the mean C.I.R.A. atmosphere 1965 with which most results agree up to 100 Km. Above this height the present results as well as the others disagree with the model atmosphere in that densities are lower by a factor of 2 to 3.

The Long Tom results below an altitude of 90 Km. depended on measurements made with a lithium fluoride-nitric oxide ion chamber, as were the other results shown, with the exception of Jursa et al (▼) , photographic spectrograph) and one flight of Weeks and Smith (o, ø) who used a magnesium fluoride-nitric oxide ion chamber. A variation of up to 15% higher than the mean C.I.R.A. atmosphere is indicated by the Long Tom results for molecular oxygen. In this height region the correction factor for aspect angle is in error by 10% (See 4.3.3) and together with the errors associated with the trajectory and the absorption cross-section (10%) indicate that the present results agree with the C.I.R.A. atmosphere within the experimental error. Weeks and Smith (1968) found variations the order of 20% at approximately

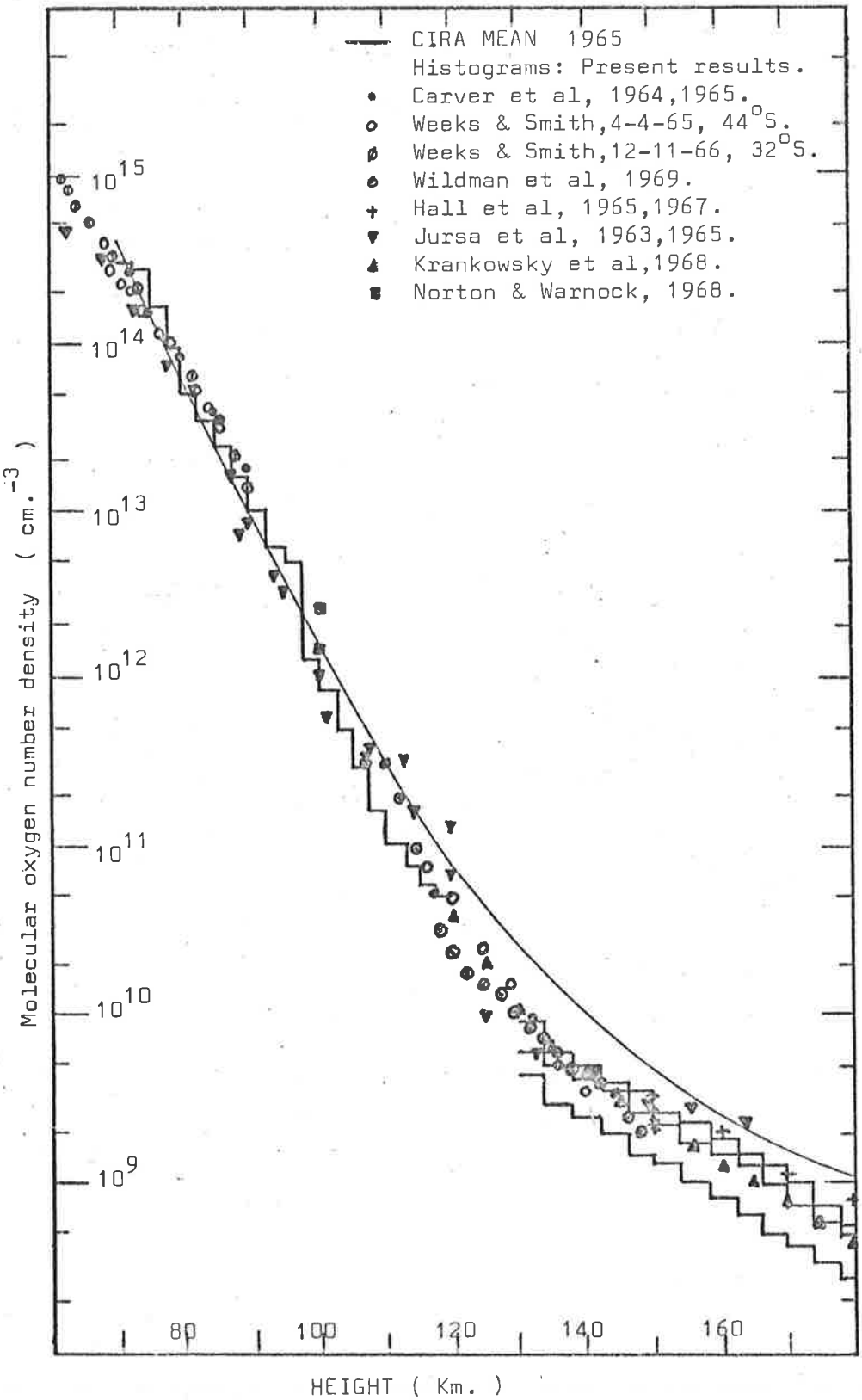

Fig.6.1. The molecular oxygen density profile determined by the present results and compared with others.

90 Km. in molecular oxygen density from two flights made in July, 1964 that were flown 65 minutes apart ; one at dawn and the other in the morning. It has been suggested that the variation is diurnal and as the variation can be 20% and greater, in this height region, the agreement between the results indicated on Figure 6.1 is remarkable.

In the region 90 to 120 Km. the Long Tom results have been derived from independent measurements from eight ion chambers of five different types (See Table 4.1). These results indicate that the molecular oxygen densities are significantly lower than those predicted by the mean C.I.R.A. atmosphere ; at 120 Km. the present results are lower by a factor of 2. The errors associated with aspect angle are lower than those for the 70 to 90 Km. region as the correction factor was less than 1.15 compared with 1.41 for the 80 to 90 Km. region. However, the main error for the data in this region is in the absorption cross-section as effective absorption cross-sections were used in contrast to the value at 1215 A (Hydrogen Lyman-α) used for the lithium fluoride-nitric oxide ion chamber. (See Table 4.1). The probable errors introduced in using effective absorption cross-sections has been estimated by Carver (1969) as ±15%. Errors associated with the absolute calibration do not enter the calculation as absolutely calibrated ion chambers are not required to determine molecular oxygen densities. The method of analysis of trajectory data is sensitive enough to indicate an apogee height error of greater than 0.1 Km. so that the probable error in the trajectory is no

greater than 0.1 Km.

The results from Wildman et al (1969, o) and Weeks and Smith (1968, o) agree with the Long Tom data in the region near 120 Km. although they have reported difficulties with the window of sapphire-xylene ion chambers outgassing making the ascent and descent phase of their results slightly different. No such effect was noticed with the Long Tom sapphire-xylene ion chamber measurements but possibly this could be accounted for by the differences in the launch vehicles ; the Long Tom rocket being subject to greater aerodynamic heating than the Skylark found flown by Wildman et al.

For altitudes above 120 Km., the histograms representing the average results from three WRESAT passes have been reproduced in Figure 6.2. These have been displayed together with the mass spectrometer results from Krankowsky et al (1968) and Kasprzak et al (1968) for flights in December, 1966 and July, 1967. As the Santiago 2 and Johannesberg 42 pass results were obtained during summer at sunrise for the satellite, where the latitude of the minimum ray height position was almost identical (See Figure 5.2), the agreement between the results to within the estimated errors for the experiment and data analysis (±30%) was to be expected. These results disagree with the mean C.I.R.A. atmosphere in that the molecular oxygen density is a factor of two to three lower throughout the height region 130 to 190 Km. The Alaska 16 pass was a winter, sunset pass and as can be

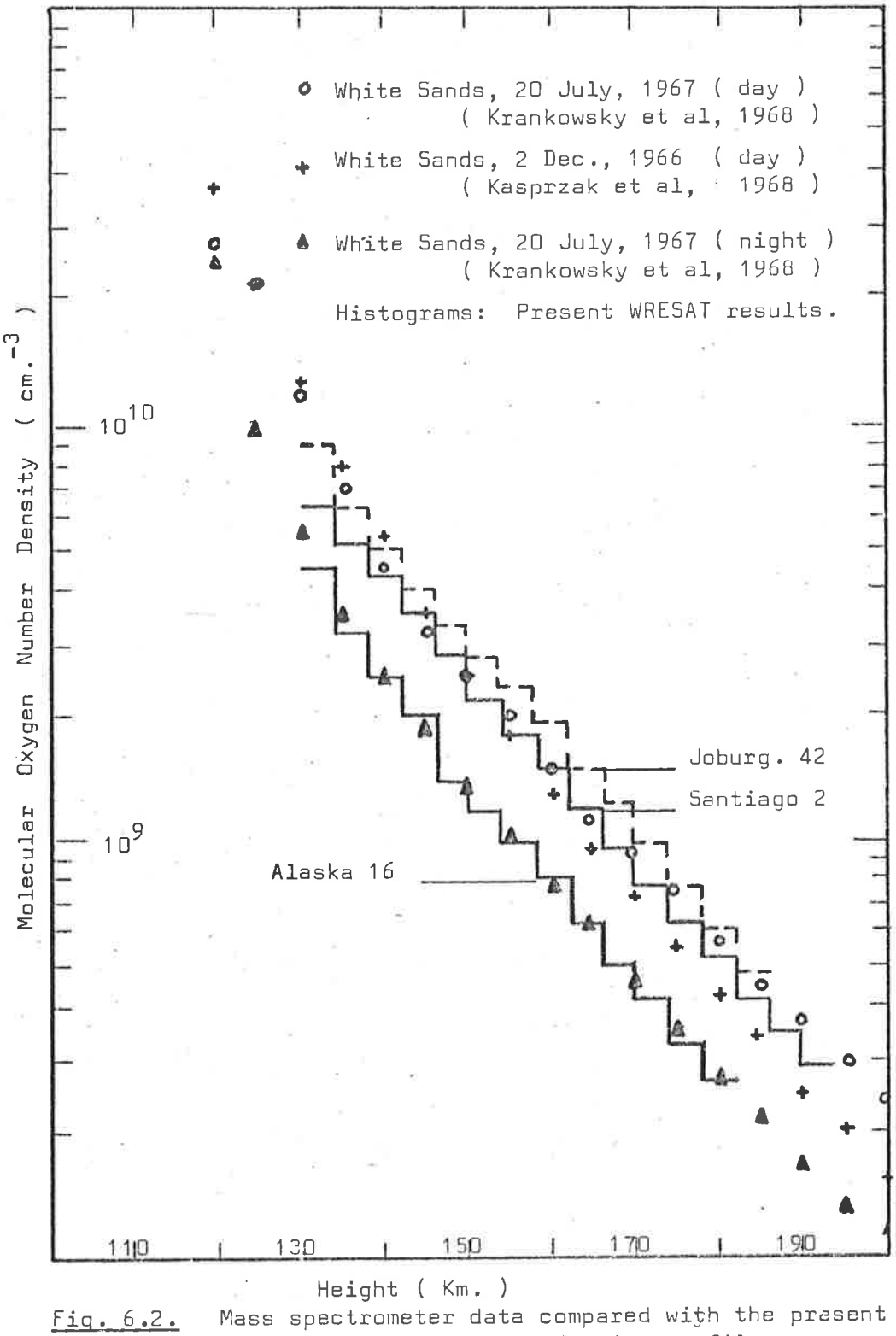

Fig. 6.2. Mass spectrometer data compared with the present WRESAT molecular oxygen density profiles.

seen from Figure 5.12, considerable scatter was evident in the measured values of molecular oxygen density. However, the present results indicate that the molecular oxygen densities appear to be lower than the summer passes in the 130 to 190 Km. region in agreement with the summer-winter dayflights of Krankowsky et al and Kasprzak et al (1968). The differences between Alaska 16 and the other passes from WRESAT, which could be attributed to seasonal and latitudinal variations as well as experimental errors have the same magnitude as the day-night variation measured by Krankowsky et al over White Sands in July, 1967. Results from two flights by Kasprzak et al (1968) indicated that day to day variations were also as large as the day-night variations. Even though the absolute magnitude of the molecular oxygen densities derived from mass spectrometer measurements may be in error due to uncertainties in calibration, the relative densities between any two flights should be accurate. Some evidence on seasonal variations can be inferred by comparing these measurements but the amount of data available is hardly sufficient to separate these effects from day-night and day to day variations. Further analysis of satellite data from WRESAT and Ariel 3 will be particularly important in specifying the variations of the densities from their average values.

6.2.2 DISCUSSION ON ATOMIC OXYGEN RESULTS

Measurements of atomic oxygen densities in the atmosphere have previously been attempted by using mass spectrometers (Nier and

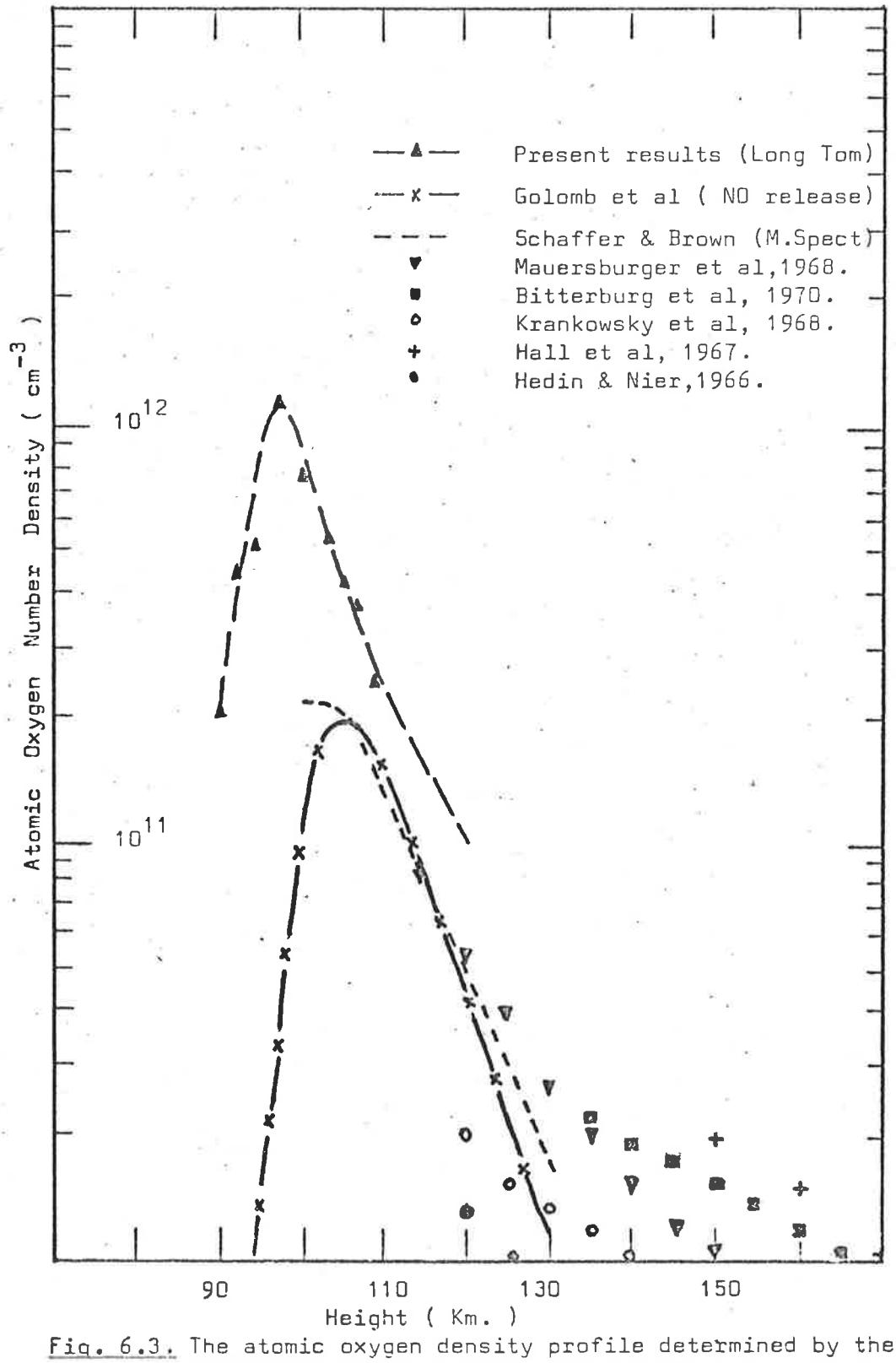

Fig. 6.3. The atomic oxygen density profile determined by the present results and compared with others.

his colleagues, Mauersberger et al), photoelectric spectrometers (Hall et al) and by nitric oxide release* (Golomb et al 1965). Examples of the determination of atomic oxygen densities are presented in Figure 6.3 together with the present Long Tom results. The agreement between the atomic oxygen curve derived from nitric oxide release and the mass spectrometer measurements is partly due to normalization to mass spectrometer measurements at 120 Km.

The present atomic oxygen concentrations were derived by assuming that within the height range 90 to 110 Km., there was no significant diffusive separation of the atmospheric species and hence the sum of molecular and atomic oxygen was equal to the fraction of oxygen in the air (21%) multiplied by the total atmospheric density (n_t) :

$$2n_O + n_{O_2} = 0.21n_t \qquad \ldots\ldots (1)$$

Measurements made with the Geiger counter included in the Long Tom flight gave total densities which were not significantly different from the U.S. Standard Atmosphere 1962 (See Figure 4.7). The molecular oxygen densities provided by ion chamber measurements enable equation (1) to be evaluated for atomic oxygen density throughout the height range. The assumption that there was no diffusive separation of

---

*The nitric oxide release technique relies upon releasing nitric oxide at night and detecting with photographic and photometric equipment on the ground, the radiation given off by the reaction ;

$$NO + O \rightarrow NO_2 + h^f$$

the atmospheric species from sea-level to the altitude of interest becomes increasingly erroneous at higher altitudes. However, in the range 90 to 100 Km., it may still hold and the data shows a distinct maximum at 100 Km. The absolute magnitude of the atomic oxygen density at 100 Km. is a factor of five higher than other measurements, however, it should be pointed out that even though calibrated detectors are not required, the peak value for atomic oxygen is extremely sensitive to errors in the total and molecular oxygen densities. The peak value of atomic oxygen, even with a probable error of 40%, indicates that dissociation of molecular oxygen becomes important above 100 Km.

The photo-electric spectrometer measurements shown on Figure 6.3 (Hall et al 1967) were obtained by measuring the intensity of solar ultra-violet emission lines of wavelength less than 1000 A. An identical technique was used as described previously (Section 6.1.2) which gave atomic oxygen densities larger than those determined by mass spectrometer measurements above 150 Km.

Mass spectrometer measurements of atomic oxygen have always been considered as minimum values as no laboratory calibration has been made for the instrument with this gas. Theoretical calibrations have been used for atomic oxygen but considerable uncertainties exist in estimating interactions between oxygen atoms at the ion source wall and hot filaments. The existance of loss processes seems to be established beyond doubt and it has been pointed out by von Zahn (1967) that greater

than 80% of the ion current observed stem from collisions with the ion source walls. The existance of a mass 44 peak (either N_2O or CO_2) has been attributed by von Zahn as being mainly formed by atomic oxygen recombining. Von Zahn has also pointed out in his review that the measured argon abundances imply a ratio of $n(O)/n(O_2)$ of about 4 at 120 Km. whereas mass spectrometers have measured this ratio as approximately 1. The present results indicate a value for this ratio of approximately 2 although it must be remembered that the basic assumption for the present method may be in error at this altitude. However, as the present technique is simple and does not require calibrated detectors, it could be used as a method for calibrating a mass spectrometer for atomic oxygen at altitudes less than 110 Km.

6.2.3 DISCUSSION ON SOLAR FLUX RESULTS

The Long Tom ion chamber data has been used to determine absolute solar ultra-violet fluxes in terms of the laboratory calibrations of each of the ion chambers. The barium fluoride-toluene and sapphire-xylene ion chambers did not reach saturation currents at the maximum rocket altitude of 121 Km. so that measurements were extended to zero optical depth by assuming that the observed molecular oxygen density curve could be extended to higher altitudes with constant scale height and plotting ion chamber response against relative air mass. These flux measurements are reproduced in Figure 6.4 together with WRESAT

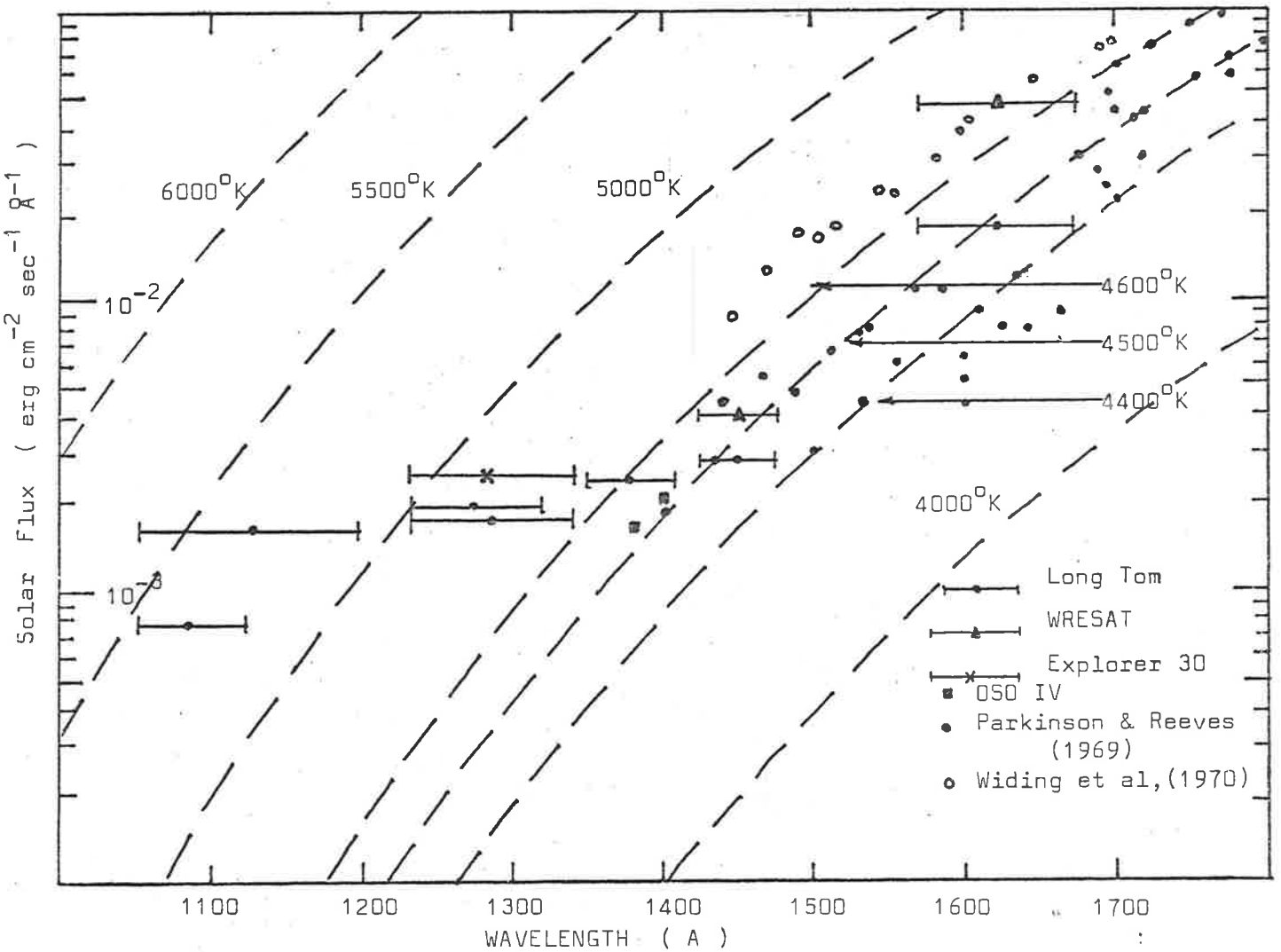

Fig. 6.4. Solar ultra-violet intensity distribution according to present ion chamber measurements. Included for comparison are the results from other workers and black body curves.

flux measurements, spectrographic measurements of Widing et al (1969) and spectrometric measurements (Parkinson and Reeves 1969). Included in the figure are curves which represent values for the equivalent black body temperatures of the sun. The present results indicate that the radiation temperature of the sun decreases from 5300°K at 1100 Å to a broad temperature minimum in the region 1400 to 1600 Å where the black body temperature is 4500 ±50°K. This temperature represents the solar temperature minimum between the upper photosphere and the low chromosphere and is of interest for the theory of the solar atmosphere. Gingerich and Rich (1968) theoretically predicted that the spectral range 1500 to 1700 Å would most clearly show the characteristics of the solar temperature minimum. As pointed out in Chapter One, the temperature minimum can be inferred not only from measurements made in the ultra-violet spectrum but also in the infra-red. Recent measurements in the infra-red region of the spectrum between 238 and 312 μ yielded a radiation temperature of 4370 ±260 Å, which agreed with the Long Tom results, (Eddy et al 1970, reported by Widing et al 1970). Widing et al's measurements indicate a temperature minimum of 4670 ±100°K and Parkinson and Reeves (1969) measured a value of 4400°K. No error limits have been stated for Parkinson and Reeve's measurement so that this value is possibly in agreement with the present result, however, the spectrographic measurement of 4670 ±100°K is inconsistent with the Long Tom data. The solar temperature

measurement is a poor indication of the absolute intensity of solar ultra-violet fluxes as an error of 40% in intensity corresponds to an error in the solar temperature of only 100°K. The present ion chamber measurement of 4500 ±50°K is more accurate than the spectrographic measurement, but due to a wide wavelength response is not as detailed. Only the errors associated with the absolute calibration system (approximately 10%) affect the absolute intensity measurements from ion chambers ; an extra 10% error has been allowed, for estimating the solar temperature minimum from Figure 6.4.

The preliminary WRESAT fluxes, shown in Figure 6.4., are higher than the Long Tom data but still indicate a solar temperature of approximately 4500°K. The measured Lyman-α flux (not shown on Figure 6.4) was also higher for WRESAT than for the Long Tom data. An average value of 5.0 erg cm^{-2} sec^{-1} was determined from the forward facing lithium fluoride-nitric oxide in WRESAT, whereas, the Long Tom flight gave a value of 4.2 erg cm^{-2} sec^{-1}. However, these values and the Explorer 30 value of 4.25 erg cm^{-2} sec^{-1}, taken at the same time as the Long Tom flight fall well within the limits suggested by Weeks (1967) for variations in Lyman-α intensity during the eleven year solar cycle : for the maximum of the cycle (1958, 1969) the mean value is 6.1 ±0.45 while for the minimum, the mean value is 4.3 ±0.35 erg cm^{-2} sec^{-1}.

6.3.1 CONCLUSIONS

The ion chamber method has been established for many years as a reliable method for determining molecular oxygen densities in the 70 to 180 Km. region. Results obtained indicate that there is good agreement between concentrations determined from ion chambers and by other techniques. Below 100 Km. the molecular oxygen concentration agree fairly well with those suggested by the mean C.I.R.A. model atmosphere 1965. However, at altitudes above 100 Km. measurements indicate the average molecular oxygen concentrations are a factor of 2 to 3 below that given by the mean C.I.R.A. model. The region of the atmosphere above 120 Km. appears most prone to significant change caused by diurnal, day to day, seasonal and possibly latitude and longitudinal variations. Very few rocket flights have been made to determine the magnitude of the variations in this height region but mass spectrometer measurements indicate that day to day and day-night variations may be as large as any seasonal and latitude variation. Clearly more detailed analysis from satellite borne detectors such as those carried by WRESAT or Ariel 3 which will give information in this region of the atmosphere, is required to help understand the magnitude of these variations from their average values. Unfortunately, ion chambers which provide information in this region suffer deterioration of the filling gases from prolonged exposure to ultra-violet radiation. Extreme limitation of the ion chamber window, together with highly sensitive amplifiers are

required in satellites to enable ion chambers to last a full year and separate seasonal from latitude or hemispherical variations.

Atomic oxygen, being a reactive gas, is very difficult to measure by mass spectrometers. Uncertainties in calibration of the instrument for atomic oxygen have lead to an under-estimation of the density above 90 Km. The present results indicate that atomic oxygen losses in mass spectrometers could be as high as 80%, however, a direct comparison between Long Tom data and other measurements is difficult as they have been taken in different localities at different times. A large proportion of the discrepency between the present results and other experimenters' may be due to experimental error, seasonal, latitudinal, day to day or day-night variations. The present technique of using a geiger tube and ion chamber to measure total and molecular oxygen densities and hence atomic oxygen, may be a satisfactory method of providing a calibration point between 90 and 110 Km. for mass spectrometers.

The problem of the solar temperature minimum between the photosphere and the low chromosphere is of interest for the theory of the solar atmosphere. However, the latest spectrometric results which indicate a temperature of 4400^{o}K and spectrographic measurements indicating 4670 ±100^{o}K are inconsistant as the temperature is not a good indication of the absolute intensities in the solar spectrum ; an error in the absolute intensity of 40%, only corresponds to a 100^{o}K uncertainty

in the temperature at 1650 Å. Solar flux measurements from ion chambers are more accurate than the spectrographic technique as they are simple to calibrate but measure an integrated flux over a wide bandpass. The quartz-triethylamine ion chamber, which has been flown successfully for the first time in the present work, together with the sapphire-xylene ion chamber indicate a solar temperature minimum of 4500 ±50°K. A more detailed analysis from WRESAT passes and further rocket flights carrying both sapphire-xylene and quartz-triethylamine ion chambers will be particularly important in specifying this parameter.

APPENDIX

This following paper has been written on the work described in this thesis.

"Solar Absorption Photometry and the Determination of Atmospheric Composition",
J. H. Carver, P. J. Edwards, P. L.Gough, A. G. Gregory, B. Rofe, and S. G. Johnson, Journal of Atmospheric and Terrestrial Physics, 1969, Vol. 31, pp. 563 to 570.

REFERENCES

Aboud, A., Behring, W.E. and Rense, W.A., 1959, Astrophys. J., 130, 381.

Aiken, A.C., Kane, J.A., and Troim, J., 1964, J. Geophys. Res., 69, 4621.

Allen, C.W., 1965, Space Sc. Rev., 4, 91.

Bates, D.R., and Nicolet M., 1950, J. Geophys. Res., 55, 301.

Bates, D.R., and Witherspoon, A.E., 1952, Mon. Nat. R. Astr. Soc., 112, 101.

Braun, W.A., Johnson, F.S., Oberly, J.J., Rockwood, C.C., Strain, C.V., and Tousey, R., 1946, Phys. Rev., 70, 781.

Bitterberg, W., Bruchhausen, K., Offermann, D., and von Zahn, U., 1970, J. Geophys. Res., 75, (28).

Blake, A.J., Carver, J.H., and Haddad, G.N., 1966, J. Quant. Spec. Rad. Tranf., 6, 451.

Burton, W.M., and Wilson, R., 1965, Nature, Lond., 207, 61.

Byram, E.T., Chubb, T.A., Friedman, H., and Gailar, N., 1953, Phys. Rev., 91, 1278.

Byram, E.T., Chubb, T.A., Friedman, H., 1955, Phys. Rev., 98, 1594.

Byram, E.T., Chubb, T.A., Friedman, H., and Kupperian, J.E., 1956, Astrophys. J., 124, 480.

Byram, E.T., Chubb, T.A., Friedman, H., Kupperian, J.E., and Kreplin, R.W., 1958, Astrophys. J., 128, 738.

Carver, J.H., 1969, Annals of the IQSY, Vol. 6, Paper 16.

Carver, J.H., Mitchell, P., Murray, E.L., and Hunt, B.G., 1964, J. Geophys. Res., 69, 3755.

Carver, J.H., and Mitchell, P., 1964, J. Scient. Instrum., 41, 555.

Carver, J.H., Mitchell, P., Murray, E.L., and Rofe, B., 1965, Space Research VI, Ed. R.L. Smith-Rose (Spartan Books, Washington, D.C.) pp 373 - 377.

Carver, J.H., and Mitchell, P., 1967, J. Opt. Soc. Amer., 57, 738.

Carver, J.H., Edwards, P.J., Gough, P.L., Gregory, A.G., Rofe, B., and Johnson, S.G., 1969, J. Atmos. Terr. Phys., 31, 563.

Chubb, T.A., and Friedman, H., 1955, Rev. Scient. Instrum., 26, 493.

Chubb, T.A., Friedman, H., Kreplin, R.W., and Kupperian, J.E., 1957, J. Geophys. Res., 62, 389.

Colegrove, F.D., Johnson, F.S. and Hanson, W.B.,1966, J. Geophys. Res., 71, 2227.

Cook, G.R., and Ching, B.K., 1965, Rep. No. TDR-469 (9260-01)-4 (Aerospace Corp.)

Cospar International Reference Atmosphere 1965, 1965, (North-Holland Publ. Co., Amsterdam).

de Jager, C., 1964, Research in Geophysics, Ed. H. Odislow (Massachusetts; MIT Press), vol. 1, p.1.

Detwiler, C.R., Purcell, J.D., and Tousey, R., 1961a, Mem. Soc. R. Sci. Liege, Ser. 5, 4, 253.

Detwiler, C.R., Garrett, D.L., Purcell, J.D., and Tousey, R., 1961b, Annls., Geophys., 17, 9.

Ditchburn, R.W., 1962, J. Quant. Spectrosc. Radiat. Transfer, 2, 361.

Ditchburn, R.W. Bradley, J.E.S., Cannon, C.G., and Munday, G., 1954, Rocket Exploration of the Upper Atmosphere, Ed. R.L.E. Boyd and M.J. Seaten (London: Pergamon Press) p.327.

Friedman, H., 1960, Physics of the Upper Atmosphere, Ed. J.A. Ratcliffe (New York: Academic Press), p.133.

Friedman, H., Lichtman, S.W., and Byram, E.T., 1951, Phys. Rev., 83, 1025.

Friedman, H., Chubb, T.A., Kupperian, J.E., and Lindsay, J.C., 1958, Annals of the I.G.Y., vol. 6, p.316.

Friedman, H., Chubb, T.A., and Siomkajlo, J.M., 1964, Sounding Rocket Research Techniques, Instruction Manual No. 9, (IQSY, Secretariat, London) pp.89-104.

Friedman, H., 1967, Proc. Nat. Ac. Sci., 58, 6, 2162.

Gadsden, M. and Marovich, E., 1969, J. Atmos. Terr. Phys., 31, 817.

Gingerich, O., and de Jager, C., 1968, Solar Phys., 3, 5.

Gingerich, O., and Rich, J.C., 1968, Solar Phys., 3, 82.

Goldberg, L., Parkinson, W.H., and Reeves, E.M., 1965, Astrophys. J., 141, 1293.

Goldberg, L., 1963, J. Quant. Spectrosc. Radiat. Tranfer., 3, 519.

Golomb, D., Rosenberg, N.W., Aharonian, C., Hill, J.A.F., and Alden, H.L. 1965, J. Geophys. Res., 70, 1155.

Hall, L.A., Damon, K.A., and Hinteregger, H.E., 1963a, Space Research 3, 745.

Hall, L.A., Schweizer, W., and Hinteregger, H.E., 1963b, J. Geophys. Res., 68, 6413.

Hall, L.A., Schweizer, W., and Hinteregger, H.E., 1965, J. Geophys. Res., 70, 105.

Hall, L.A., Schweizer, W., and Hinteregger, H.E., 1965, J. Geophys. Res., 70, 2241.

Hall, L.A., Chagnon, C.W., and Hinteregger, H.E., 1967, J. Geophys. Res., 72, 3425.

Hall, L.A., Higgins, J.E., Chagnon, C.W., and Hinteregger, H.E., 1969, J. Geophys. Res., 74, 4181.

Hedin, A.E., Avery, C.P., Tschetter, C.D., 1964, J. Geophys. Res., 69, 4637.

Hedin, A.E., and Nier, A.O., 1965, J. Geophy. Res., 70, 1273.

Hedin, A.E., and Nier, A.O., 1966, J. Geophy. Res., 71, 4121.

Heroux, L., Newburgh, R.G., McMahon, W.J., and Hinteregger, H.E., 1968, App. Opt. 7, 37.

Hinteregger, H.E., 1961a, Space Astrophysics, Ed. W. Liller (New York: McGraw-Hill) p.34.

Hinteregger, H.E., 1961b, Mem.Soc. R. Sci. Liege., ser. 5, 4, 111.

Hinteregger, H.E., 1961c, J. Geophys. Res., 66, 2367.

Hinteregger, H.E., 1962, J. Atmos. Sci., 19, 351.

Hinteregger, H.E., and Watanabe, K., 1953, J. Opt. Soc. Am., 43, 604.

Hinteregger, H.E., and Watanabe, K., 1962, J. Geophys. Res., 67, 3373.

Hinteregger, H.E., Hall, L.A., and Schmidtke, G., 1965, Space Research 5, 1175.

Hinteregger, H.E., 1965, Space Sci. Rev., 4, 461.

Hinteregger, H.E., Solar Spectrum (Dordrecht: D. Reidel 1965), pp. 179-205.

Inn, E.C.Y., Watanabe, K., and Zelikoff, M., 1953, J. Chem. Phys., 21, 1648.

Johnson, F.S., Purcell, J.D., Watanabe, K., and Tousey, R., 1952, J. Geophys. Res., 57, 157.

Johnson, F.S., Purcell, J.D., and Tousey, R., 1954, Phys. Rev., 95, 621.

Johnson, F.S., 1956, J. Opt. Soc. Am., 46, 101.

Johnson, F.S., Malitson, H.H., Purcell, J.D., and Tousey, R., 1958, Astrophys. J., 127, 80.

Jursa, A.S., Tanaka, Y., and LeBlanc, F., 1959, Planet Space Sci., 1, 161.

Jursa, A.S., Nakamura, M., and Tanaka, Y., 1963, J. Geophys. Res., 68, 6145.

Jursa, A.S., Nakamura, M., and Tanaka, Y., 1965, J. Geophys. Res., 70, 2699

Kallmann-Bijl., H.K., and Sibley, W.L., 1963, Planet Space Sci., 11, 1379.

Kasprzak, W.T., Krankowsky, D., and Nier, A.O., 1968, J. Geophys. Res., 73, 6765.

Knapp, R.A., and Smith, A.M., 1964, App. Opt., 3, 637.

Knudson, A.R., and Kupperian, J.E., 1957, J. Opt. Soc. Am., 47, 440.

Krankowsky, D., Kasprzak, W.T., and Nier, A.O., 1968, J. Geophys. Res., 73, 7291.

Kreplin, R.W., Chubb, T.A., and Friedman, H., 1962, J. Geophys. Res., 67, 2231.

Kupperian, J.E., and Kreplin, R.W., 1957, Rev. Scient. Instrum., 28, 14.

Kupperian, J.E., Byram, E.T., and Friedman, H., 1959, J. Atmos. Terr. Phys., 16, 174.

Laufer, A.H., Pirog, J.A., and McNesby, J.R., 1965, J. Opt. Soc. Am., 55, 64.

Lee, P., 1955, J. Opt. Soc. Am., 45, 703.

Marmo, F.F., 1953, J. Opt. Soc. Am., 43, 1186.

Mauersberger, K., Muller, D., Offerman, D., and von Zahn, U., 1968, J. Geophys. Res., 73, 1071.

Metzger, P.H., and Cook, G.R., 1964, J. Quant. Spectrosc. Radiat. Tranfer, 4, 107.

Metzger, P.H., and Cook, G.R., 1965, J. Opt. Soc. Am., 55, 516.

Mitchell, P., Ph.D. Thesis, University of Adelaide, 1966.

Muller, D., and Hartmann, G., 1969, J. Geophy. Res., 74, 1287.

Nicolet, M., 1960, Physics of the Upper Atmosphere, Ed., J.A. Ratcliffe (New York : Academic Press) p.17.

Nier, A.O., Hoffman, J.H., Johnson, C.Y., and Holmes, J.C., 1964, J. Geophys. Res., 69, 979.

Norton, R.B., and Warnock, J.M., 1968, J. Geophys. Res., 73, 5798.

Ogawa, M., 1968, J. Geophys. Res., 73, 6759

Parkinson, W.H., and Reeves, E.M., 1969, Solar Physics, 10, 342.

Preston, W.M., 1940, Phys. Rev., 57, 887.

Purcell, J.D., Packer, D.M., and Tousey, R., 1960, Space Research 1, 581.

Purcell, J.D., and Tousey, R., 1960, J. Geophys. Res., 65, 370.

Rense, W.A., 1953, Phys. Rev., 91, 299.

Rense, W.A., 1961, Space Astrophysics, Ed. W. Liller (New York : McGraw Hill) p.17.

Sampson, J.A.R., 1964, J. Opt. Soc. Am., 54, 6.

Schaefer, E.J., 1969, J. Geophys. Res., 74, 3488.

Smith, L.G., and Weeks, L.H., 1965, Geophysics Corporation of America, Tech. Rep. 65-10-N.

Smith, L.G., Accardo, C.A., Weeks, L.H. and McKinnon, P.J., 1965, J. Atmos., Terr. Phys., 27, 803.

Stewart, K.H. and Wildman, P.J.L., 1968, Nature 219, 5155, 714.

Stewart, K.H., and Wildman, P.J.L., 1969, Proc. Roy. Soc. A. 311, 391.

Stober, A.K., Scolnik, R., and Hennes, J.P., 1963, Appl. Opt., 2, 735.

Tanaka, Y., 1955, J. Opt. Soc. Am., 45, 663.

Tanaka, Y., Inn, E.C.Y., and Watanabe, K., 1953, J. Chem. Phys., 21, 1651.

Tanaka, Y., Jursa, A.S., and LeBlanc, F., 1960, J. Chem. Phys., 32, 1205.

Taylor, R.G., Chubb, T.A., and Kreplin, R.W., 1965, J. Opt. Soc. Am., 55, 1078.

Tousey, R., 1963, Space Sci. Rev., 2, 3.

Tousey, R., Watanabe, K., and Purcell, J.D., 1951, Phys. Rev., 83, 792.

Tousey, R., Purcell, J.D., Austin, W.E., Garrett, D.L., and Widing, K.G., 1964, Space Research 4, 703.

Tousey, R., 1964, Quart. J. Roy. Astrom. Soc., 5, 123.

Tousey, R., 1967, Astro. Phys. J., 149, 2, Pt. 1, 239.

Tousey, R., 1967, App. Opt., 6, 12, 2044.

U.S. Standard Atmosphere, 1962 (Washington, D.C. : U.S. Govt. Printing Office).

Violett, T., and Resne, W.A., 1959, Astrophys. J., 130, 954.

Watanabe, K., 1954, J. Chem. Phys., 22, 1564.

Watanabe, K., and Inn, E.C.Y., 1953, J. Opt. Soc. Am., 43, 32.

Watanabe, K., and Zelikoff, M., 1953, J. Opt. Soc. Am., 43, 753.

Watanabe, K., Inn, E.C.Y., and Zelikoff, M., 1953a, J. Chem. Phys., 21, 1026.

Watanabe, K., Marmo, F.F., and Inn, E.C.Y., 1953b, Phys. Rev., 90, 155.

Watanabe, K., and Matsunaga, F.M., 1961, Hawaii Inst. Geophys. Contril, 27, Honolulu.

Watanabe, K., Nakayama, T., and Mottl, J., 1962, J. Quant. Spectrosc. Radiat. Tranfer, 2, 369.

Weeks, L.H., 1967, Astrophys. J., 147, 1203.

Weeks, L.H., and Smith, L.G., 1968, J. Geophys. Res. 73, 4835.

Widing, K.G., Purcell, J.D., and Sandlin, G.D., 1970, Solar Physics, 12, 52.

Wildman, P.J.L., Kerley, M.J., and Shaw, M.S., 1969, J. Atmos. Terr. Phys., 31, 951.

von Zahn, U., 1967, J. Geophys. Res., 72, 5933.

von Zahn, U.,1969, J. Geophys. Res., 74, 4055.

von Zahn, U., 1970, J. Geophys. Res., 75, 5517.